UNIVERSITÀ DEGLI STUDI DI PAVIA
DOTTORATO DI RICERCA IN FISICA – XXXIV CICLO

Nuclear Magnetic Resonance Relaxation

Clinical MRI Mapping Harmonization and Novel Aspects in Ln-based Contrast Agents

Davide Cicolari

Tesi per il conseguimento del titolo

Università degli Studi di Pavia

Dottorato di Ricerca in Fisica – XXXIV Ciclo

NUCLEAR MAGNETIC RESONANCE RELAXATION

CLINICAL MRI MAPPING HARMONIZATION AND NOVEL ASPECTS IN LN-BASED CONTRAST AGENTS

DAVIDE CICOLARI

ADVISORS:	REFEREES:
Dr. Manuel Mariani	Prof. Mauro Botta
Prof. Alessandro Lascialfari	Prof. Sophie Laurent

Submitted to the Graduate School of Physics
in partial fulfillment of the requirements for the degree of

DOTTORE DI RICERCA IN FISICA
DOCTOR OF PHILOSOPHY IN PHYSICS

at the
University of Pavia

COVER:
Tri-morphic Resonance Painting
Lewis Pathack
United Kingdom
2015

TITLE:
Nuclear Magnetic Resonance Relaxation :
Clinical MRI Mapping Harmonization and Novel Aspects in Ln-based Contrast Agents

AUTHOR:
Davide Cicolari

PhD Thesis – Università degli Studi di Pavia
Pavia, Italy, June 2021

’I will take the Ring,’ he said, ’though I do not know the way.’

— J.R.R. Tolkien, *The Lord of the Rings*

It is our choices, Harry, that show what we truly are, far more than our abilities.

— J.K. Rowling, *Harry Potter and the Chamber of Secrets*

ABSTRACT

This PhD thesis has two major purposes. The first goal is to propose a robust method based on a well-characterized in-scan reference phantom for the validation and harmonization of relaxation time maps acquired through Magnetic Resonance Imaging (MRI) techniques. The second goal is to investigate novel aspects of the relaxation enhancement mechanisms of some lanthanide complexes, used as MRI contrast agents for high-field applications by analyzing their Nuclear Magnetic Relaxation Dispersion (NMRD) profiles. These goals are accomplished by means of ^{1}H Nuclear Magnetic Resonance (NMR) relaxometry and MRI techniques employing different scanners and spectrometers at several magnetic field strengths. These research projects were conducted thanks to cross-collaborations between national and international research groups and hospital structures.

As to the first goal, we present a proof-of-concept study focusing on a method for the intra- and inter-center validation and harmonization of data obtained from MRI T_1 and T_2 maps. The method is suggested for the simultaneous scan of the patient and a set of $MnCl_2$ samples, arranged in a cartridge-like belt configuration, that provide in-scan ground-truth reference values for the recalibration of the maps, regardless of the details of the MRI protocol. The relaxation times of $MnCl_2$ aqueous solutions were first measured by means of an NMR laboratory relaxometer, as a function of concentration and temperature. The obtained T_1 and T_2 values, once renormalized at the scanner temperature, were used as reference values for the MRI mapping measurements of the $MnCl_2$ relaxation times. By using different clinical MRI scanners and sequences, we found a good agreement for standard and turbo sequences (limits of agreement: 5% for IR, SE, IR-TSE; 10% for TSE), while an under-estimation and an over-estimation were found respectively for MOLLI and T_2-prep TrueFISP, as already reported in the literature. The linearity of the relaxation rates with the concentration predicted by the Solomon-Bloembergen-Morgan theory was observed for every dataset at all temperatures, except for T_2-prep TrueFISP maps results. A phantom study and a preliminary *in vivo* experiment on an untrained volunteer confirmed the feasibility of map recalibration for MOLLI sequence while questioning the reliability of T_2-prep TrueFISP maps, for which further investigations are needed.

In the second research project, longitudinal and transverse ^{1}H NMR nuclear relaxivities of Ln(III)-DOTA complexes (with Ln = Gd, Dy, Tb, Er; DOTA = 1,4,7,10 - tetraazacyclododecane - N,N′,N″,N‴ - tetraacetic acid) and Mn(II) aqueous solutions were measured in a wide range of frequencies, 10 kHz - 700 MHz. The experimental data were interpreted by means of models derived from the Solomon-Bloembergen-Morgan theory. The data analysis was performed assuming the orbital angular momentum $L = 0$ for Gd-DOTA and the aqua ion $[\mathrm{Mn(H_2O)_6}]^{2+}$ and $L \neq 0$ for Dy-DOTA, Tb-DOTA, and Er-DOTA. A refined estimation of the Zero-Field-Splitting barrier Δ and of the modulation correlation time τ_v was obtained for $[\mathrm{Mn(H_2O)_6}]^{2+}$ by extending the fitting of NMRD profiles to the low-field regime. The Gd-DOTA fitting parameters resulted in good agreement with the literature, and the fit of transverse relaxivity data confirmed the negligibility of the scalar interaction in the nuclear relaxation mechanism. Larger transverse relaxivities of Dy-DOTA and Tb-DOTA ($\sim$ 10 mM^{-1}s^{-1}) with respect to Er-DOTA ($\sim$ 1 mM^{-1}s^{-1}) were observed at 16 T, compatibly with a shorter residence time of the coordinated water molecule τ_m, which heavily influences the fluctuation rate of the dipolar electron-nuclear interaction that, in turn, depends on the electronic spin correlation rate and the magnetic anisotropy. The possible employment of Dy-DOTA, Tb-DOTA, and Er-DOTA as negative MRI contrast agents for high-field applications was envisaged by collecting spin-echo images at 7 T. Particularly in Dy- and Tb- derivatives the transverse relaxivity at 16 T is of the order of the Gd- one at 1.5 T.

CONTENTS

LIST OF FIGURES

ACRONYMS

AMT	(Center for) Adaptable MRI Technology
bSSFP	balanced - Steady State Free Precession
CA	Contrast Agent
CPMG	Carr-Purcell-Meiboom-Gill
CSF	Cerebro-Spinal Fluid
CT	Computed Tomography
EPI	Echo Planar Imaging
FA	Flip Angle
FFC	Fast Field-Cycling
FID	Free Induction Decay
FISP	Fast Imaging with Steady Precession
FT	Fourier Transform
HRV	Heart-Rate Variability
HU	Hounsfield Unit
INFN	Italian National Institute for Nuclear Physics
IR	Inversion Recovery
LV	Left Ventricle
MOLLI	Modified Look-Locker Inversion Recovery
MRF	Magnetic Resonance Fingerprinting
MRI	Magnetic Resonance Imaging
NMR	Nuclear Magnetic Resonance

NMRD	Nuclear Magnetic Relaxation Dispersion
NP	Non-Polarized
PP	Pre-Polarized
PTFE	Polytetrafluoroethylene
QA	Quality Assurance
RARE	Rapid Acquisition with Relaxation Enhancement
RV	Right Ventricle
SE	Spin-Echo
SR	Saturation Recovery
SSFP	Steady State Free Precession
TSE	Turbo Spin-Echo
ZFS	Zero Field Splitting

1

INTRODUCTION

The phenomenological Bloch equations [1] describe the temporal evolution of a spin system, drawn in a static and homogeneous magnetic field when perturbed by radiofrequency pulses. Such temporal evolution is governed by the so-called *relaxation times* T_1, or *spin-lattice r.t.*, and T_2, or *spin-spin r.t.*, which characterize, respectively, the return to equilibrium of the spin-system due to the interactions with the surrounding environment and the whole ensemble of non-equilibrium processes due to the spins interacting with each other.

This spin dynamics is at the heart of the Nuclear Magnetic Resonance (NMR) techniques [2], in which a nucleus with non-null magnetic moment is exploited as a local probe for the characterization of materials and biological tissues. Magnetic Resonance Imaging (MRI) [3] represents the spatially-resolved evolution of NMR that allows the generation of images, hence finding a useful practical application in clinics, since it permits avoiding the use of ionizing radiations and their potentially harmful side-effects. The strict relation between the MRI signal and the relaxation times is commonly used for the different weighting of the images, increasing or lowering the signal of anatomical features by properly adjusting the acquisition parameters [4]. Two other techniques have been developed to further exploit the MRI signal dependence from relaxation times: the relaxation time mapping and the use of contrast agents.

As concerns the relaxation time mapping, which is a recent achievement due to the modern advancement of MRI technology, it consists in acquiring a series of images of the same body slice by setting the acquisition parameters in order to reconstruct the relaxation curves of each represented tissue: the relaxation time maps can be obtained through a pixel-wise fit of the series of images. The greatest advantage of the mapping techniques is that it provides images with both qualitative and quantitative information. These maps can be used for the diagnosis and monitoring of several pathologies as reported by Cheng *et al.* [5]. The problem of long acquisition times of standard sequences (such as Spin-Echo and Inversion Recovery) has been overcome in recent years with the development of faster sequences suitable

for clinical practice (*i.e.* the acquisitions are usually performed during a single breath-hold) even for the challenging field of cardiac MRI [6, 7].
Since their introduction, it has become clear that such sequences are affected by a severe variability (at the equal static external magnetic field, usually 1.5 or 3 T): relaxation time values can change in a non-negligible manner when comparing results from acquisitions performed with different mapping sequences, MRI scanners and software [8–12]. Inter-platform and inter-center variabilities oblige the collection of reference 'normal' data, *i.e.* the reference values of a cohort of healthy volunteers, for each sequence and scanner used in clinical protocols (it is noted that also upgrades of the scanner's software could require a recollection of normal data). Several international projects in current years have investigated this harmonization issue for relaxation time mapping data: they usually rely on tissue-mimicking calibration phantoms, although without taking into consideration the possibility of using them as an in-scan reference [13, 14].

More basic and qualitative use of the relation between the MRI signal and the relaxation times can be found in the clinical application of contrast agents (CAs) [15]. Contrast agents design allows them to accumulate in pathological anatomical tissues and structures (*e.g.* cancer): their scope is to enhance the gray-level contrast of the MRI image, facilitating the disease detection by clinicians, hence leading to improvements in medical diagnosis. The contrast enhancement is obtained by reducing locally mainly the T_1 (*positive CAs*, since they produce brighter regions in T_1-weighted images) or T_2 (*negative CAs*, producing darker regions in T_2-weighted images). This aim can be achieved by using paramagnetic substances: the theory of solvent nuclear relaxation enhancement due to the presence of paramagnetic substances was developed starting from the pioneering work of Bloembergen *et al.* [16] with the contributions of Solomon [17, 18] and Morgan [19]. The SBM theory allows characterizing the microscopical dynamic properties of a paramagnetic complex in solution through the analysis of its Nuclear Magnetic Relaxation Dispersion (NMRD) profile in which the *relaxivity*, *i.e.* the relaxation enhancement efficiency, is plotted as a function of the Larmor resonance frequency of the solvent nuclei (usually ^{1}H).
Extensive studies of these materials have been conducted in the past 40 years finding widespread use in clinics [20]: nowadays, complexes based on Gd(III) are the most widely used, thanks to the seven unpaired electrons and the long electronic relaxation times (due to the symmetric S-state) of Gd(III). However, driven by the technological developments of MRI scanner targeted to the employment of increasingly higher magnetic fields ($>$ 7 T), other Ln(III) ions have been suggested for the design of CAs by taking advantage of the chemical shift that these compounds induce on the NMR spectra (in fact, non-Gd Ln-based compounds are used as shift agents for NMR spectroscopic applications) [21, 22]. It is worth

mentioning that the interest in Ln(III) complexes lies in their applicability as multi-functional Single-Molecule Magnets (SMMs) for the development of quantum information processing and spintronics devices combined to their photo-luminescence properties [23–25].

This thesis aims to study the application of the relaxation times measurement for the investigation of the two main topics introduced above: (i) the development of an NMR characterized phantom-based method for MRI relaxation times mapping data validation and harmonization; (ii) novel aspects in NMR relaxation of Ln(III)-based complexes as high-field contrast agents through the analysis of their NMRD profiles.

An overview of the thesis content and structure is given in the next paragraph.

THESIS OVERVIEW

In **Chapter 2**, the first Section presents the physical principles at the basis of NMR techniques, introducing both the quantum and semi-classical approaches, and recalling the phenomenological Bloch equations that govern the temporal evolution of the magnetization vector. The concepts of longitudinal spin-lattice T_1 and transverse spin-spin T_2 relaxation times are given. A dedicated part is reserved for the principal spectroscopic pulse sequences used for the measurement of relaxation times. In the second Section, the principles of image generation through MRI techniques are illustrated flanked by an excursus of the employed mapping sequences. The third Section describes the mechanisms at the basis of MRI contrast agents, presenting the Solomon-Bloembergen-Morgan theory for paramagnetic dilute solutions and introducing also the concepts of relaxivity (*i.e.* the relaxation enhancement efficiency), correlation times (which characterize the statistical correlation between random variables over time) and NMRD profiles (*i.e.* the plot of relaxivity *vs* Larmor frequency); a short presentation of the Fast-Field-Cycling (FFC) techniques is also provided.

Chapter 3 focuses on the project carried out in collaboration with the Niguarda Hospital in Milan (Italy) aiming to develop a phantom-based method for MRI mapping data validation and harmonization. In the first part of the Chapter the phantom preparation and characterization through NMR techniques are described: the relaxation times of the vials composing the phantom, each filled with aqueous solutions of $MnCl_2$, were measured as a function of both temperature (in a small range around the room temperature) and $MnCl_2$ concentration. The second part concerns the results obtained from the three main experiments performed on clinical mapping sequences. In Exp. 1, the phantom alone was used for testing the performances of different mapping sequences (standard, turbo, and fast-cardiac) employing two different 1.5 T MRI scanners; in Exp. 2 the ′belt phantom′ (since it can be wrapped around anatomical regions in a cartridge-like belt configuration) was used as an in-scan reference for a phantom study in order to evaluate the influence of the heart-rate and the applicability of map recalibration; Exp. 3 consisted in a preliminary *in vivo* application of the method on an untrained volunteer.

Chapter 4 deals with the study performed in collaboration with the Department of Chemistry of the University of Florence and the Department of Physics of the University of Milan regarding the characterization of Ln-based high-field MRI contrast agents through the analysis of both longitudinal and transverse NMRD profiles. The investigated lanthanide complexes are presented: Ln(III)-DOTA, with Ln = Gd, Dy, Tb, and Er and DOTA = 1,4,7,10 - tetraazacyclododecane - N,N′,N″,N‴ - tetraacetic acid. Mn(II) aqua ions were considered as well for comparison. A detailed description of the models derived from the SBM theory for the analysis of the NMRD profiles is provided. The experimental details of the samples preparation, NMRD profiles measurement, and MRI images acquisitions are also given: the profiles were collected by means of both standard NMR and FFC relaxometry techniques spanning a wide range of frequencies (from 10 kHz to 700 MHz); two MRI scanners with different magnetic fields were used for the images acquisitions (0.18 T and 7 T). The higher transverse relaxivities at high-fields of Dy-DOTA and Tb-DOTA with respect to Er-DOTA ones are put in relation with the different magnetic anisotropies of the complexes (easy-axis for Dy-DOTA and Tb-DOTA, easy-plane for Er-DOTA).

In **Appendix A**, a summary of the researches conducted by the candidate during a 4 months mobility project at the AMT (Center for Adaptable MRI Technology) in Basel (Switzerland) concerning the development of low-field mapping sequences can be found. Two different topics are presented: (i) the development of T_1 and T_2 magnetization prepared Steady-State Free Precession (SSFP) sequences for the fast relaxation times mapping and (ii) the schedule optimization strategy for Magnetic Resonance Fingerprinting (MRF) acquisitions.

2

NMR, MRI AND CONTRAST AGENTS

The theoretical bases of Nuclear Magnetic Resonance (NMR), of Magnetic Resonance Imaging (MRI), and of Contrast Agents (CAs) will be presented. The principal techniques for signal/image acquisition and measurement will be also introduced. The main literature references for this Chapter are: [4] (Section 1: NMR; Section 2: MRI); [26] and [15] (Section 3: CAs).

2.1 NUCLEAR MAGNETIC RESONANCE

Discovered by Rabi in 1937 in an experiment published in 1938 [2] (Nobel Prize in Physics in 1944), and successively developed by Purcell and Bloch in the late ′40$_s$ - early ′50$_s$ [1, 27] (shared Nobel Prize in Physics in 1952), the Nuclear Magnetic Resonance (NMR) is a technique that exploits the nucleus as a local probe in order to study and characterize all the interactions and energy-exchange mechanisms between the nucleus itself and its surrounding environment, which can be of different nature, *e.g.* magnetic fields, electrons, other nuclei, molecules, etc.

2.1.1 Principles

An NMR experiment consists in placing a sample in a static and homogeneous magnetic induction $\boldsymbol{B_0} = \mu_0 \boldsymbol{H_0}$ (measured in Tesla, [T]), where μ_0 represents the vacuum permeability and $\boldsymbol{H_0}$ the magnetic field (measured in Ampere/meter, [A/m]), causing the Zeeman energy levels splitting in nuclear species, typically ^{1}H for its natural abundance (99.98%).

The angular momentum of a charged particle is related to its magnetic moment with a empiric law as follows

$$\boldsymbol{\mu} = \gamma \boldsymbol{J} \tag{1}$$

where $\boldsymbol{J}$ is the total angular momentum ($\boldsymbol{J} = \boldsymbol{L} + \boldsymbol{S}$, being $\boldsymbol{L}$ and $\boldsymbol{S}$ the orbital and the spin angular momentum respectively) and the proportionality constant γ is called gyromagnetic ratio and depends on the nuclear species ($\gamma = 2.675 \times 10^8$ rad s^{-1} T^{-1} for ^{1}H nuclei).

The Zeeman hamiltonian of particles with non-null angular momentum interacting with an external static magnetic induction $\boldsymbol{B_0} = B_0\hat{z}$ is given by

$$\boldsymbol{\mathcal{H}} = -\boldsymbol{\mu} \cdot \boldsymbol{B_0} = -\gamma J_z B_0 = -\gamma \hbar m_J B_0 \tag{2}$$

where the relation $J_z = m_J\hbar$ has been used (m_J are the $2J + 1$ quantum number; $m_J = -J, -J+1, ...J-1, J$).

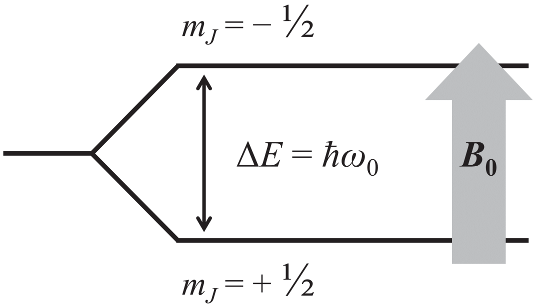

Figure 1: The splitting of the energy levels due to the Zeeman effect for a system of protons, which have positive gyromagnetic ratio, interacting with an external static magnetic induction $\boldsymbol{B_0}$.

Considering protons (^{1}H nuclei), *i.e.* particles with $\boldsymbol{L} = 0$ and $\boldsymbol{S} = 1/2$ (hence $\boldsymbol{J} = \boldsymbol{S}$; noticed that the nuclear spin is usually indicated with $\boldsymbol{I}$), the degeneration of the energy levels is resolved with two possible energy states ($m_S = \pm 1/2$) as illustrated in Fig. 1, the lower one populated by protons with spin parallel to the field ($m_S = +1/2$), while the higher one by anti-parallel spin protons ($m_S = -1/2$). The energy gap between the two states, associated to the absorption or emission of quanta (*photons*) by the proton spin system, is found to be $\Delta E = \hbar\omega_0$, with ω_0 defined as the *Larmor angular frequency*

$$\omega_0 = \gamma B_0 \tag{3}$$

The Boltzmann statistics determines the difference of the occupational number of the levels, $N \propto \exp(\Delta E / k_B T)$, with k_B being the Boltzmann constant: the small occupation discrepancy (~ 7 ppm at 1 T and room temperature) results in a net macroscopic magnetization vector $\boldsymbol{M}$, with thermal equilibrium value $M_0 \propto \gamma^2 \rho B_0 / T$, where ρ is the proton density and T is the temperature.

From a classical point of view, the magnetization vector is defined as a volumetric average of the magnetic moments $\boldsymbol{\mu}$ of the nuclei, drawn in the magnetic induction $\boldsymbol{B_0}$, that precess clockwise at the Larmor angular frequency ω_0 around the direction of $\boldsymbol{B_0}$ itself:

$$\boldsymbol{M} = \sum_i \frac{\boldsymbol{\mu}_i}{V} \tag{4}$$

The precession motion of $\boldsymbol{M}$, see Fig. 2, is then described by the following equation

$$\frac{d\boldsymbol{M}}{dt} = \gamma \boldsymbol{M} \wedge \boldsymbol{B_0} \tag{5}$$

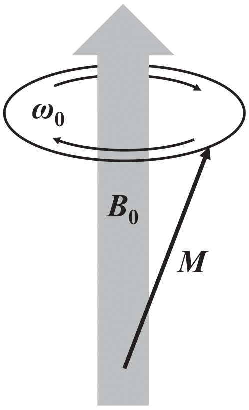

Figure 2: The precession motion of the magnetization vector $\boldsymbol{M}$ around the static magnetic induction $\boldsymbol{B_0}$ with Larmor angular frequency $\boldsymbol{\omega_0}$ described by Eq. 5.

2.1.2 Rotating Frame and RF Pulses

Considering a rotating reference frame, denoted with primed quantities, about an arbitrary axis with angular velocity vector $\boldsymbol{\omega}$, the left term in Eq. 5 can be expressed in the convective form

$$\frac{d\boldsymbol{M}}{dt} = \left(\frac{d\boldsymbol{M}}{dt}\right)' + \boldsymbol{\omega} \wedge \boldsymbol{M} \tag{6}$$

leading to the motion equation of $\boldsymbol{M}$ in the rotating frame

$$\left(\frac{d\boldsymbol{M}}{dt}\right)' = \gamma \boldsymbol{M} \wedge \boldsymbol{B_{eff}} \tag{7}$$

that has the same structure as Eq. 5, where the *effective magnetic induction* in the rotating frame is given by

$$\boldsymbol{B}_{eff} = \boldsymbol{B}_0 + \frac{\boldsymbol{\omega}}{\gamma} \tag{8}$$

As a consequence, a rotating reference frame with an angular velocity vector $\boldsymbol{\omega}$ can be always chosen in order to null the temporal variation of the magnetization vector (*i.e.* $\boldsymbol{M}$ constant in the rotating frame).

The interaction with the spin system is performed by means of a magnetic induction $\boldsymbol{B}_1$ applied on resonance and for a short time, hence called *radiofrequency pulse* (or *rf pulse*). The purpose of this excitation is to change the magnetization vector precession angle, so $\boldsymbol{B}_1$ must be orthogonal to $\boldsymbol{B}_0$, thus resulting in an effective magnetic induction $\boldsymbol{B}_{eff} = \boldsymbol{B}_1$ in the co-rotating reference frame ($\boldsymbol{\omega} = \boldsymbol{\omega}_0$). The effect of $\boldsymbol{B}_1$ is depicted in Fig. 3: it causes the magnetization vector to precess around it, following Eq. 7.
The angle variation $\Delta\vartheta$ induced by a constant $\boldsymbol{B}_1$ with a total duration τ is then given by

$$\Delta\vartheta = \gamma \left|\boldsymbol{B}_1\right| \tau \tag{9}$$

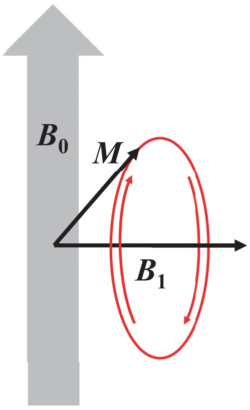

Figure 3: Precession of the magnetization vector $\boldsymbol{M}$ around the rf pulse $\boldsymbol{B}_1$ in the co-rotating reference frame ($\boldsymbol{\omega} = \boldsymbol{\omega}_0$).

2.1.3 Bloch Equations and Relaxation Times

After the application of an adiabatic rf pulse that tips the magnetization vector, the system returns to the thermal equilibrium condition with a temporal dependence described by the empirical (or phenomenological) vector equation called *Bloch equation*

$$\frac{d\boldsymbol{M}}{dt} = \gamma \boldsymbol{M} \wedge \boldsymbol{B_0} + \frac{1}{T_1}(M_0 - M_z)\hat{z} - \frac{1}{T_2}\boldsymbol{M}_\perp \tag{10}$$

that is composed by the precession term, as in Eq. 5, and two relaxation terms: assuming $\boldsymbol{B_0}$ directed along the $\hat{z}$-axis, the second term on the right part of the equation regards the parallel, or 'longitudinal', component of the magnetization vector $\boldsymbol{M}_{||} = M_z\hat{z}$ while the third term concerns the transverse components $\boldsymbol{M}_\perp = M_x\hat{x} + M_y\hat{y}$.

The temporal dependence of the evolutions of the longitudinal and transverse components of the magnetization vector is governed by two different characteristic time constants, whose values depends on the interactions of the nucleus with its surrounding environment:

- ***T*₁, spin-lattice relaxation time**: also known as *longitudinal relaxation time*, it characterizes the regrowth of the longitudinal component of the magnetization vector towards the thermal equilibrium value M_0, and it depends on the transition probability between the energy states splitted by the Zeeman effect;

- ***T*₂, spin-spin relaxation time**: also known as *transverse relaxation time*, it characterizes all the non-equilibrium processes due to the local randomly fluctuating field variations generated by neighboring nuclei, which cause the magnetic moments to resonate in a distribution of frequencies centered in ω_0 (collective dephasing effect).

It is also useful to introduce the longitudinal and transverse *relaxation rates*, defined by:

$$R_1 \equiv 1/T_1 \text{ and } R_2 \equiv 1/T_2 \tag{11}$$

The inhomogeneities of the static magnetic induction $\boldsymbol{B_0}$ contribute to an additional dephasing of the magnetization characterized by another decay time T_2' (or rate $R_2' = 1/T_2'$), resulting in a overall transverse relaxation time T_2^* (or rate $R_2^* = 1/T_2^*$), related to the others by

$$\frac{1}{T_2^*} = \frac{1}{T_2} + \frac{1}{T_2'} \quad (\text{or } R_2^* = R_2 + R_2') \tag{12}$$

and that should be used in Eq. 10 instead of T_2.

A SIMPLE CASE

Let us now consider the simple case of an NMR experiment in which the system is drawn in a static and homogeneous magnetic induction $\boldsymbol{B_0} = B_0\hat{z}$

and an on-resonance rf pulse rotates adiabatically the magnetization vector of 90° from the initial equilibrium position $\boldsymbol{M} = M_0\hat{z}$. The solutions of the Bloch equation in the laboratory and co-rotating frame can be calculated analytically:

- LABORATORY FRAME

$$\begin{aligned} M_\perp(t) &= M_0\, e^{-t/T_2}\, e^{-i\omega_0 t} \\ M_z(t) &= M_0 \left(1 - e^{-t/T_1}\right) \end{aligned} \tag{13}$$

- CO-ROTATING FRAME

$$\begin{aligned} M_\perp(t) &= M_0\, e^{-t/T_2} \\ M_z(t) &= M_0 \left(1 - e^{-t/T_1}\right) \end{aligned} \tag{14}$$

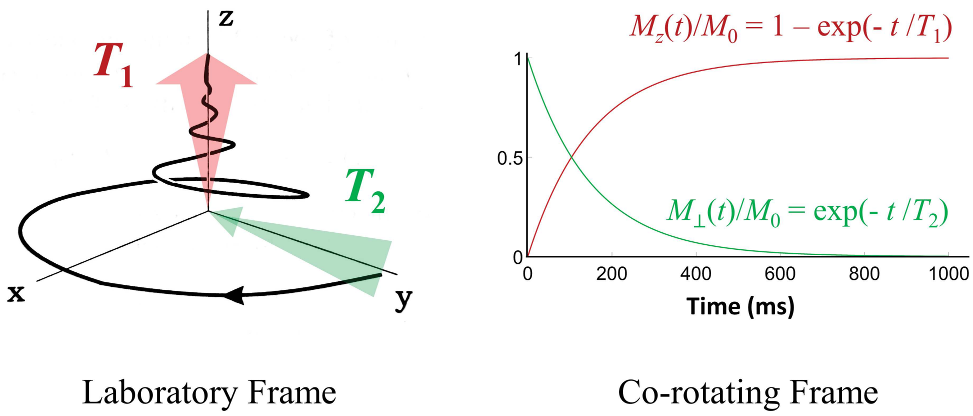

Figure 4: Trajectory of the magnetization vector towards the equilibrium as described by Eq. 10 in the laboratory frame (left, Eq. 13) and the temporal evolution of its components in the co-rotating frame (right, Eq. 14) after the application of an on-resonance 90° rf pulse.

2.1.4 NMR Signal and Pulse Sequences

The NMR signal is collected during the spiraling-upward relaxation motion of the magnetization vector by means of coils: the precessing magnetization induces an electromotive force (*emf*) as a consequence of the variation of the magnetic flux, as described by the *Faraday's law of induction*

$$emf = -\frac{d\Phi}{dt} \tag{15}$$

where Φ represents the magnetic flux of a magnetic induction $\boldsymbol{B}$ through a coil with infinitesimal surface element $d\boldsymbol{S}$

$$\Phi = \int_{coil\,area} \boldsymbol{B} \cdot d\boldsymbol{S} \tag{16}$$

and can be demonstrated that the signal $S(t)$ of an NMR experiment (usually few μV) assumes the form

$$S(t) = -\frac{d\Phi}{dt} = -\frac{d}{dt}\int_{sample} d^3r\, \mathfrak{B}^{receive}(\boldsymbol{r}) \cdot \boldsymbol{M}(\boldsymbol{r}, t) \tag{17}$$

where $\mathfrak{B}^{receive}$ is the magnetic induction per unit of induced current, generated by the motion of $\boldsymbol{M}$.
The NMR spectrum is related to the received signal $S(t)$ in the time domain through the Fourier transform

$$f(\omega - \omega_0) = \int dt\, S(t)\, e^{i\,2\pi\,(\omega-\omega_0)\,t} \tag{18}$$

and is composed of a set of absorption lines of the investigated nuclei in the frequency domain.

Free Induction Decay

The simple case described above in the previous Section corresponds to the simplest NMR experiment, in which the signal is collected after a single initial $\pi/2$ rf pulse (see Fig. 5): this experiment is called *Free Induction Decay* (FID), and produces an oscillating signal in the laboratory frame, the envelope of which is characterized by the T_2^* decay.

Spin-Echo and CPMG

To reverse the effect of the signal loss due to the external magnetic induction inhomogeneities (T_2'), which cause the spins to dephase relatively to each other as they experience different field strengths, a second 'refocusing' π-pulse can be applied with respect to FID experiment (see Fig. 6): this sequence is called *Spin-Echo* (SE) since it causes an 'echo' of the signal by nulling the relative accumulated phases of the spins (after the π-pulse, the spins which had previously accumulated extra positive phase now accumulate the negative of that phase, and *vice versa*). Noticed that the intrinsic losses characterized by the T_2 relaxation times are not recoverable because they are related to local, random, and time-dependent field variations.

In non-solid samples, as liquids, gels and gases, the Brownian motion may cause the diffusion of molecules resulting in a signal loss $\propto \exp(-\alpha t^3)$ that can rival and even dominate the intrinsic irreversible T_2 decay, where

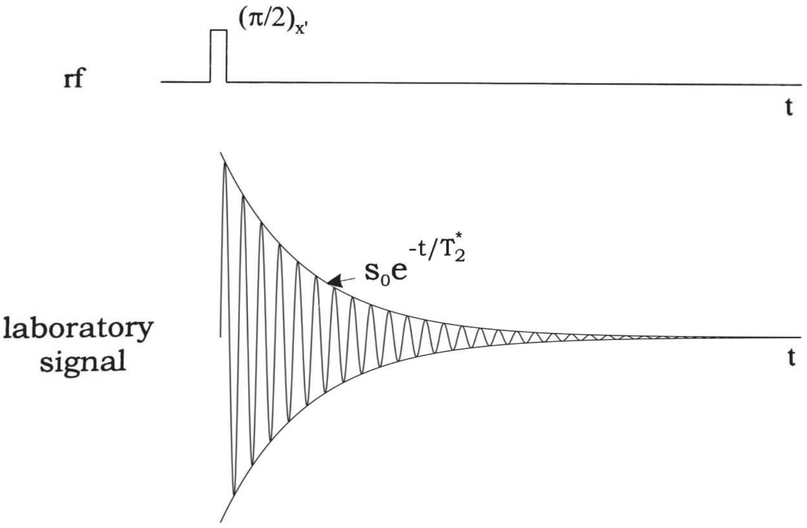

Figure 5: Sequence diagram (top) and related acquired signal (bottom) of a FID experiment. The envelope of the signal in the laboratory frame decays exponentially with rate constant $R_2^* = 1/T_2^*$. Source [4].

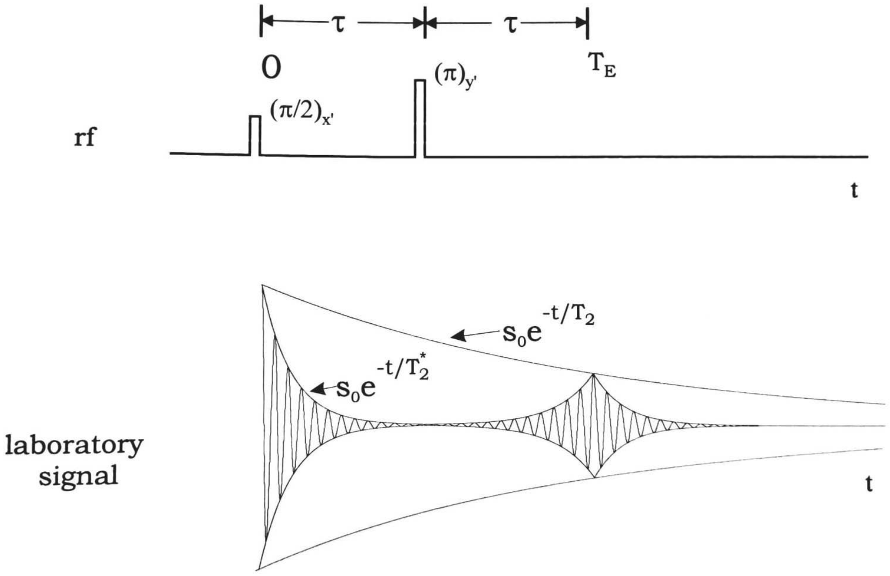

Figure 6: Sequence diagram (top) and related acquired signal (bottom) of a SE experiment. If we apply the π-pulse after a time τ with respect to the $\pi/2$-pulse, the echo will be formed at $t = 2\tau = T_E$, called *echo-time*. The envelope of the echoes decays exponentially with rate constant $R_2 = 1/T_2$. Source [4].

α depends on the diffusion constant, on the external field gradient and on the gyromagnetic ratio. To suppress the diffusion effects, the *Carr-Purcell-*

Meiboom-Gill (CPMG) pulse sequence can be employed (see Fig. 7): a train of π-pulses is applied to prevent the build-up of phase accumulation for a given spin random walk.

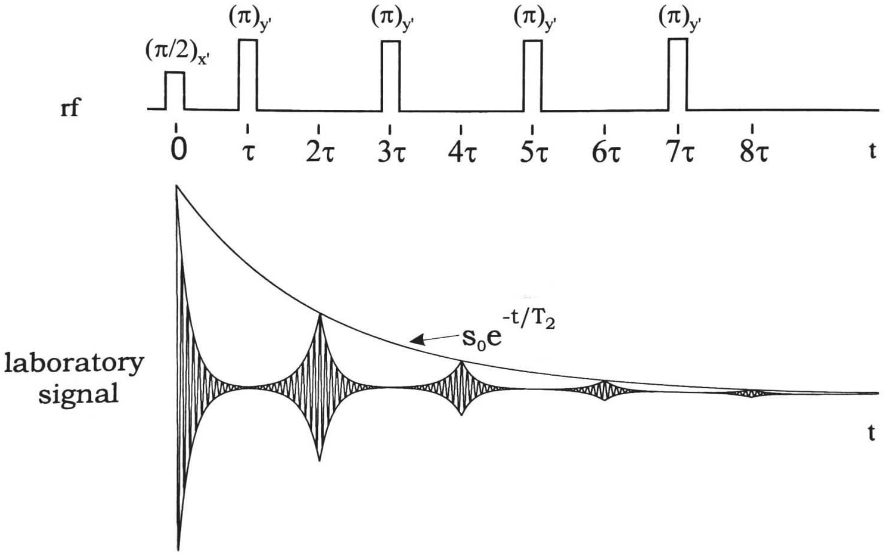

Figure 7: Sequence diagram (top) and related acquired signal (bottom) of a CPMG experiment. The π-pulse are applied at $t = (2n+1)\tau$ (with $n = 0, 1, 2, ...$), while the echoes are formed at $t = 2m\tau$ (with $m = 1, 2, 3, ...$). The envelope of the echoes decays exponentially with rate constant $R_2 = 1/T_2$. Source [4].

SATURATION AND INVERSION RECOVERY

The measurement of T_1 can be performed using either the *Saturation Recovery* (SR, Fig. 8) or the *Inversion Recovery* (IR, Fig. 9).

The main difference between the two pulse sequences is that SR applies as a first excitation a $\pi/2$-pulse, hence nulling the longitudinal component of the magnetization vector, while IR uses a π-pulse as a first excitation in order to invert the longitudinal component of the magnetization vector. After the first excitation pulse, the signal can be detected by means of a FID or a SE readout (this latter is the case of Fig. 8 and Fig. 9).

The regrowth of the longitudinal component of the magnetization vector is sampled at different times after the initial excitation pulse (τ_{sat}, or *saturation time*, for SR; T_I, or *inversion time*, for IR).

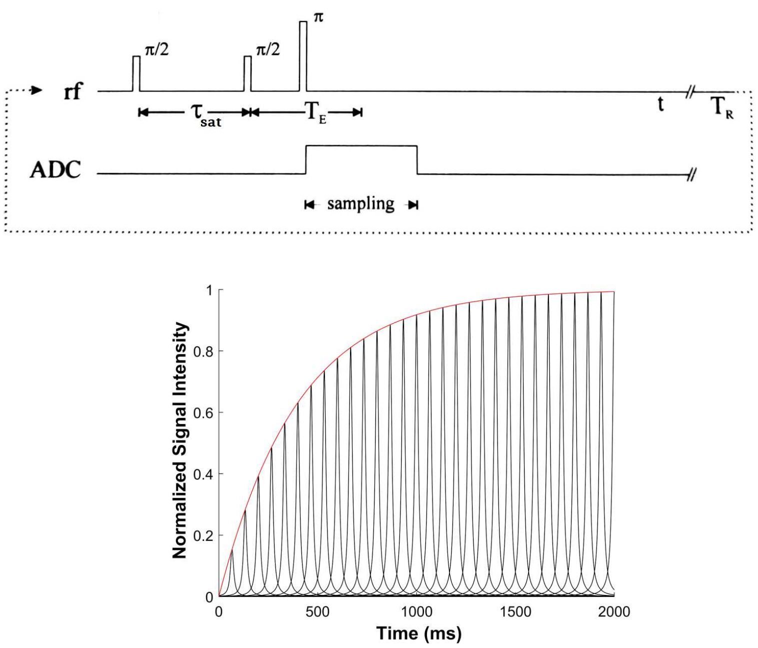

Figure 8: Sequence diagram (top) and signals collected at different τ_{sat} (bottom) of a SR experiment using a SE readout (a FID readout can also be used). The envelope of the echoes (red curve) follows the expression $M_z(t)/M_0 = 1 - \exp(-t/T_1)$. T_R indicates the *repetition time* of the sequence. Source [4].

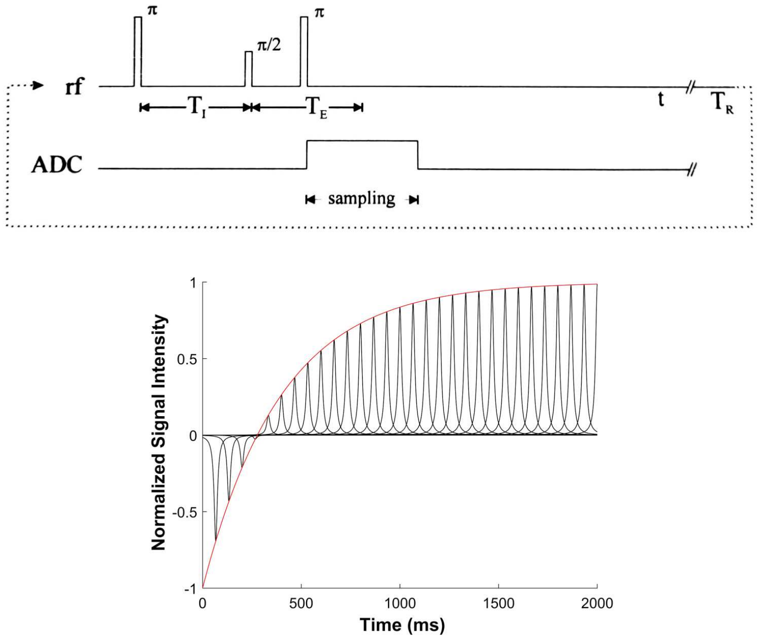

Figure 9: Sequence diagram (top) and signals collected at different T_I (bottom) of a IR experiment using a SE readout (a FID readout can also be used). The envelope of the echoes (red curve) follows the expression $M_z(t)/M_0 = 1 - 2\exp(-t/T_1)$. T_R indicates the *repetition time* of the sequence. Source [4].

2.2 MAGNETIC RESONANCE IMAGING

The *Magnetic Resonance Imaging* (MRI) is a non-invasive technique for the visualization of human body tissues and organs as a support for medical diagnosis.
Starting from the work of Lauterbur and Mansfield in 1973 [3, 28] (awarded by the Nobel Prize in Medicine in 2003) and thanks to the recent improvement in MRI scanner technology and parallel imaging reconstruction techniques, nowadays MRI has become a mature imaging modality that is considered the gold standard for many clinical applications, despite its high costs and low sensitivity which usually lead to poorer resolutions and longer scan times with respect to other imaging techniques such as CT (Computed Tomography).

NOTE Following the usual nomenclature in the MRI field, in this Section the magnetic induction $\boldsymbol{B}$ will be referred to as *magnetic field*.

2.2.1 Image Construction

An MRI image is acquired by performing a *spatial encoding* of the NMR signal: this can be achieved modifying locally the intensity of the static magnetic field B_0 by employing magnetic field gradients G_α, generated by means of dedicated coils, along the three principal spatial directions $\alpha = x, y, z$, hence obtaining a local intensity of the magnetic field given by $B_\alpha = B_0 + \alpha G_\alpha$, so

$$G_\alpha \equiv \frac{\partial B_\alpha}{\partial \alpha} \quad \text{with} \quad \alpha = x, y, z \tag{19}$$

Frequency Encoding

The *frequency encoding* is a spatial encoding method that exploits the strict correlation generated by the frequency-encoding gradient, applied in a specific direction, between a distinct spatial location and its Larmor frequency. As can be seen in Fig. 10, the Fourier Transform (FT) of the acquired time-domain NMR signal unravels the intensity of the frequencies present in the signal, which are linearly related to the positions along the gradient direction.

Let us assume that a linear gradient is applied along the x direction, in general $G_x(t)$, then the Larmor resonance frequency will depend on the x position according to

$$\omega(x,t) = \omega_0 + \omega_G(x,t) = \gamma(B_0 + x\,G_x(t)) \tag{20}$$

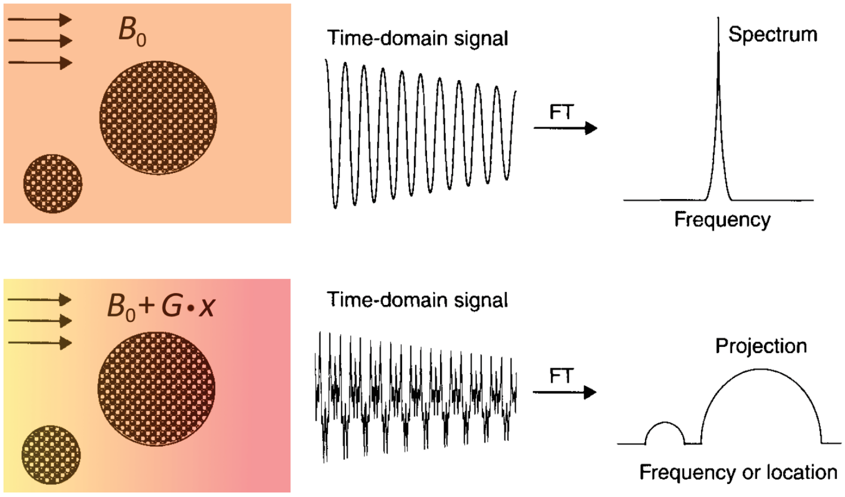

Figure 10: NMR signals without (top) and with (bottom) a frequency-encoding gradient G along the x direction. With the static magnetic field B_0 alone, FT of the time-domain NMR signal is composed by only one resonance frequency ($\omega = \gamma B_0$), while the spectrum of the NMR signal acquired with the frequency-encoding gradient is composed by a range of resonance frequencies ($\omega = \gamma(B_0 + G \cdot x)$). Source [29].

Neglecting the relaxation terms, considering (20) and assuming $M_0(\boldsymbol{r}) = M_0(x) \propto \rho_0(x)$, it can be demonstrated that the signal (Eq. 17) assumes the form

$$s(t) = \int dx\, \rho(x)\, e^{i\,\phi_G(x,t)} \tag{21}$$

where

$$\phi_G(x,t) = -\int_0^t dt'\, \omega_G(x,t') = -\,\gamma\, x \int_0^t dt'\, G_x(t') \tag{22}$$

is the accumulated phase, up to time t, due to the applied gradient (at time $t = 0$).

Equation (21) can be rewritten as

$$s(k_x) = \int dx\, \rho(x)\, e^{-i\,2\pi\, k_x\, x} \tag{23}$$

where the time dependence resides implicitly in the spatial frequency $k_x = k_x(t)$ with

$$k_x(t) = \frac{\gamma}{2\pi} \int_0^t dt'\, G_x(t') \tag{24}$$

Equation (23) shows that, when linear gradients are used, the signal $s(k_x)$ is the Fourier transform of the spin density of the sample which can be found, therefore, taking the inverse Fourier transform of the signal:

$$\rho(x) = \int dk_x\, s(k_x)\, e^{+i2\pi k_x x} \tag{25}$$

Since the signal $s(k_x)$ and the image $\rho(x)$ are a 'Fourier transform pair', is important to collect the signal over a sufficiently large set of k values: a good coverage of k-space is required.
In the case where the applied gradient is constant over the whole time interval, (24) reduces to

$$k_x = \frac{\gamma}{2\pi} G_x t \tag{26}$$

which states that, to collect a uniform distribution of points in k-space, it is only necessary to sample the signal at a constant rate in the presence of a constant gradient, sampling both positive and negative values of k by changing the sign of the gradient.

Phase Encoding

In analogy with frequency encoding, *phase encoding*, also known as *Fourier encoding*, generates a linear spatial variation of the magnetization phase in the orthogonal direction with respect to the frequency encoding one. The phase encoding is usually performed while the magnetization is flipped in the transverse plane (see Fig. 11).

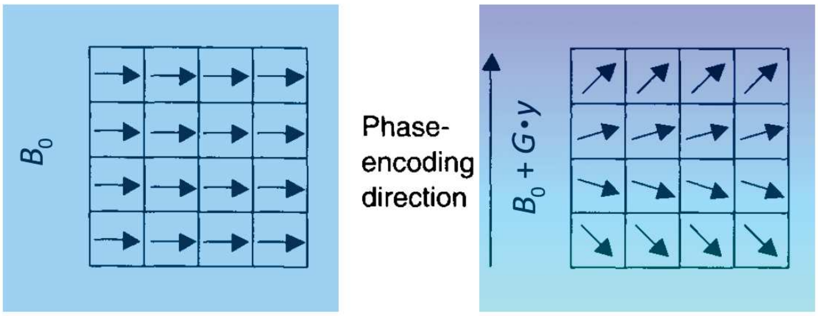

Figure 11: Effect of a phase-encoding gradient on an object divided in 16 pixels: the phase of the magnetization is varied at each location along the phase-encoded direction. Source [29].

The signal detected after the application of the phase-encoding gradient can be expressed as

$$s(k_y) = \int dy M_\perp(y)\, e^{-i\phi_G(y,t)} \rightarrow \sum_{n=0}^{N-1} M_\perp(n\Delta y)\, e^{-i2\pi\,(n\Delta y)\,k_y} \tag{27}$$

where the right part of Eq. 27 is the discrete approximation of the signal with $y = n\Delta y$, and Δy and N are the size and the number of pixels, respectively. Using N phase encoding steps with N different values of G_y a complete reconstruction of $M_\perp(n\Delta y)$ can be performed.

K-space Coverage

From the combination of frequency and phase encoding, the fully sampling of the k-space can be done: the final image is eventually obtained applying the Fourier transform to the acquired k-space. In Fig. 12 an example of a k-space coverage is shown.

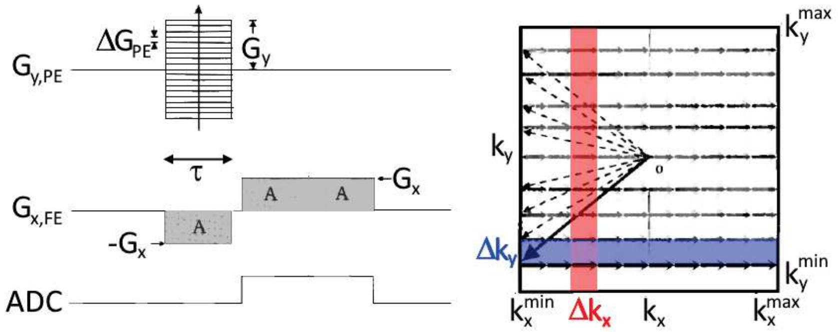

Figure 12: K-space coverage: the frequency encoding (FE) and the phase encoding (PE) are applied respectively along the x and y direction. The signal can be considered to be initialized at $k_x = k_y = 0$. The combined effect of the phase encoding lobe (at a given step) and the dephasing lobe of the frequency encoding moves the signal to a chosen k-space value along a diagonal trajectory. The read gradient is then reversed in order to sample all the k-space line along k_x, leaving k_y unaltered. The process is repeated for every phase-encoding steps.
$k_\alpha^{max/min} = \pm(\gamma/2\pi)\, G_\alpha \tau$ with $\alpha = x, y$; $\Delta k_x = (\gamma/2\pi)\, G_x\, 2\tau/N_x$ with N_x being the number of acquisition time steps; $\Delta k_y = (\gamma/2\pi)\, \Delta G_{PE}\, \tau$. Source [4].

Slice Selection

The selection of a thin slice of the body to be imaged through the frequency and phase encoding methods described above, is performed combining a *slice-selection* gradient and a 'spatially selective' rf pulse. The slice can be selected in one of the principal standard planes (see Fig. 13) or in any arbitrary oblique direction, employing a linear combination of the three physical gradients G_α (with $\alpha = x, y, z$).

To excite a slice of finite thickness with identical phase and flip angle across the slice itself a range of frequency Δf, or *spectral bandwitdh*, must be uniformly excited (see Fig. 14): therefore the analytic form of the rf excitation profile in the frequency-domain must be a boxcar function, which implies that the shape of the rf pulse in the time-domain is a sinc function.

Since the slice-selection gradient induces dephasing of the transverse magnetization across the slice, a *rephasing*, or *refocusing*, gradient is added after the end of the rf excitation pulse in order to correct the phase accumulation (see Fig. 15).

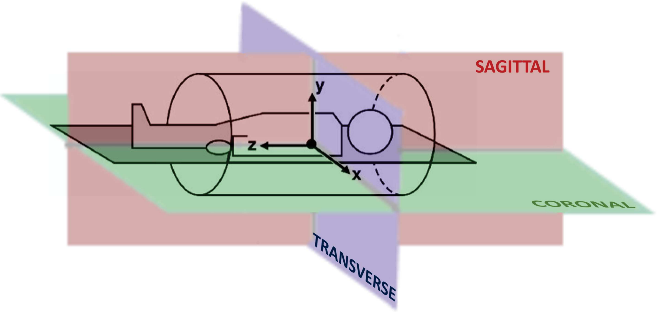

Figure 13: Standard slice planes of a whole-body MRI acquisition: *transverse*, or *axial* (blue); *sagittal* (red); *coronal* (green).

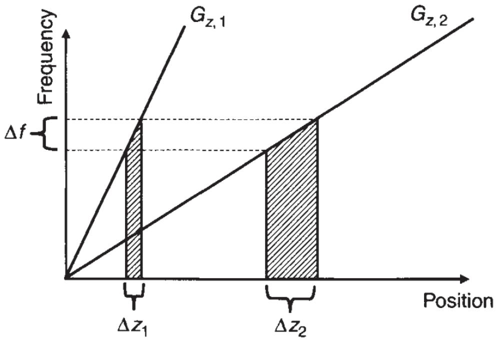

Figure 14: Plot of the resonance Larmor frequency as a function of the position along the direction of the slice-selection gradient. For a given bandwidth Δf, the higher gradient strengths imply thinner slices ($G_{z,1} > G_{z,2} \Rightarrow \Delta z_1 < \Delta z_2$). Source [29].

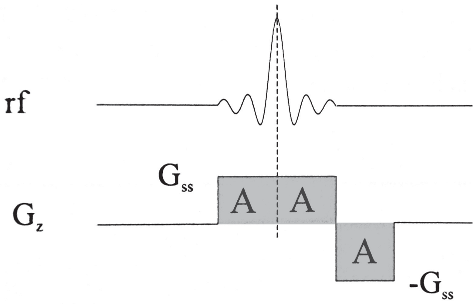

Figure 15: A slice-selection gradient G_{SS} (with the related rf excitation pulse) and the reversed lobe of the rephasing gradient $-G_{SS}$. It can be demonstrated that the area under the rephasing gradient (A) must be half of the area under the slice-selection gradient (2A). Source [4].

2.2.2 Noise and Contrast

An image acquisition can be affected by either random or systematic *noise*: the SNR (Signal-to-Noise Ratio) permits to quantify the voxel signal relative to the noise.
The SNR is defined as the ratio between the signal S and the noise standard deviation σ_{noise}

$$\mathrm{SNR} \equiv \frac{S}{\sigma_{noise}} \tag{28}$$

If the SNR is not high enough, it becomes impossible to differentiate tissues from one another or the background.
Noise derives from random fluctuations in the receive coil electronics and in the sample, from the digitization process noise and from pseudo-random ghosting due to the moving spins.
The variance of the fluctuating noise is

$$\mathrm{var}(emf_{noise}) = \sigma^2_{noise} \propto k_B T\, R\, \Delta f \tag{29}$$

where R is the effective resistance representing the sum of the body, coil and electronic components, T is the absolute temperature and Δf is the bandwidth of the detecting system.

An improvement of the SNR can be obtained repeating an imaging experiment N times and averaging the signal over these N measurements: the signal accumulated then becomes proportional to N, but noise, that is random and statistically independent from one repetition to another, grows proportionally to $\sqrt{N}$. Thus, the signal-to-noise ratio increases as

$$\mathrm{SNR} \propto \frac{N}{\sqrt{N}} = \sqrt{N} \tag{30}$$

The ability to distinguish between diseased and neighboring normal tissues depends not only on the SNR but also on the CNR (Contrast-to-Noise Ratio).

If tissues under investigation are labeled A and B, the difference of their signal is defined as the *contrast*:

$$C_{AB} \equiv S_A - S_B \tag{31}$$

The CNR is defined as the ratio of the contrast to the noise standard deviation

$$\mathrm{CNR} \equiv \frac{C_{AB}}{\sigma_{noise}} = \frac{S_A - S_B}{\sigma_{noise}} = \mathrm{SNR}_A - \mathrm{SNR}_B \tag{32}$$

The CNR is a more appropriate measure of the ability to distinguish a change in the signal of adjacent but different object, since it keeps in count the amplitude of the noise that may obstacle the differentiation.

Weighted Images

A signal collected using a classical Spin-Echo sequence can be expressed in terms of both the intrinsic parameters of the tissue visualized in a certain pixel ($\rho(^1\mathrm{H})$ = proton density, T_1 = spin-lattice relaxation time, T_2 = spin-spin relaxation time) and of the acquisition parameters of the sequence that can be set by the user (T_E = echo-time, T_R = repetition time):

$$S(t) \propto \rho(^1\mathrm{H})\, e^{-T_E/T_2}\, (1 - e^{-T_R/T_1}) \tag{33}$$

To enhance the contrast or to highlight some properties related to specific MR parameters (spin density or relaxation times) in images obtained by MR devices, it is necessary to choose carefully the values of the acquisition parameters: the different types of contrast can be used in the clinical practice to establish if a tissue is normal or pathologic (see Figure 16). A set of general rules for choosing T_E and T_R are outlined in Table 1.

Table 1: General set of rules for generating tissue contrast in MRI.

Type of contrast	T_R	T_E
Spin density (PDW)	$T_R \gg T_1$	$T_E \ll T_2$
T_1-weighted (T_1W)	$T_R \lesssim T_1$	$T_E \ll T_2$
T_2-weighted (T_2W)	$T_R \gg T_1$	$T_E \lesssim T_2$

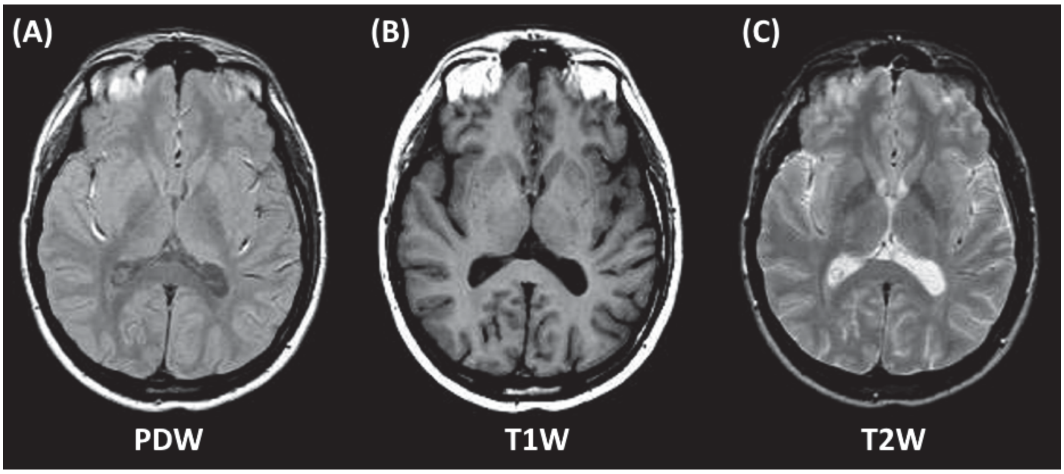

Figure 16: Different types of contrast: (A) spin, or proton, density-weighted, (B) T_1-weighted and (C) T_2-weighted. Source [4].

2.2.3 Relaxation Time Mapping

Relaxation time maps are MRI images whose pixels report the exact value of the relaxation times (T_1, T_2 or T_2^*) of the represented tissue (usually in units of ms). Their dual nature of qualitative and quantitative images make them a powerful instrument in medical applications. Since the relaxation times of human body water proton depends on the interactions with the surrounding environment, relaxation time maps can be used to identify tissue and morphological changes that can be correlated to pathologies and used to monitor disease progressions [5].

The conventional relaxation time mapping technique consists in acquiring several images of the same body slice adjusting the acquisition parameters in order to generate a series of images whose pixel-wise intensities can be characterized in terms of the solutions of the Bloch equations. Such characterization, usually performed by means of a fitting of the signal intensities, allows to extrapolate the values of T_1 or T_2 of the tissue represented in each pixel. T_2^* maps are beyond the scope this thesis and therefore they will be non longer considered.
The typical MRI sequences employed for the construction of T_1 and T_2 relaxation time maps are:

- *SE*, or *TSE* (Spin-Echo or Turbo Spin-Echo [30]): all the parameters are kept fixed with the exception of T_E, usually varied from few milliseconds up to hundreds milliseconds. According to Eq. 33, the signal in each pixel will decay exponentially with time constant T_2. A pixel-wise fit of the signal intensities along the image series (acquired with different T_Es) allows to create another image assigning to each pixel the fitted T_2 values. From this process, a T_2 map is obtained.
  Noticed that keeping fixed all the parameters and varying T_R, according to Eq. 33, also a T_1 map can be retrieved.

- *IR*, or *IR-TSE* (Inversion Recovery, *i.e.* SE or TSE with an initial π inversion rf-pulse): all the parameters are kept fixed with the exception of T_I, usually varied from tens milliseconds up to thousands milliseconds. The signal in each pixel will regrow exponentially with time constant T_1 according to

$$S(t) \propto \rho(^1\mathrm{H})\, e^{-T_E/T_2}\, (1 - 2e^{-T_I/T_1} + e^{-T_R/T_1}) \qquad (34)$$

  A pixel-wise fit of the signal intensities along the image series (acquired with different T_Is) allows to create another image assigning to each pixel the fitted T_1 values. From this process, a T_1 map is obtained.
  Notice that IR and IR-TSE are preferred over SE and TSE for T_1 mapping thanks to the higher SNR of the acquired images.

The greatest disadvantage of the above mentioned sequences is the long acquisition time needed that makes these sequences unfeasible for clinical practice: in fact, in order to guarantee a full recovery of the magnetization vector, a long T_R is required in each phase encoding step.

Many MRI sequences have been developed over the years in order to fasten the acquisition without losing in efficiency (accuracy and precision). Hereafter are presented the two sequences used in this thesis work, developed in the challenging field of the cardiac MRI, characterized by a good reproducibility and extremely short acquisition time (order of seconds).

MOLLI

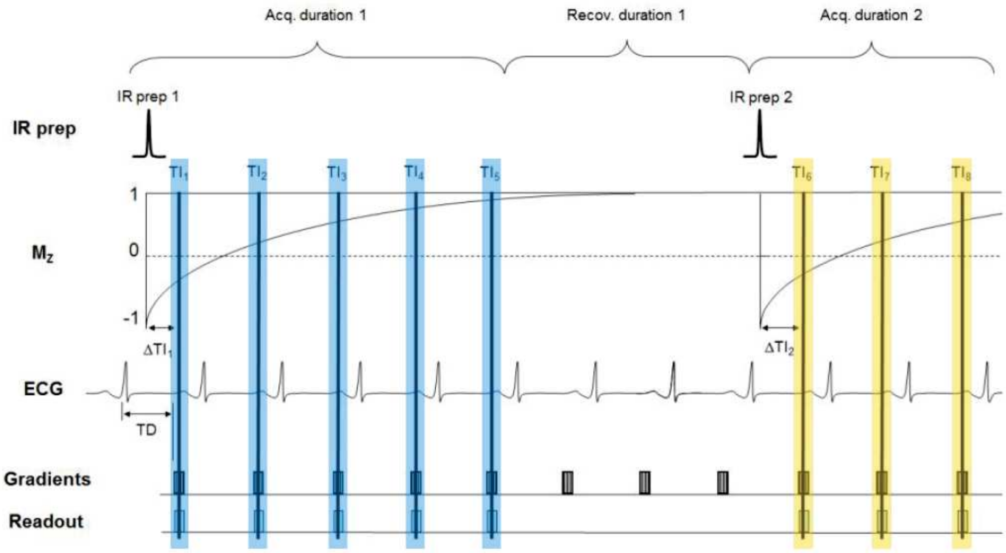

Figure 17: MOLLI acquisition scheme composed of 2 Look-Locker (LL) experiments characterized by 2 different inversion times ($\Delta T_{I,1}$ and $\Delta T_{I,2}$) with 5 and 3 ECG-triggered samplings of the recovery curve. Each sampling is performed at a fixed time TD after the ECG wave in order to acquire the signal in the same phase of the cardiac cycle. Source [31].

Firstly presented in 2004 by Messroghli *et al.* [32], the MOLLI sequence (Modified Look-Locker Inversion Recovery) allows the *in vivo* T_1 mapping within a single breath-hold. The MOLLI pulse sequence scheme used in the present work is illustrated in Fig. 17 [33].

The conventional Look-Locker sequence (LL) is similar to an IR pulse sequence, but instead of a single sampling of the recovery curve per T_R it applies a train of low flip angle impulses spread across the T_R.

MOLLI scheme introduces two principles to the standard LL sequence:

1. Selective data acquisition at a given time of the cardiac circle over successive heartbeats;

2. Merging of image sets from multiple LL experiments with varying inversion time into one data set.

Two successive ECG-triggered LL experiments (with two different ΔT_Is) were carried out with five and three single-shot readouts: images are acquired with single-shot TrueFISP sequence [34] at different inversion times after a single inversion pulse, all gated to the same cardiac phase. By combining several inversions with slightly shifted T_I times within one protocol, the relaxation curve is sampled in a interleaved manner, resulting in a sufficient number of points for T_1 quantification acquired within a single breath-hold, as can be seen in Fig. 17 (11 heartbeats ca.).

Images are sorted according to their accumulative time from inversion t, which is given by

$$t = \Delta T_I + (n-1)TD \tag{35}$$

where n is the image number within the LL experiment, and TD is the heartbeat interval.

Three-parameters nonlinear curve fitting is then performed pixel per pixel for map generation using the following equation

$$y = |\mathrm{A} - \mathrm{B}\, e^{-t/T_1^*}| \tag{36}$$

where y denotes signal intensity and T_1^* corresponds to the apparent, modified T_1 in a LL experiment due to the effect of the readout that drives the IR to recover more quickly and to reach a steady state that is less than the equilibrium magnetization M_0. T_1 is then calculated from the resulting parameters A, B and T_1^* by applying the conventional Look-Locker correction

$$T_1 = T_1^* \left(\frac{\mathrm{B}}{\mathrm{A}} - 1 \right) \tag{37}$$

The T_1 map formation process is illustrated in Fig. 18.

ACCURACY, PRECISION AND REPRODUCIBILITY The performance of quantitative methods may be assessed and compared in terms of accuracy and precision: accuracy relates to systematic bias errors whereas precision relates to random errors due to noise.

Kellman *et al.* [35] listed factors influencing the accuracy of T_1 measurements using inversion recovery methods as MOLLI:

- *Sensitivity to* T_2: TrueFISP readout and the imperfect inversion efficiency lead to a T_2 dependent error in the estimate of T_1. The effect the inversion efficiency can be minimized by using a short duration inversion pulse.
- *Off-resonance*: it causes banding artifacts using a TrueFISP readout. Reducing the flip angle will decrease the off-resonance related error at the expense of a reduction of SNR causing a loss of precision.
- *Heart rate*: the original MOLLI protocol exhibited a large sensitivity to heart rate for long T_1 values: by modifying protocols (number of inversions, time between inversions and influence of the TrueFISP readout flip angle during each inversion) the heart rate sensitivity has been reduced.

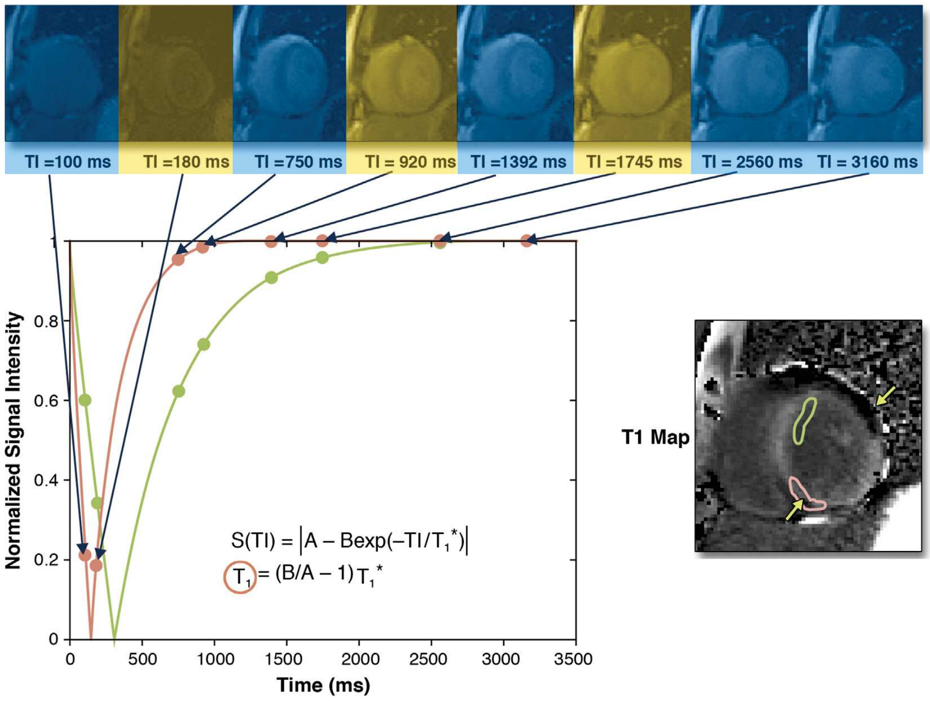

Figure 18: T_1 map generation from MOLLI acquisition (Fig. 17). Source [7]

- *Flip angle*: it affects the T_1 measurement accuracy of MOLLI on-resonance, the off-resonance behaviour, the heart rate sensitivity and the SNR: an increasing T_1 underestimation was observed for increasing flip angle.
- *Blood flow*: it has two effects:
  1. From beat to beat the blood is moving and mixing such that the slice selective TrueFISP readout from a given beat does not influence the next (Look-Locker correction is not required);
  2. An apparent shorter T_1 is observed because of the flow of the non-inverted blood from outside the z-FOV (or the magnet) with the inverted blood.
- *Partial volume effect*: T_1 mapping methods assume that the voxel is comprised of a single tissue species and not a mixture. Loss of resolution may occur due to cardiac motion with high heart rates (tachycardia) or for subjects with Heart-Rate Variability (HRV, arrhythmia).
- *Magnetization transfer*: intracellular bound pool of protons exchanges with the free pool of protons and can thus reduce the signal from the free pool. It leads to a significant underestimation of apparent T_1 [36].

The precision depends on the SNR of the raw images and the number and location of samplings along the recovery curve.

The reproducibility of T_1 mapping can be reduced if the described factors influencing the accuracy and the precision, which depend on the protocol or scanner adjustment, are not well controlled.

Inversion Recovery methods such as MOLLI have excellent precision and are highly reproducible, but the accuracy is affected significantly by magnetization transfer (MT) that causes an underestimation of the spin-lattice relaxation time [9].

T_2-PREP TRUEFISP

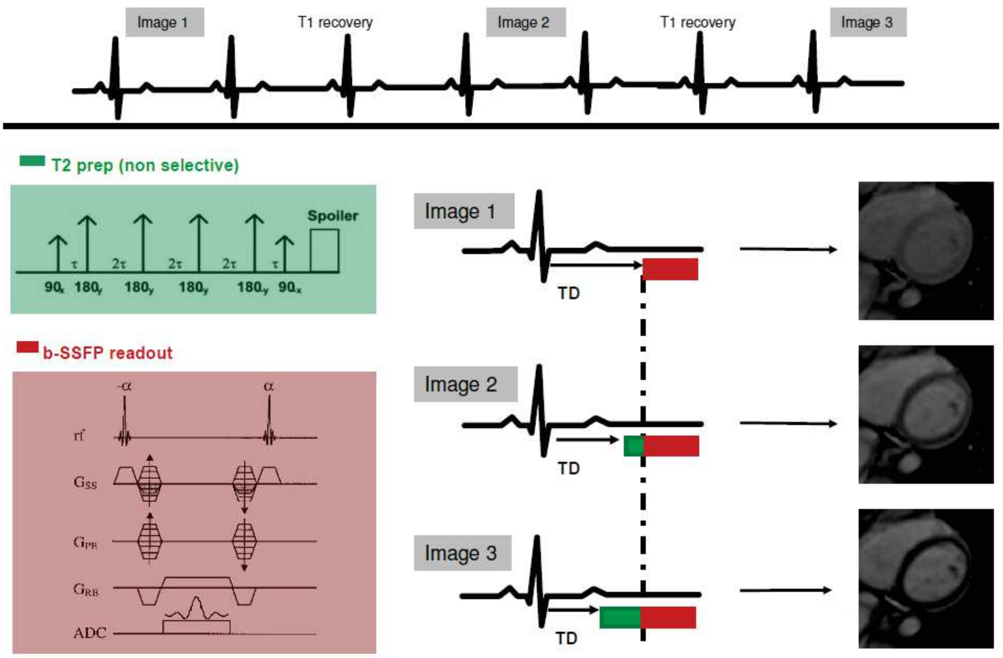

Figure 19: T_2-prep TrueFISP acquisition scheme composed of 3 samplings characterized by different $T_{E,prep}$s, each followed by a TrueFISP (or b-SSFP) readout. Each sampling is performed at a fixed time TD after the ECG wave in order to acquire the signal in the same phase of the cardiac cycle. Source [37].

Proposed by Huang *et al.* in 2007 [38], the T_2-prep TrueFISP is a fast, high contrast, high SNR and motion-insensitive sequence that combines T_2 magnetization preparation with TrueFISP (or *b-SSFP*, balanced-Steady-State Free Precession) imaging, whose acquisition scheme is reported in Fig. 19.

The T_2 preparation part was previously described by Brittain *et al.* [39]: it consists in an iterative Carr-Purcell Malcolm-Levitt (MLEV) sequence, *i.e.* a $(\pi/2)_x$ excitation pulse followed by four equally spaced $(\pi)_y$ composite refocusing pulses, which provide a more uniform off-resonance behaviour; the magnetization is returned back to the longitudinal direction by a $(-\pi/2)_x$ composite pulse. Each of the rf pulses are non-spatially-selective and a crusher gradient is employed after the T_2-preparation sequence to spoil any residual transverse magnetization. Increasing MLEV train lengths ($T_{E,prep}$) are employed to vary the T_2 sensitivity.

After the T_2-preparation sequence, the TrueFISP imaging sequence is applied. It is characterized by completely balanced gradients in all direction during each repetition time and the echo occurs in the middle of the readout period, halfway between consecutive rf pulses. A 180° phase alternation between consecutive rf pulses maximizes image SNR and maintains a relative uniform signal response to resonance offset angles. The TrueFISP imaging requires the continuous application of rf pulses to maintain the magnetization in a steady-state.

The T_2 mapping is performed in a breath-hold fashion with the trigger delay (TD) and acquisition window that could possibly been set during both diastole (most of all) and systole (if a thicker myocardium is desired), as can be seen in Fig. 19.

The T_2-prep TrueFISP sequence produces single-shot T_2-weighted images, each with different $T_{E,prep}$ preparation times: T_2 relaxation time is measured by performing a curve-fitting on the following two-parameters equation

$$y = A\, e^{-T_{E,prep}/\,T_2} \tag{38}$$

where y is the signal intensity.
T_2 maps are generated by fitting Eq. 38 to signals of corresponding pixels from each image with different T_2 preparation times $T_{E,prep}$ (see Fig. 20).

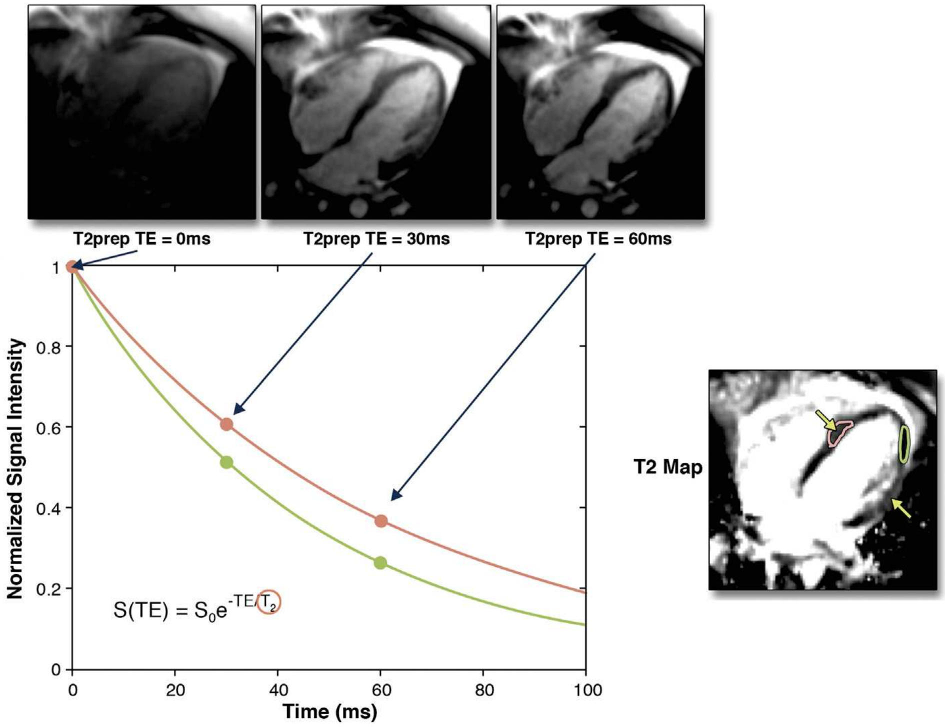

Figure 20: T_2 map generation from T_2-prep TrueFISP acquisition. Source [7]

CONSIDERATIONS Giri *et al.* [37] showed that T_2-prep TrueFISP is a rapid and practical technique for quantitative T_2 mapping that settles limitations associated with conventional T_2-weighted imaging:

- *Motion sensitivity*: T_2 values are unaffected by the location of the acquisition window in cardiac cycle; in addiction, the TrueFISP readout is less sensitive to artifacts induced by cardiac arrhythmias or imperfect breath-hold than segmented *k*-space methods.
- *Surface coil intesity variation*: under conditions of severe surface coil signal inhomogeneity, the T_2-prep TrueFISP sequence shows a reduction of the mean coefficient of variation among myocardial segments.
- *Stagnant blood*: sub-endocardial bright signal artifact caused by stagnant blood is not observed in the T_2 maps generated by T_2-prep TrueFISP sequence.

Besides these advantages, an overestimation of T_2 values occurred in phantom results, while measurements in vivo concurred with the other values reported in literature. Giri *et al.* identified two probable causes of this inaccuracy:

1. The linear *k*-space ordering chosen for the b-SSFP readout instead of centric that provides an higher T_2 accuracy in phantoms but gives rise to artifacts in the in vivo images (due to off resonance) and has lower SNR.
2. The number of echo times and fitting method used. Huang *et al.* [38] also showed a moderate overestimation ($2 - 12\%$) between T_2-prep TrueFISP and MESE (Multi-Echo Spin-Echo) in phantom measurements of T_2 relaxation depending on the number of $T_{E,prep}$ steps (this error may occur because of signal decay during the magnetization preparation composite rf impulses). Akçakaya *et al.* [40] studied the impact of the fitting model on accuracy and precision: using a 3-parameter fit model and incorporating an additional image acquired with saturation preparation to the T_2-prep TrueFISP sequence, more accurate T_2 measurements can be achieved. Moreover, with the sequence proposed by Akçakaya *et al.*, T_2 measurements are independent of number and duration of $T_{E,prep}$ preparation times.

Inaccuracy in T_2 measurements can rise introducing some T_1 dependence to the values because of incomplete T_1 relaxation between each image acquisition (for example in tachycardiac patient).

Even at a segmental level, T_2 values obtained by the T_2-prep TrueFISP sequence appear to be highly reproducible and in good agreement with those obtained with different cardiac T_2 mapping sequences [10].

2.3 CONTRAST AGENTS

The aim of Contrast Agents (CAs) for medical MRI application is to cause a local increase of both nuclear longitudinal $R_1 = 1/T_1$ and transverse $R_2 = 1/T_2$ relaxation rates of tissues, thus obtaining a major sensitivity of the technique for diagnostic purposes. These magnetic systems, that enhance the image contrast where delivered, can be divided into two types (see Fig. 21):

- *Positive* CAs, that produce brighter zones reducing mainly T_1;
- *Negative* CAs, that cause darker spots reducing mainly T_2.

The MRI CAs have been extensively studied in the last 40 years and their use in clinic is widespread, especially at the most common fields employed, *i.e.* 1.5 and 3 T.
In this Thesis, the main focus is on paramagnetic dilute solutions CAs.

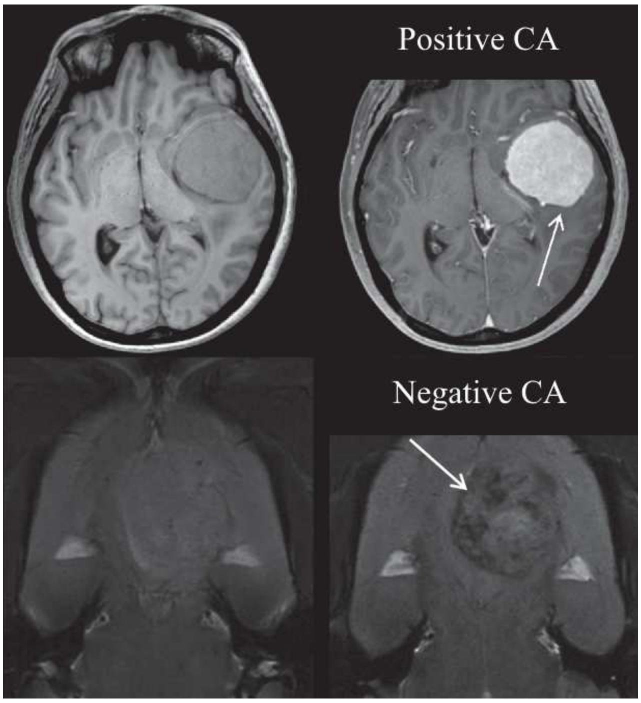

Figure 21: Effect of positive (top, [41]) and negative (bottom, [42]) contrast agents on the MRI images.

2.3.1 The Solomon-Bloembergen-Morgan Theory

The theory of spin relaxation induced by paramagnetic species in dilute solutions was developed by Solomon, Bloembergen and Morgan in the '50$_s$ ([17–19, 43]) after the pioneering work of Bloembergen *et al.* in 1948 [16].
Unpaired electrons in paramagnetic systems, characterized by positive magnetic susceptibility, affect the NMR spectra of solutions in which such systems are diluted in. The increase of relaxation rates, also named *Paramagnetic Relaxation Enhancement* (PRE), is caused by variations of the magnetic hyperfine interactions between the electron and nuclear spin, expressed by the hamiltonian

$$\mathcal{H} = \boldsymbol{I} \cdot \boldsymbol{A} \cdot \boldsymbol{S} \tag{39}$$

being $\boldsymbol{A}$ the hyperfine coupling tensor and $\boldsymbol{I}$ and $\boldsymbol{S}$ the nuclear and electron spin operator, respectively.

The hyperfine interaction can be split into three main components: (i) the *dipole-dipole* interaction between the nuclear magnetic moment and the electrons far from the nucleus; (ii) the *scalar interaction*, or *contact interaction*, between the nuclear magnetic moment and the electron spin density close to the nucleus site; (iii) the *Curie interaction* [44] between the nuclear magnetic moment and a large static time-averaged magnetic moment arising from the electrons (this effect is non-negligible at high-field).

The relaxation efficacy of a CA is called *relaxivity* (in units of $\mathrm{mM}^{-1}\ \mathrm{s}^{-1}$) and it is expressed as

$$r_i = \frac{1}{C}\left(\frac{1}{T_{i,obs}} - \frac{1}{T_{i,dia}}\right) \text{ with } i = 1,2 \tag{40}$$

where C is the molar concentration of the paramagnetic species (usually in units of mM = mmol l^{-1}), $1/T_{i,obs}$ are the observed relaxation rates of the solution, and $1/T_{i,dia}$ are the diamagnetic solvent relaxation rates (in absence of the paramagnetic species).
The paramagnetic relaxation rates $1/T_{i,par} = r_i C$ arise from the contributions of two main mechanism (see Fig. 22):

- *Inner-Sphere relaxation*, that considers the interactions of the solvent molecules (typically water) in the close proximity of the paramagnetic species and the propagation of such interactions towards the bulk solvent through chemical exchange. The parameters that influence this relaxation mechanism are: the lifetime τ_M (also known as 'exchange correlation time') and the number q of the solvent molecules in the so-called 'first coordination sphere' (also known as 'hydration number'); the distance between the paramagnetic species and the observed nucleus r; the rotational correlation time of the paramagnetic species τ_R; and the electronic relaxation times τ_{Si}.

- *Outer-Sphere relaxation*, that considers the effect of the random translational diffusion motion around the paramagnetic species. This mechanism depends on the distance of minimum approach for bulk water molecules to the paramagnetic center d (assuming a spherical symmetry) and the translational correlation time defined by $\tau_D = d^2/D$, where D is the solvent relative diffusion coefficient.

Correlation times

The concept at the basis of the Solomon-Bloembergen-Morgan (SBM) theory is the *correlation function* that, in general, provides the statistical correlation between random variables over time. For an ensemble of spins, in a magnetic field and at a given temperature, it can be demonstrated that the correlation function can be well approximated by an exponential decay function

$$C(t) \propto e^{-t/\tau_C} \tag{41}$$

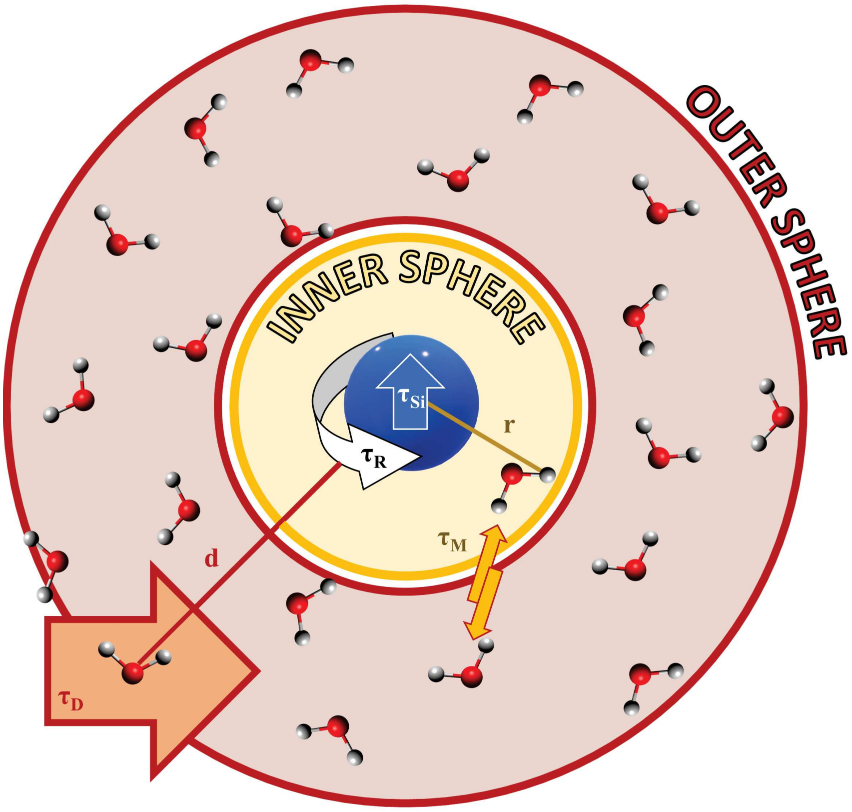

Figure 22: Relaxation in paramagnetic aqueous dilute solutions: Inner-Sphere and Outer-Sphere mechanisms. See text for the details on the reported quantities.

where the correlation time τ_C describes all the dynamic processes occurring in the system, such as electron motion, molecular rotation, vibrations and collisions.

In the frequency domain, the Fourier transform of the correlation function, called *spectral density*, has a Lorentzian shape:

$$J(\omega) = \frac{\tau_C}{1 + \omega^2 \tau_C^2} \tag{42}$$

that presents, as can be seen in Fig. 23, an inflection point (also called *dispersion*) at $\omega\tau_C = 1$.

As mentioned above, three main dynamic processes can affect and cause relaxation of nuclear spins and contribute to the decay of the correlation function: the spin relaxation, characterized by the electronic relaxation (correlation) time τ_{Si}; the molecular rotation, characterized by the rotational correlation τ_R; and the chemical exchange, characterized by the exchange correlation time τ_M.

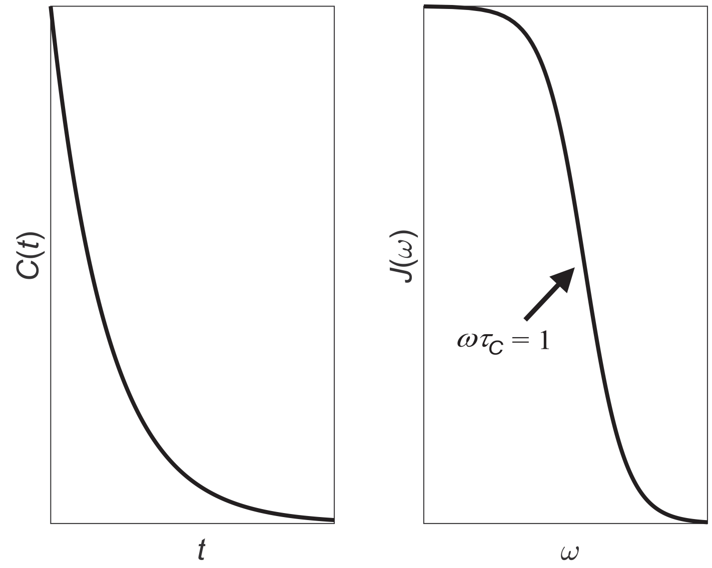

Figure 23: Exponential correlation function (left) and Lorentzian spectral density (right, abscissa in log-scale) connected by the Fourier transform. In the right graph is also indicated the dispersion point $\omega\tau_C = 1$.

Provided the independence of these mechanisms, the overall correlation function decays as

$$C(t) \propto e^{(-t/\tau_{Si})}e^{(-t/\tau_R)}e^{(-t/\tau_M)} \tag{43}$$

and hence

$$\tau_{C,DD}^{-1} = \tau_{Si}^{-1} + \tau_R^{-1} + \tau_M^{-1} \tag{44}$$

that provides the expression of the correlation time for the dipolar coupling (DD). The scalar, or contact, coupling (SC), which is mainly effective in the inner-sphere framework, is modulated by the chemical exchange and the electronic relaxation time only, so

$$\tau_{C,SC}^{-1} = \tau_{Si}^{-1} + \tau_M^{-1} \tag{45}$$

while Curie relaxation is determined by the molecular rotation and the chemical exchange

$$\tau_{C,Curie}^{-1} = \tau_R^{-1} + \tau_M^{-1} \tag{46}$$

Assumptions and limitations

The Solomon-Bloembergen-Morgan theory is based on several assumptions:

- Redfield limit condition, *i.e.* the motions in the spin systems must occur on a much slower timescale than those in the lattice;

- No correlation between the electron spin relaxation and the molecular reorientation;
- The electron Zeeman interaction dominates over other interactions, which cause only the relaxation of the electron spin.

Moreover: (i) the electron spin is assumed as a point dipole centered at the paramagnetic center (*e.g.* a transition metal ion), (ii) the electron g tensor is hypothesized isotropic, (iii) the molecular rotation is supposed isotropic and characterized by τ_R alone, and (iv) no correlations are considered between the chemical exchange and the lattice motions.

2.3.2 Fast Field-Cycling

The Nuclear Magnetic Resonance (NMR) characterization of CAs is performed by collecting nuclear relaxivity data, *i.e.* the relaxation rate increment (with respect to the solvent) normalized to 1 mM concentration of the CA, as a function of the Larmor resonance frequency $\nu = (\gamma/2\pi)B_0$, where γ is the gyromagnetic ratio of the nuclear species, usually ^{1}H, and B_0 is the applied static magnetic induction. The acquired data generate the so-called *Nuclear Magnetic Relaxation Dispersion* (NMRD) profiles, that can be analyzed according to models based on the Solomon-Bloembergen-Morgan (SBM) theory.

The acquisitions of the NMRD profiles must be performed in a wide range of frequencies (several orders of magnitude) for a proper efficiency and usefulness of their analysis through the SBM theory. In order to span such wide range of frequencies and fasten the measurements, the *Fast Field-Cycling* (FFC) NMR relaxometry is employed, taking advantage of the linear dependence from the external magnetic induction B_0 of the equilibrium value of the magnetization vector $M_0 \propto \gamma^2 B_0/T$ (with T being the temperature).

An FFC experiment for relaxometry purposes is usually composed by three steps (see Fig. 24):

1. *Preparation*, in which a strong 'polarization' induction B_P is either applied or not to the sample in order to build up a net starting nuclear magnetization M_0 or to start from the $M_0 = 0$ condition. We refer to the first case as *Pre-Polarized sequence* (PP), while the second case is known as *Non-Polarized sequence* (NP).
2. *Relaxation*, in which the magnetization of the sample, kept in a constant 'relaxation' magnetic induction B_R, relaxes from M_0 to $M(B_R)$. The duration of this part can be varied to sample all the relaxation steps of the magnetization vector going from M_0 to $M(B_R)$ (this is how T_1 can be measured).

3. *Detection*, the signal is collected using standard NMR sequences (FID, SE, CPMG) at an 'acquisition' magnetic induction B_A determined by the current operating frequency.

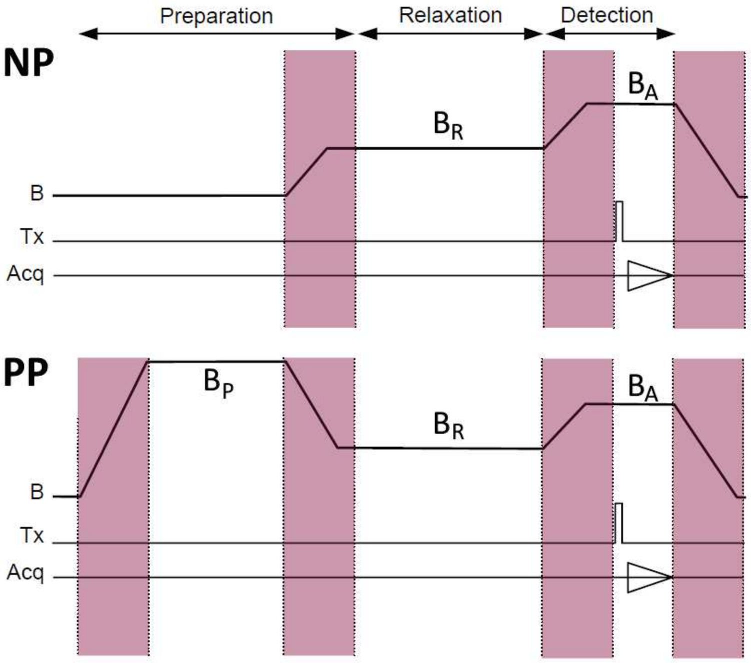

Figure 24: Non-polarized (top, NP) and pre-polarized (bottom, PP) FFC sequences. In purple are also indicated the switching transitions, performed with a constant switch-rate set by the user, between the applied magnetic inductions (polarization B_P, relaxation B_R and acquisition B_A).

3

RELAXATION TIME MAPS IN CLINICS: AN HARMONIZATION METHOD

A method for the harmonization of data from relaxation time maps for clinical application will be presented. The development of this method was carried out in collaboration with the Niguarda Hospital in Milan, Italy.

Part of the studies presented in this Chapter have been published on the Journal of Magnetic Resonance in a paper entitled *A method for T_1 and T_2 relaxation times validation and harmonization as a support to MRI mapping* by Cicolari *et al.* [45].

NOTE Following the usual nomenclature in the MRI field, in this Section the magnetic induction $\boldsymbol{B}$ will be referred to as *magnetic field*.

3.1 RATIONALE

The scaling of a parametric map taking as reference in-scan calibrating samples, hence resulting in a recalibration of the map, is a technique already used in '60_s at early stages of Computed Tomography (CT) applications [46, 47]. In fact, CT images, which are parametric maps displaying the absorption coefficients of tissues in Hounsfield Units (HU), are often scaled according to the reference HU values of samples scanned simultaneously with the patient. On the other hand, MRI often suffers from limited use of in-scan references for specific quantitative data acquisitions, a typical example being the ones using mapping sequences. In recent years, the technological developments of MRI scanners allowed the clinical introduction of such sequences [6], leading to the generation of parametric maps containing tissue physical properties: qualitative and quantitative information about such properties should be obtained through an appropriate image acquisition and analysis [48, 49].

The MRI parametric maps of the spin-lattice relaxation times (T_1) and of the spin-spin relaxation times (T_2) are typically created by acquiring multiple images of the same body slice with different sensitivity to the biophysical parameter of interest using the T_1- or T_2- "weighted" intrinsic contrast mechanisms on the MR signal. The signal intensity evolution of the obtained images is modeled with the phenomenological Bloch equations [1, 4] describing the relaxation behavior of the nuclear system, usually composed of hydrogen nuclei, decoupling the different relaxation time contrast mechanisms that contribute to the overall MR signal [4].
Nowadays, new fast acquisition sequences can be used for diagnostic purposes: the classical Spin-Echo (SE) [4] and Inversion Recovery (IR) [4] sequences and their turbo-analogous (TSE, IR-TSE), based on the RARE readout [30], have been turned into single breath-hold sequences suitable for clinical practice [7], such as the MOLLI (Modified Look-Locker Inversion Recovery) [32, 33] for T_1 measurements, and the T_2-prep TrueFISP (Fast Imaging with Steady Precession) [38] for T_2 measurements.
Relaxation time maps have been proven to be highly reliable instruments for the assessment of different pathologies in several body districts [5]. In fact, tissue and morphological changes, observable through deviations from the relaxation times normal values [50], can be correlated with several diseases, whose progression can be also monitored. Nevertheless, performing clinical diagnosis employing MRI pure relaxation times maps is a procedure that is highly affected by a low inter- and intra-center harmonization, due to differences in (i) the chosen methods of images acquisition [9, 10, 12, 51], (ii) the post-processing software, (iii) the whole data analysis work-flow employed [11, 40], and (iv) the used MRI scanners [8, 52].
The accuracy (true value proximity) and the precision (reproducibility) of relaxation time maps are mostly assessed taking as reference other maps generated from more standard techniques (IR/IR-TSE, SE/TSE), thus maintaining the mentioned contrast dependencies [8–13, 40, 51–53]. The same observations can be done for the development of new fast sequences (or upgrades of the existent ones) increasingly precise and accurate [54–59].

This study aims to set the basis for a 'novel' scanner-, software-, center-independent method for the validation and the harmonization of the data obtained from MRI relaxation time maps, which is based on $MnCl_2$ aqueous solutions used as calibrating samples. In this preliminary study, the samples' relaxation time values for ^1H nuclei extracted from the parametric maps acquired by means of different vendor clinical MRI scanners with different configurations are compared with reference T_1 and T_2 values estimated by means of an NMR laboratory spectrometer. It is worth mentioning that the first attempts of this kind of study were made in 1987 by Richards *et al.* [60], Johnson *et al.* [61] and in 1992 by Keevil *et al.* [62] but suffered of several problems due to technological limits.

In the following sections, will be illustrated the methods, the laboratory experiments and the clinical scanners acquisitions, afterward discussed within the framework of data validation and harmonization.

3.2 THE BELT PHANTOM

The purpose of the *'belt phantom'* is to provide a wide range of reference values for both T_1 and T_2. Other useful characteristics are the stability and the homogeneity. It was then decided to create a phantom based on manganese aqueous solutions, being Mn(II) aqua ion a compound with such properties well known in the literature [63, 64].

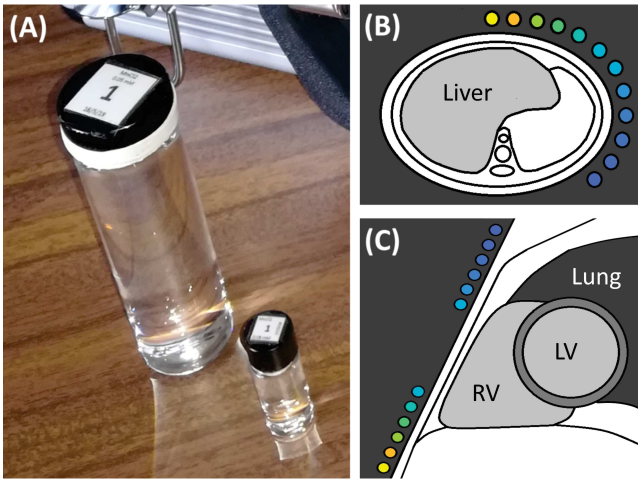

Figure 25: The 30 ml and 2 ml vials containing the $MnCl_2$ aqueous solutions, used as reference samples (A). Suggested accommodation of the 30 ml vials in a cartridge-like belt configuration around a sketched liver (B). Suggested accommodation of the 2 ml vials in a cartridge-like belt configuration nearby a sketched heart (RV = Right Ventricle, LV = Left Ventricle) (C).

3.2.1 Preparation

The reference samples composing the belt phantom consist of twelve 30 ml vials made of borosilicate glass with PTFE teflon caps (supplied by Fischer Scientific, Loughborough, UK) filled with different concentrations of manganese(II) chloride tetrahydrate (formula $MnCl_2 + 4\,H_2O$, molar mass 197.91 g/mol; supplied by Sigma-Aldrich Co., St. Louis, MO, USA) in aqueous solutions, using MilliQ water as solvent. Through the serial dilution technique, twelve different concentrations ranging from 0.05 mM to 0.45 mM were prepared, with a precision of ±2%.

For future *in vivo* applications, each vial can be separately placed side by side into a non-rigid thermo-isolating cartridge-like belt designed for the simultaneous acquisition of both the samples and the patient (Fig. 25). When properly positioned, the samples will appear on the image as a series of circles (the axial slices of the vials) on the surface of the patient (see Fig. 25.B). Twelve smaller vials (2 ml) made of the same materials and filled with solutions identical to the 30 ml ones were also prepared for the NMR measurements. These vials can also substitute the bigger vials as a reference for the mapping of smaller volumes (Fig. 25.C).

3.2.2 NMR Characterization

The reference T_1 and T_2 values of the solutions at $B_0 = \mu_0 H = 1.5$ T were measured with an NMR spectrometer (Tecmag Apollo, Houston, TX, USA) equipped with an electromagnet (Bruker, Billerica, MA, USA) by scanning the 2 ml vials (see Fig. 26). The temperature dependence of the relaxation time values was measured at five different temperatures ranging from 17°C to 29°C with steps of 3°C, by placing each vial inside a cryostat in which the temperature could be set by balancing a flux of liquid nitrogen and a heating resistance. The temperature was measured with a thermocouple close to the vial with a precision of ±0.2°C. The temperature range was chosen accordingly to the usual room temperature of the MRI scanners, taking also into account the possible presence of the patient as a heating source inside the bore.

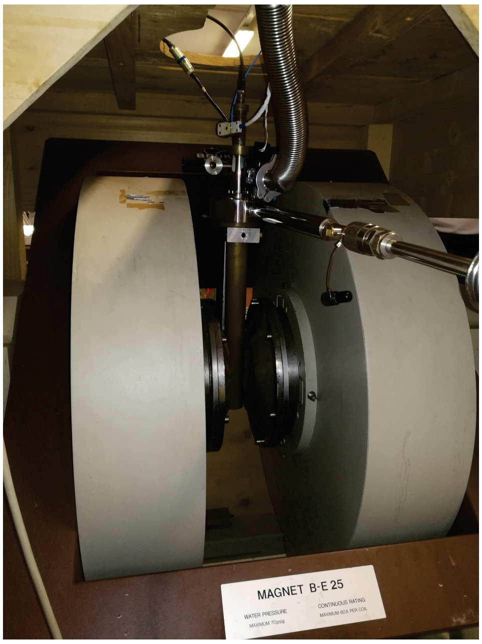

Figure 26: NMR experimental set up: the nitrogen-flux cryostat placed between the Bruker electromagnet expansions.

Standard NMR pulse sequences were used to obtain the reference ground-truth relaxation time values (see Section 2.1):

- *IR sequence* with a SE readout, for T_1 measurements (acquisition parameters: $\pi/2$ pulse duration = 5.5 μs, echo time = 4 ms, repetition time = 10 s);

- *SR sequence* with a SE readout, for T_1 measurements (acquisition parameters: $\pi/2$ pulse duration = 5.5 μs, echo time = 4 ms, repetition time = 10 s);
- *CPMG sequence* for T_2 measurements (acquisition parameters: $\pi/2$ pulse duration = 5.5 μs, τ = 50 μs, repetition time = 5 s).

IR and SR data were then fitted with an exponential recovery function $y = A(1 - B\exp(-t/T_1))$, while CPMG data were fitted with an exponential decay function $y = A\exp(-t/T_2) + B$. A, B, T_1 and T_2 were used as adjustable parameters for the fitting.

THEORY RECALLS As already illustrated in Section 2.3 and here reported for sake of clarity, the Solomon-Bloembergen-Morgan (SBM) theory [17, 19] for paramagnetic dilute solutions explains how the relaxation times of diamagnetic host solution (usually pure water, as in the case of this study) can be changed by adding a paramagnetic species according to the equation:

$$R_{i,obs} = R_{i,dia} + r_i\,C \quad \text{with } i = 1, 2 \tag{47}$$

where R_i are the overall observed relaxation rates ($R_{i,obs} = 1/T_{i,obs}$, $i = 1, 2$), $R_{i,dia}$ are the relaxation rates of the diamagnetic host solution, r_i are the nuclear relaxivities (in units of $\mathrm{mM}^{-1}\ \mathrm{s}^{-1}$) that measure the efficiency of the paramagnetic species in increasing the relaxation rates and, therefore, the MRI image contrast, and C is the concentration of the paramagnetic species in the solution (usually expressed in mM).

The SBM theory also describes the temperature dependence of the relaxation times (see also the pioneering work by Bloembergen-Purcell-Pound [16]) for aqueous paramagnetic dilute solutions, although Bernheim *et al.* in 1959 already performed a preliminary study [65]. The model describes the nuclear relaxation mechanism as due to the dipolar spin-spin interaction and to the scalar coupling (or contact interaction) between the nuclear spin and the electron spin, modulated respectively by the correlation times τ_{ci} and τ_{ei}, as described in Section 2.3. Bernheim *et al.* assume an Arrhenius-type exponential dependence with the temperature T of the dipolar correlation time τ_c

$$\tau_c = \tau_c^0 \exp(V_c/RT) \tag{48}$$

where V_c is the activation energy for the molecular motion (R is the molar gas constant), and a hybrid dependence (linear and Arrhenius-type exponential) with the temperature of the exchange correlation time τ_e

$$\frac{1}{\tau_e} = \frac{\exp(-V_m/RT)}{\tau_m^0} + \frac{T_0}{\tau_s^0(T - T_0)} \tag{49}$$

where V_m is the activation energy for the exchange mechanisms.

In the range of temperatures explored in this study (five temperatures within a range of 15°C nearby the room temperature), the model predicts a linear dependence of relaxation times with temperature, which was thus assumed for our data analysis [60].

RESULTS

The dependence of relaxation rates with $MnCl_2$ concentration at five different temperatures, as obtained from NMR measurements, are shown in Fig. 27. Based on previous studies on the *a priori* error of the NMR experimental setup, an experimental error of ±5% was applied to all relaxation times values. The theoretical expected linear behavior as a function of the paramagnetic species concentration was experimentally confirmed for both R_1 and R_2 results at all temperatures ($R^2 > 0.99$). The expected linearity of relaxation times as a function of temperature was also found for all the vials ($R^2 > 0.99$).

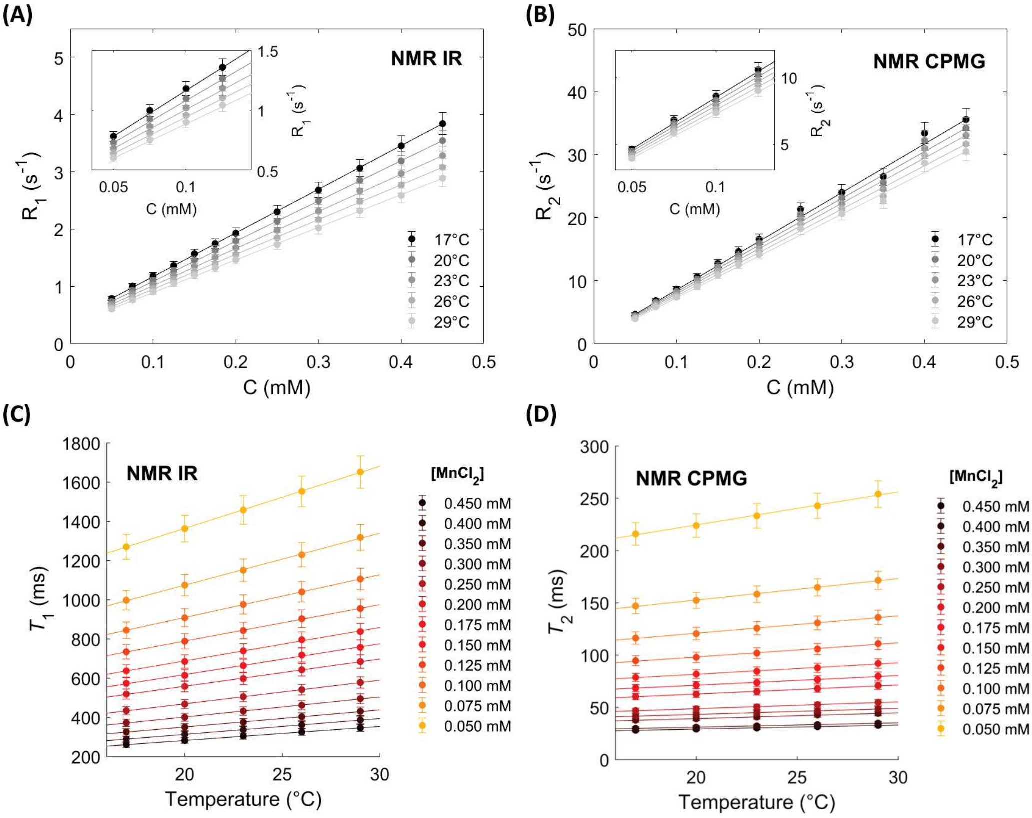

Figure 27: *Top Graphs*: (A) Longitudinal R_1 (s^{-1}) and (B) transverse R_2 (s^{-1}) relaxation rates as a function of $MnCl_2$ concentration C (mM) at different temperatures, as obtained from NMR measurements using IR and CPMG sequences. The insets report a magnification of relaxation rate data at low $MnCl_2$ concentrations.
Bottom Graphs: (C) Longitudinal T_1 (ms) and (D) transverse T_2 (ms) relaxation times as a function of temperature for all the $MnCl_2$ concentrations, as obtained from NMR measurements using IR and CPMG sequences.

SR results were found to be statistically coincident with the IR ones within the experimental error of 5% (see the Bland-Altman analysis [66, 67] in Fig. 28): only IR results were then used as the T_1 ground-truth reference values.

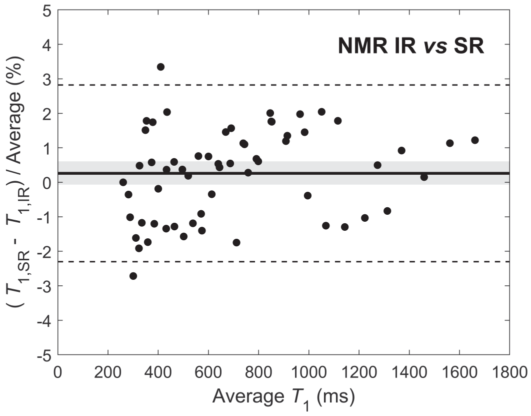

Figure 28: Bland-Altman plots of the comparison between the results concerning the relaxation time T_1 as measured with the NMR IR and the NMR SR sequences. The shaded area represent the confidence level limits, while dotted lines are the limits of agreement for the mean value (bold line). Kolmogorov-Smirnov test p-value = 0.5309; mean = 0.26%; standard deviation = 1.31%; limits of agreement = [−2.30%, +2.82%].

3.3 MRI MAPPING EXPERIMENTS

Three main experiments were conducted: the first one consisted in a general application of the method to several acquisition sequences employing two different MRI scanners (a General Electric Signa and a Siemens Magnetom Aera); the second one was more focused on the sequences developed for cardiac applications (MOLLI and T_2-prep TrueFISP, available on the Siemens scanner only); the third experiment tested the method *in vivo* on an untrained volunteer.

3.3.1 Image Processing

Four different software were used for the image post-processing and relaxation time map measurements: (i) *Segment* [68, 69], a vendor-independent and open-source software (http://www.medviso.com); (ii) *swSD*, a custom Matlab (MathWorks, Natick, MA, USA) script; (iii) *Siemens VE11C MyoMaps* [70], the vendor software installed on the Siemens Magnetom Aera (only for MOLLI and T_2-prep TrueFISP images); and (iv) *ImageJ* (only for the measurements of the maps obtained from the Siemens software, http://imagej.net).

All the DICOM images acquired with the clinical scanners were post-processed employing both Segment and swSD. The images acquired using MOLLI and T_2-prep TrueFISP sequences were also post-processed with the Siemens software: this software generates the relaxation time maps after the application of a motion correction algorithm.
Segment and swSD were used for the measurements of the self-generated maps by means of built-in tools, while the ImageJ Measure Tool was used for the measurements of the maps generated by the Siemens software.

Through the swSD software, the SD maps (pixel-wise 68% confidence bound, in absolute value, for the fitted relaxation time) were calculated for each selected ROI on the relaxation time maps in order to provide an alternative estimation of the standard deviations for the average values measured on the relaxation time maps themselves: this procedure allows to retrieve the errors arising from the fitting which is a piece of information completely lost if considering only the relaxation time maps (*e.g.* in an homogeneous region of a relaxation time map a value of $T_{1,average} \pm \sigma$ can be measured, with σ given by the distribution of the values in the pixels of the region, but each of those values may be the result of a fitting with uncertainty σ_{fit} which is different, generally speaking, with respect to σ).

THE SWSD SOFTWARE Here below we illustrate the steps for the relaxation time and SD maps generation starting from the acquired images, taken as input, performed by the swSD software.

Pixel-wise T_1 or T_2 estimates were initialized using a preliminary search of T_1 or T_2 values chosen in discrete ranges (from 50 to 4000 ms with steps of 10 ms for T_1; from 5 to 600 ms with steps of 1 ms for T_2) so to minimize the residuals between, respectively, the normalized $y = |A_1(1 - B_1 \exp(-t/T_1))|$ (hence with $A_1 = 1$) or the normalized $y = A_2 \exp(-t/T_2) + B_2$ (hence with $A_2 = 1$ and $B_2 = 0$) with the normalized acquired data. For the T_1 initialization, also the factor B_1 is preliminary searched in a range from 1.5 to 2.5 with steps of 0.1. The final T_1 or T_2 maps were then obtained with the pre-implemented Matlab `fminsearch` method giving as input the acquired raw data and using the 3-parameters equation $y = |A_1(1 - B_1 \exp(-t/T_1))|$ (for T_1) or the 3-parameters $y = A_2 \exp(-t/T_2) + B_2$ (for T_2). To obtain T_1 maps from MOLLI acquisitions, the Look-Locker correction Eq. 37 was applied. For T_2-prep TrueFISP images, $B_2 = 0$ was imposed since each acquisition is composed of only three images (*i.e.* three different $T_{E,prep}$s, see below).

A circular ROI was used for the calculation of the average relaxation time on the map (Matlab `mean` method).

The SD maps were extracted only for the pixels selected on the maps by the circular ROI used for the measurements of T_1 and T_2: to those pixels, through the pre-implemented Matlab `fit` method, and using the parameters obtained from the previous step using `fminsearch` as starting points, was calculated the 68% confidence bound, in absolute value, for the fitted relaxation time. To the average value of T_1 or T_2 calculated in the circular ROI on the relaxation time map was then assigned as standard deviation the average value measured on the SD map.

A example of the swSD interface is shown in Fig. 29.

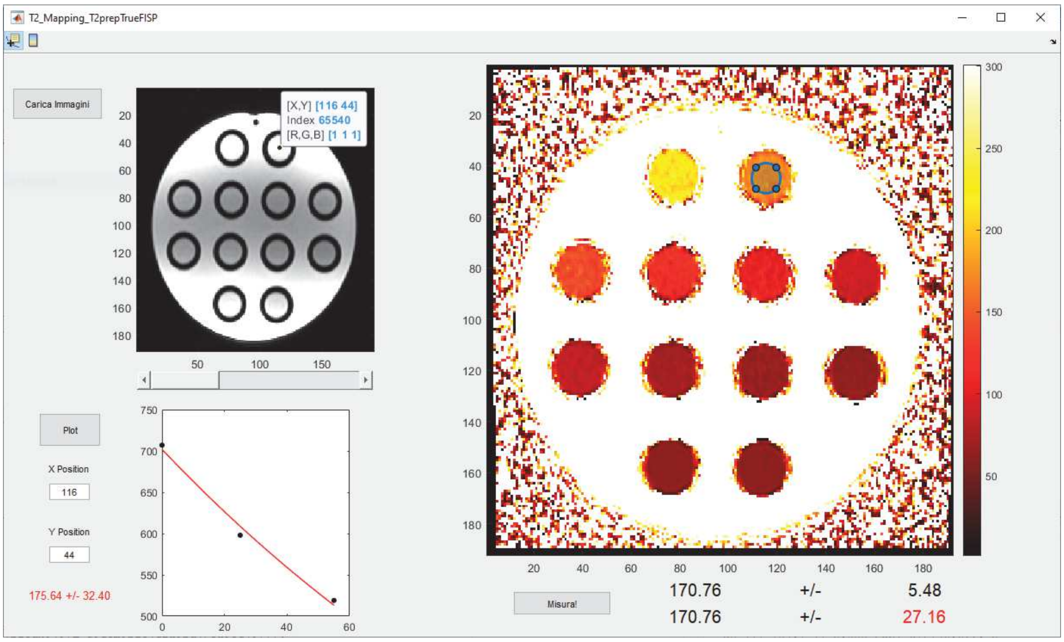

[X,Y] [116 44]
Index 65540
[R,G,B] [1 1 1]

X Position: 116

Y Position: 44

175.64 +/- 32.40

170.76 +/- 5.48

170.76 +/- 27.16

Figure 29: Interface of the custom Matlab software *swSD*. In the image can be seen the image explorer navigator by means of a slider (top left), the fit for the pixel in the position (X,Y) (bottom left) and the generated relaxation time map (right). Below the map, a button allows to measure the usual average ± standard deviation of the pixels in the blue circular ROI on the map (top row) and the average ± average of the SD map (this latter indicated in red) as explained in the text (bottom row).

3.3.2 Exp. 1: Different Scanners, Different Sequences

Relaxation time maps of the samples composing the belt phantom were acquired employing different acquisition sequences of use in clinical applications.

In Fig. 30, the vials arrangement in a plexiglas support filled with doped water (to increase the SNR) and the temperature monitoring system employed are shown: an optical fiber sensor TempSense (Opsense Inc., Quebec, Canada), with a sensitivity of ±0.2°C.

The MRI acquisitions were performed using two different clinical MRI scanners (see Fig. 31):

- a *Siemens Magnetom Aera*: $B_0 = 1.5$ T, bore size 70 cm, gradient strength 33 mT m^{-1} @ gradient slew rate 125 T m^{-1} s^{-1} and 45 mT m^{-1} @ gradient slew rate 200 T m^{-1} s^{-1} (Siemens Healthineers, Erlangen, Germany);
- a *General Electric Signa*: $B_0 = 1.5$ T, bore size 60 cm, gradient strength 33 mT m^{-1} @ gradient slew rate 120 T m^{-1} s^{-1} (General Electric Healthcare, Chicago, IL, USA).

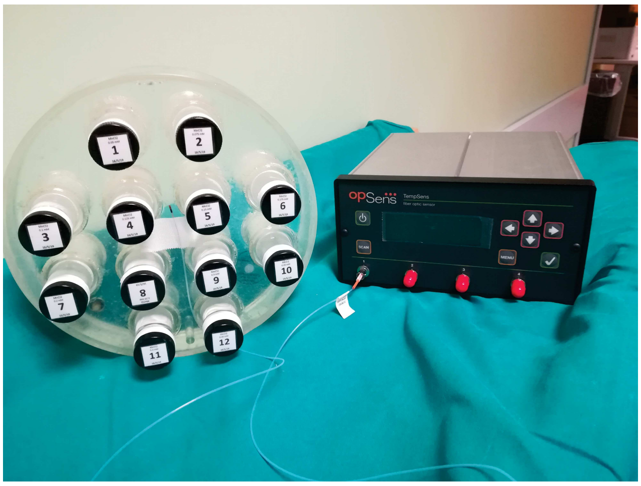

Figure 30: The twelve 30 ml $MnCl_2$ vials arranged in a plexiglass support (filled with doped water for increasing the SNR) and the optical fiber sensor TempSense.

Figure 31: The 1.5 T MRI scanners used in this study: a Siemens Magnetom Aera (left) and a GE Signa (right).

Three different types of sequences were used:

- standard clinical sequences, IR and SE;
- fast (turbo) clinical sequences, IR-TSE and TSE;
- fast sequences developed for cardiac applications, MOLLI (5-3 acquisition scheme [33]) and T_2-prep TrueFISP.

It is important to remark that the third type of sequences was executed only with the Siemens MRI scanner. The acquisition parameters used can be found in Table 2.

Table 2: MRI acquisition parameters of Exp. 1.

MRI Scanner	**GE Signa (1.5 T)**				**Siemens Aera (1.5 T)**					
Parameters	**IR**	**SE**	**IR-TSE**	**TSE**	**IR**	**SE**	**IR-TSE**	**TSE**	**MOLLI**	**T_2-prep TrueFISP**
Coil Type	Quadrature Birdcage (Head)				Body Wrap Around (Body)					
FOV (mm × mm)	250 × 250	250 × 250	250 × 250	250 × 250	250 × 250	250 × 250	250 × 250	250 × 250	272 × 272	223 × 223
Matrix	256 × 256	256 × 256	512 × 512	256 × 256	256 × 256	256 × 256	256 × 256	256 × 256	256 × 256	192 × 192
ST (mm)	5	5	5	5	5	5	5	5	8	8
FA (°)	90	90	90	90	90	90	90	90	35	70
T_R (ms)	5000	5000	10000	5000	5000	5000	10000	5000	414.35	323.03
T_E (ms)	15	15, 25, 35, 50, 60, 70 80, 100, 200, 300	12	12.5, 25, 37.6, 50.1, 62.6, 75.1, 87.6, 100.2, 200.3, 300.5	15	15, 25, 35, 50, 60, 70, 80, 100, 200, 300	11	15, 30, 44, 59, 74, 89, 104, 133, 207, 311	1.28	1.3
$T_{E,prep}$ (ms)	-	-	-	-	-	-	-	-	-	0, 25, 55
T_I (ms)	40, 70, 120, 210, 350, 600, 1050, 1750, 2940, 4000	-	50, 70, 120, 210, 350, 600, 1050, 1750, 2940, 4000	-	40, 70, 120, 210, 350, 600, 1050, 1750, 2940, 4880	-	40, 70, 120, 210, 350, 600, 1050, 1750, 2940, 4620	-	156, 236, 1156, 1236, 2156, 2236, 3156, 4156	-
ETL	1	1	16	24	1	1	9	21	1	1
NA	1	1	1	1	1	1	1	1	1	1
PS (%)	100	100	50	100	100	100	100	100	63.7	74.8
PB (Hz/pixel)	651	122	65	115	130	130	150	95	1085	1185
HR (bpm)	-	-	-	-	-	-	-	-	60	60
T (°C)	22.8	23.7	23.7	23.7	23.5	24.1	22.8	22.5	25.0	25.0

FOV = Field Of View; *ST* = Slice Thickness; *FA* = Flip Angle; T_R = Repetition Time; T_E = Echo Time; $T_{E,prep}$ = T_2 Preparation Time; T_I = Inversion Time; *ETL* = Echo Train Length; *NA* = Number of Averages; *PS* = Percent Sampling;*PB* = Pixel Bandwidth; *HR* = Heart-Rate; *T* = Temperature.

RESULTS

The comparisons between MRI results and NMR reference values are illustrated in Figs. 32 to 34: in the graphs, the longitudinal R_1 (s^{-1}) and transverse R_2 (s^{-1}) relaxation rates as function of $MnCl_2$ concentration C (mM) are reported. The data points with error bars correspond to the MRI results of the samples' relaxation times, while the grey areas represent the NMR reference values. The values reported are those obtained by the custom swSD Matlab script. The coefficients of determination R^2 of data (R_i *vs* [$MnCl_2$]), assuming a linear regression model as predicted by the SBM theory, were greater than 0.997 for all data-sets with the only exception of T_2-prep TrueFISP ones. To obtain the NMR reference values for the MRI results, which were acquired at different temperatures with respect to the NMR measurements, the linear regression of NMR data *vs* temperature was used: for all the concentrations (*i.e.* all the vials) both relaxation times showed a linear behavior as a function of the temperature, with coefficients of determination $R^2 > 0.99$. Using the slope and intercept parameters obtained from the linear regressions of the data (relaxation times *vs* temperature), it was possible to determine the relaxation times reference values of each vial at all temperatures, which are measured during each MRI scan by means of the optical fiber sensor. The gray areas were then obtained

applying to the regression lines of relaxation rates *vs* $MnCl_2$ concentration at a given temperature a percentage error of ±5% (see Section 3.2.2).
Fig. 35 shows the dependence of the errors (expressed as percentage values) obtained through the swSD software by measuring the mean values on the SD maps related to the relaxation time maps in corresponding ROIs, for each used sequence. From swSD software analysis, it was decided to set conservatively the experimental errors as follows: ±5% for relaxation times measured on maps obtained from IR, IR-TSE, and SE acquisitions and ±10% for T_2s measured on maps obtained from TSE acquisitions; the average values measured on the SD maps for relaxation times measured on MOLLI and T_2-prep TrueFISP maps.
Compatibility tests between MRI values measured on maps from standard and turbo sequences and the NMR reference values were performed employing the two-sample t-test, assuming the experimental errors equal to the standard deviations. As null hypothesis was assumed the equality of the relaxation times mean values measured with NMR techniques, on one side, and on the parametric maps, on the other side. In all cases, a significance level (p-value) greater than 0.1 was obtained. A significative discrepancy (p-value < 0.1) was found for MOLLI (underestimation, for [MnCl2] > 0.2 mM) and T_2-prep TrueFISP (overestimation, for [MnCl2] > 0.1 mM) values from NMR reference ones.

Considering standard and their turbo-analogous sequences, a good agreement (p-values > 0.1) was found for both MRI scanners and for both relaxation times of each vial in the limits of the experimental errors found with the swSD software: ±5% for both T_1 and T_2 using standard IR, SE and IR-TSE clinical sequences, ±10% for TSE clinical sequences. Such accordance with NMR values was expected since proper acquisition parameters were chosen and no issues in the acquisition steps were reported. Nevertheless, the use of reference samples even for standard and their turbo analogous sequence should be encouraged, especially for purpose in which an high accuracy/precision is required.
The discrepancies found for MOLLI and T_2-prep TrueFISP sequences from NMR reference values (p-values < 0.1), well known in the literature [9, 10, 12–14, 71], could be overcome by recalibrating the maps [62]: a sequence-scanner-software dependent recalibration, generally not straightforward, can be applied as long as a simultaneous scan of both the patient and the samples is performed, as it was done for CT images [46, 47]. The recalibration can be performed by plotting the measured relaxation times against the true ones of the vials solutions and finding the best bijective fitting function (either linear, as in the case of MOLLI results, or non-linear, as in the case of T_2-prep TrueFISP results) that links the two sets of values and applying that function to the acquired relaxation times maps [62].

Since a recalibration of the acquired map is a delicate procedure that involves error propagation, a proper evaluation of the errors must be performed: the analysis with the swSD software had this purpose. In fact, the error of a measured relaxation time is not only dependent on the homogeneity of the ROI of the map in which is calculated, but also on the previous processing: in this study, only the fit was taken into consideration, but many other factors can be accounted in the SD map analysis (like static magnetic field B_0 and radio-frequency field B_1 inhomogeneities and instabilities, Gibbs's ringing artifacts, etc.).

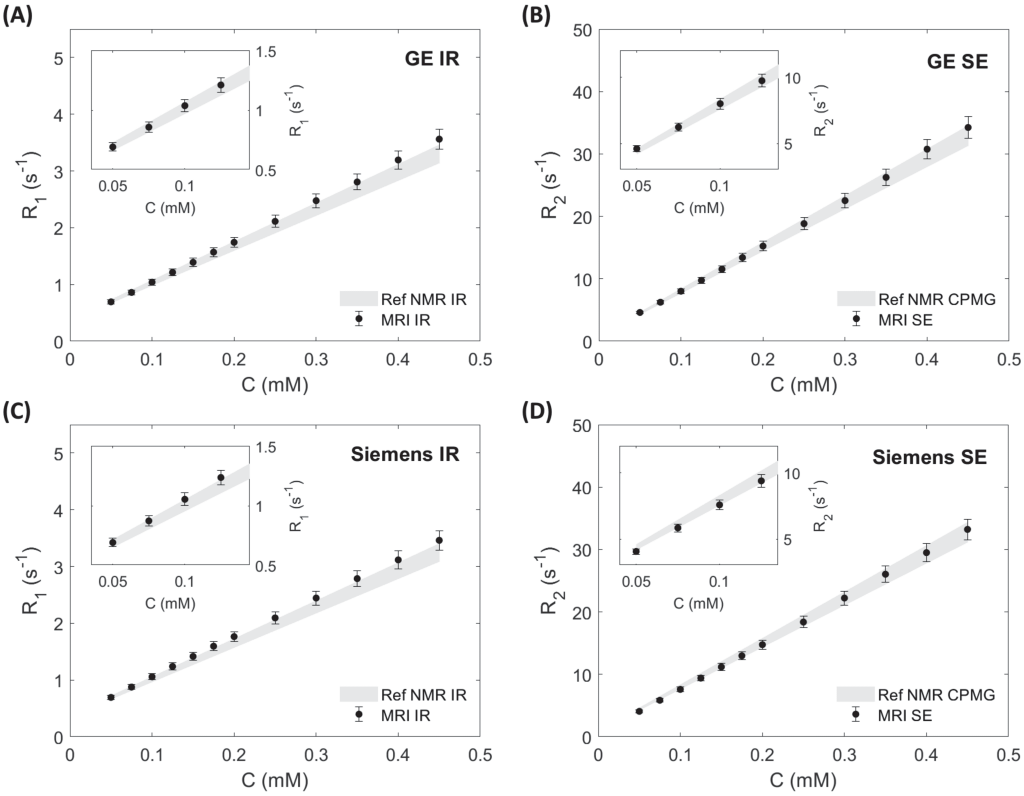

Figure 32: MRI results *vs* NMR reference relaxation times values (grey areas) measured by means of standard sequences IR (A and C) and SE (B and D) obtained with the GE (A and B) and with the Siemens (C and D) MRI scanner. The insets in the graphs represent a magnification of the data at low $MnCl_2$ concentrations. $MnCl_2$ samples temperature as measured with the optical fiber sensor: GE IR at 22.8°C; Siemens IR at 23.5°C; GE SE at 23.7°C; Siemens SE at 24.1°C.

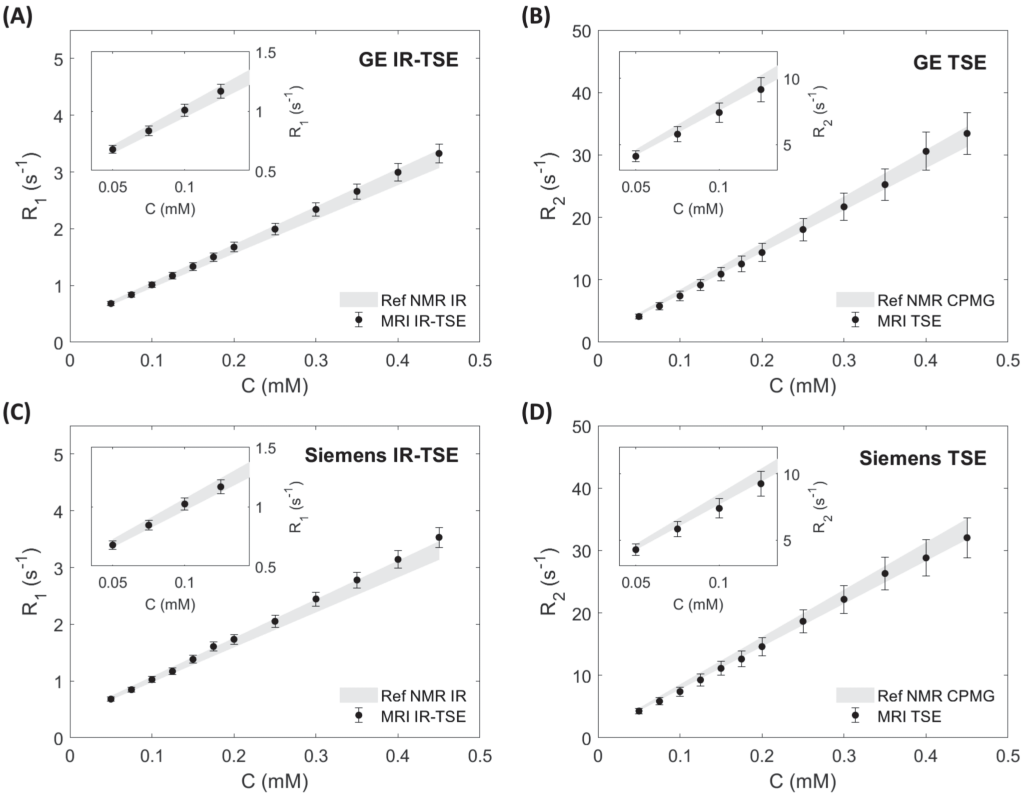

Figure 33: MRI results *vs* NMR reference relaxation times values (grey areas) measured by means of IR-TSE (A and C) and TSE (B and D) sequences, obtained with the GE (A and B) and with the Siemens (C and D) MRI scanner. The insets in the graphs represent a magnification of the data at low $MnCl_2$ concentrations. $MnCl_2$ samples temperature as measured with the optical fiber sensor: GE IR-TSE at 23.7°C; Siemens IR-TSE at 22.8°C; GE TSE at 23.7°C; Siemens TSE at 22.5°C.

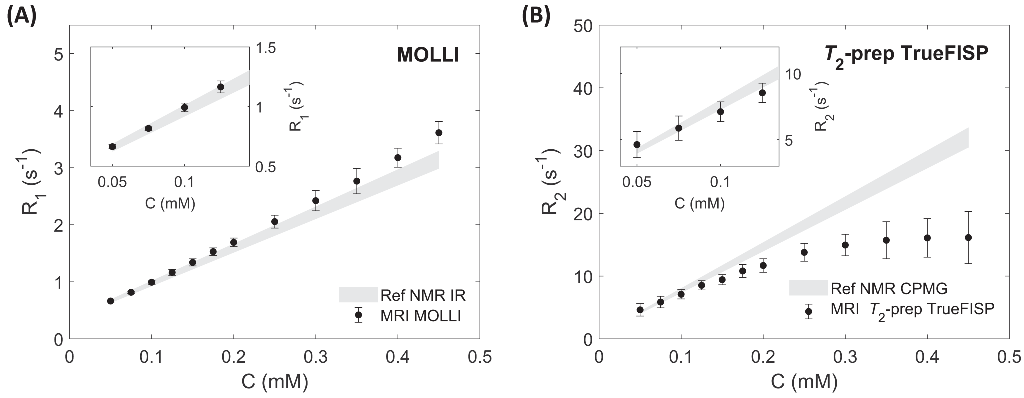

Figure 34: MRI results *vs* NMR reference relaxation times values (grey areas) measured by means of MOLLI (A) and T_2-prep TrueFISP (B) sequences, obtained with the Siemens MRI scanner and with a simulated heart-rate of 60 bpm. $MnCl_2$ samples temperature as measured with the optical fiber sensor: MOLLI at 25°C; T_2-prep TrueFISP at 25°C.

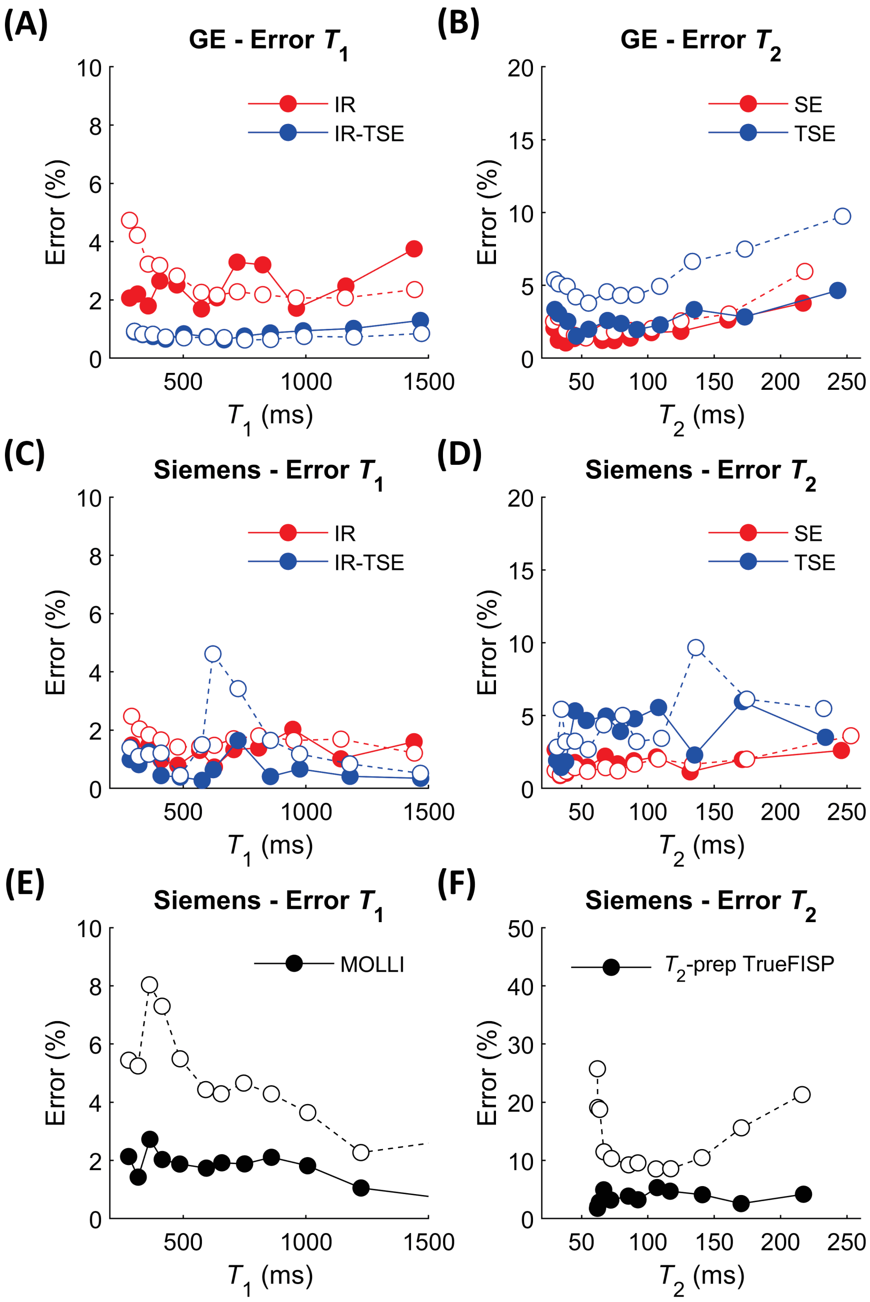

Figure 35: SwSD software measurements of SD maps related to the relaxation times maps acquired through standard, turbo and cardiac mapping sequences with the GE (top row: A and B) and the Siemens (central and bottom rows: C, D, E, and F) MRI scanner. In the graphs the percentage errors measured with the swSD software as a function of the mean relaxation times calculated on the relaxation time maps in circular ROIs, for each used sequence, are illustrated. The filled dots connected by continuous lines represent the percentage errors usually calculated (*i.e.* obtained from the standard deviations of the relaxation times in a selected ROI of the relaxation time maps), while empty dots connected by dashed lines are those retrieved from the SD maps (*i.e.* the average value of the 68% confidence bound of the fitted relaxation times in the ROI selected on the relaxation time maps, see text).

3.3.3 Exp. 2: Phantom Study of Cardiac Mapping Sequences

In this second experiment we applied our method in a phantom study. We acquired MOLLI and T_2-prep TrueFISP maps with the Siemens Aera MRI scanner of an Eurospin phantom (Diagnostic Sonar Ltd, Livingston, Scotland [72]), which played the role of the patient. The belt phantom was wrapped around the Eurospin phantom as illustrated in Fig. 36.

Figure 36: Acquisition set-up employed in the second experiment.

Table 3: MRI acquisition parameters of Exp. 2.

Parameters	**MOLLI**	**T_2-prep TrueFISP**
Coil Type	Body Wrap Around (Body)	
FOV (mm × mm)	360 × 242	391 × 257
Matrix	256 × 172	192 × 126
ST (mm)	8	8
FA (°)	35	70
T_R (ms)	286.96	207.95
T_E (ms)	1.12	1.04
$T_{E,prep}$ (ms)	-	0, 25, 55
T_I (ms)	HR dependent (8)	-
ETL	1	1
NA	1	1
PS (%)	66.7	74.7
PB (Hz/pixel)	1085	1185
HR (bpm)	30 – 150 (15)	30 – 150 (15)
T (°C)	22.5	22.5

FOV = Field Of View; *ST* = Slice Thickness; *FA* = Flip Angle; T_R = Repetition Time; T_E = Echo Time; $T_{E,prep}$ = T_2 Preparation Time; T_I = Inversion Time; *ETL* = Echo Train Length; *NA* = Number of Averages; *PS* = Percent Sampling; *PB* = Pixel Bandwidth; *HR* = Heart-Rate; *T* = Temperature.

We selected 12 over the 18 available vials of the Eurospin phantom for this study (ID = 2, 4, 5, 6, 7, 9, 10, 11, 13, 15, 16, 17). These vials are filled with

agarose gels doped with gadolinium in different compositions. They are usually employed for Quality Assurance (QA) tests of the scanner contrast efficiency.
The acquisition parameters are summarized in Table 3. Since MOLLI and T_2-prep TrueFISP sequences work with the ECG-triggering and, therefore, their acquisition parameters depend on the heart-rate (HR) of the scanned patient (see Section 2.2.3), we simulated different heart-rates ranging from 30 bpm to 150 bpm (15 in total).

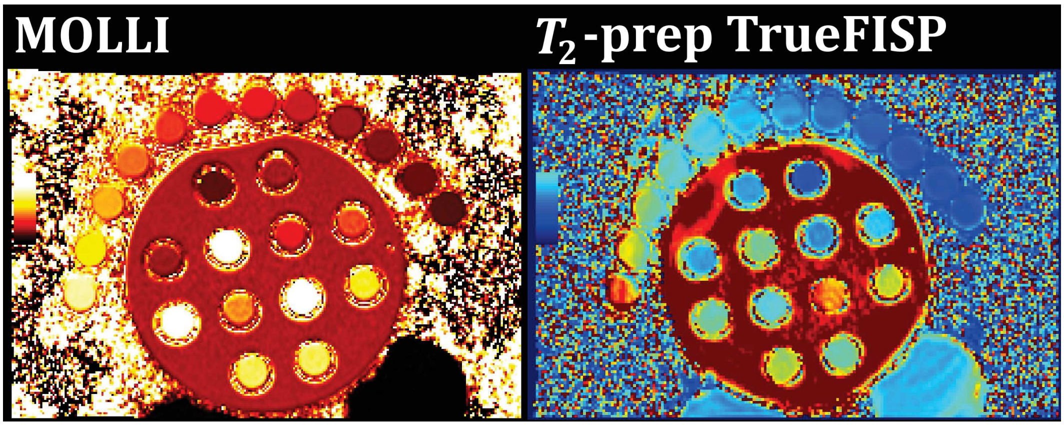

Figure 37: Example of MOLLI and T_2-prep TrueFISP maps of the belt phantom wrapped around the Eurospin phantom, as illustrated in Fig. 36, acquired during Exp. 2.

RESULTS

In Fig. 37, as example, the T_1 and T_2 maps of the phantoms at 60 bpm are reported. As a first observation, the MOLLI map appear to be more homogeneous and with less artifacts with respect to T_2-prep TrueFISP one: this characteristic was observed in all the acquired maps at each simulated heartbeat.

Belt Phantom - Considering T_1 and T_2 values of the belt phantom as measured on the maps obtained through MOLLI and T_2-prep TrueFISP sequences, we found the same behavior observed in the first experiment (see Fig. 38): from compatibility two-sample t-tests and using as standard deviations the values obtained with swSD, a significant discrepancy (p-values < 0.1) was found for MOLLI (underestimation, for $[MnCl_2] > 0.2$ mM) and T_2-prep TrueFISP (overestimation, for $[MnCl_2] > 0.1$ mM) values from NMR reference ones (null hypothesis: NMR values = parametric maps values).
The dependence of the relaxation times and of their errors calculated with the swSD software from the simulated heart-rate is shown in Fig. 39: MOLLI results are slightly dependent on the simulated heart-rate [73, 74], and,

even though an underestimation of T_1 occurs, the linear behavior of R_1 against $MnCl_2$ concentration is maintained (all $R^2 > 0.999$); T_2-prep TrueFISP results lost the linear trend predicted by the theory and are more sensitive to the heart-rate variation.

It is also important to underline that the errors reported in Fig. 39, *i.e.* the

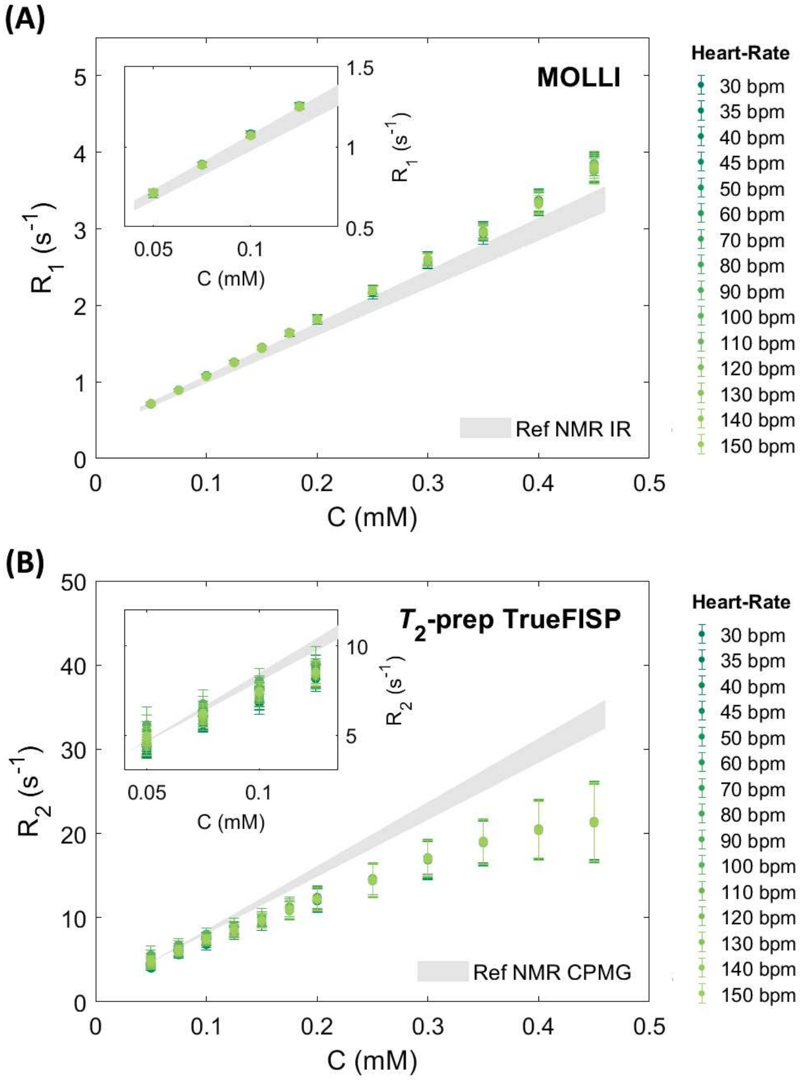

Figure 38: MRI longitudinal R_1 (s^{-1}) and transverse R_2 (s^{-1}) relaxation rates results as a function of the $MnCl_2$ concentration C (mM), for each simulated heart-rate (bpm), vs NMR reference values (grey areas) for MOLLI (A) and T_2-prep TrueFISP (B) sequence acquisitions obtained with the Siemens MRI scanner. The coefficients of determination R^2 of MOLLI results, assuming a linear regression model as predicted by the SBM theory, were 0.999 for all data-sets. The insets in the graphs represent a magnification of the data at low $MnCl_2$ concentrations. Belt phantom temperature as measured with the optical fiber sensor: MOLLI at 22.5°C; T_2-prep TrueFISP at 22.5°C.

errors derived from the fitting procedure and highlighted with the swSD software analysis, are systematically greater than the errors measured from the usual evaluations performed by Segment and ImageJ, as already pointed out in the previous experiment (see Fig. 35). The errors measured with Segment and ImageJ were lower than 3% for both type of sequences, except for the errors related to the four highest T_2s, with a maximum error of 8% (due to some artifacts affecting the images because of some unsolved field inhomogeneities): these errors turn to be lower than those estimated with swSD for every measurement.

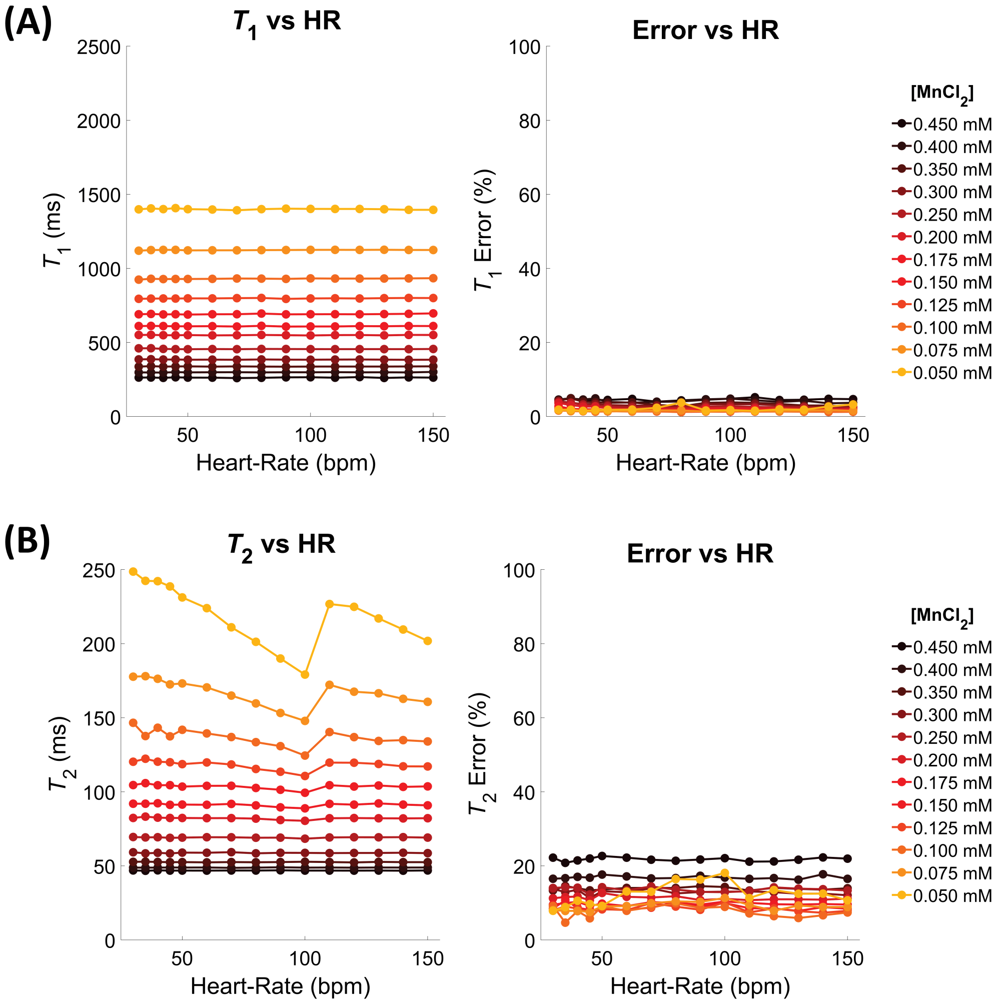

Figure 39: Belt phantom: Dependence from the simulated heart-rates (bpm), for each concentration, of the relaxation times T_1 and T_2 (left) and relative percentage errors (right) measured on, respectively, MOLLI (A) and T_2-prep TrueFISP (B) maps obtained through the swSD software.

Eurospin Phantom - Fig. 40 illustrates the dependence with the heart-rate of the Eurospin's vials relaxation times and of their percentage errors as

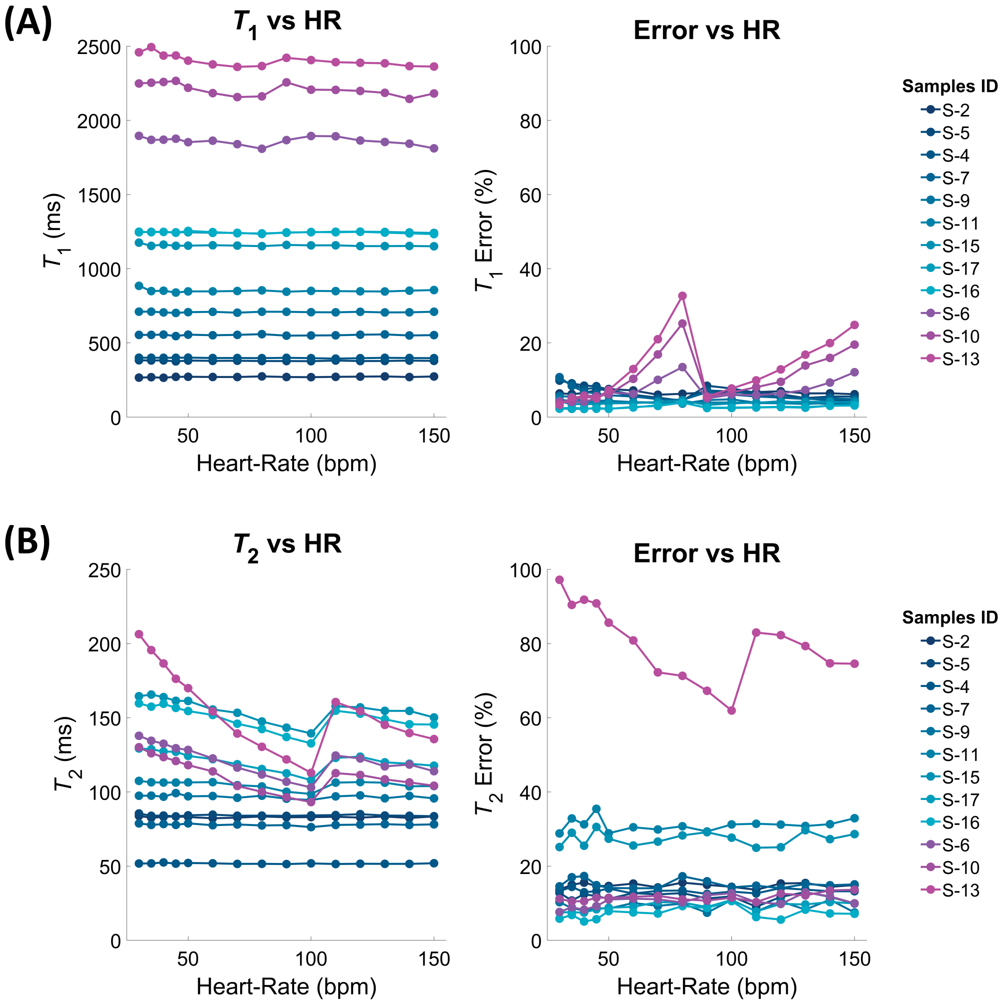

Figure 40: Eurospin phantom: Dependence from the simulated heart-rates (bpm), for each concentration, of the measured relaxation times T_1 and T_2 (left) and relative percentage errors (right) measured on, respectively, MOLLI (A) and T_2-prep TrueFISP (B) maps obtained through the swSD software.

measured by means of the swSD software. As for the case of $MnCl_2$ samples of the belt phantom, we could see a more pronounced dependence from the heart-rate of T_2 values over T_1 ones. The swSD software analysis allowed to quantify the error attributed to the fitting procedure that in same cases reached value around 40% for T_1 and 100% for T_2, while the usual errors (*i.e.* standard deviations of the relaxation times in a selected ROI on the maps) were smaller than 3% for T_1 and 5% for T_2. Moreover, the dependence from the heart-rate of Eurospin's vials T_2 values questioned the feasibility of a recalibration strategy for the T_2-prep TrueFISP maps since the curves overlapped, differently from the case of belt phantom, not preserving the relations between the true relaxation times of the Eurospin's vials. This could led to mis-corrections of the values. The overlapping seems to occur in samples with long T_1 values ($\gtrsim$ 2000 ms), which in the human body can be found only for the cerebrospinal fluid (CSF, similar to pure water: $T_1 \sim 3$ s and $T_2 \sim 2$ s).

RECALIBRATION

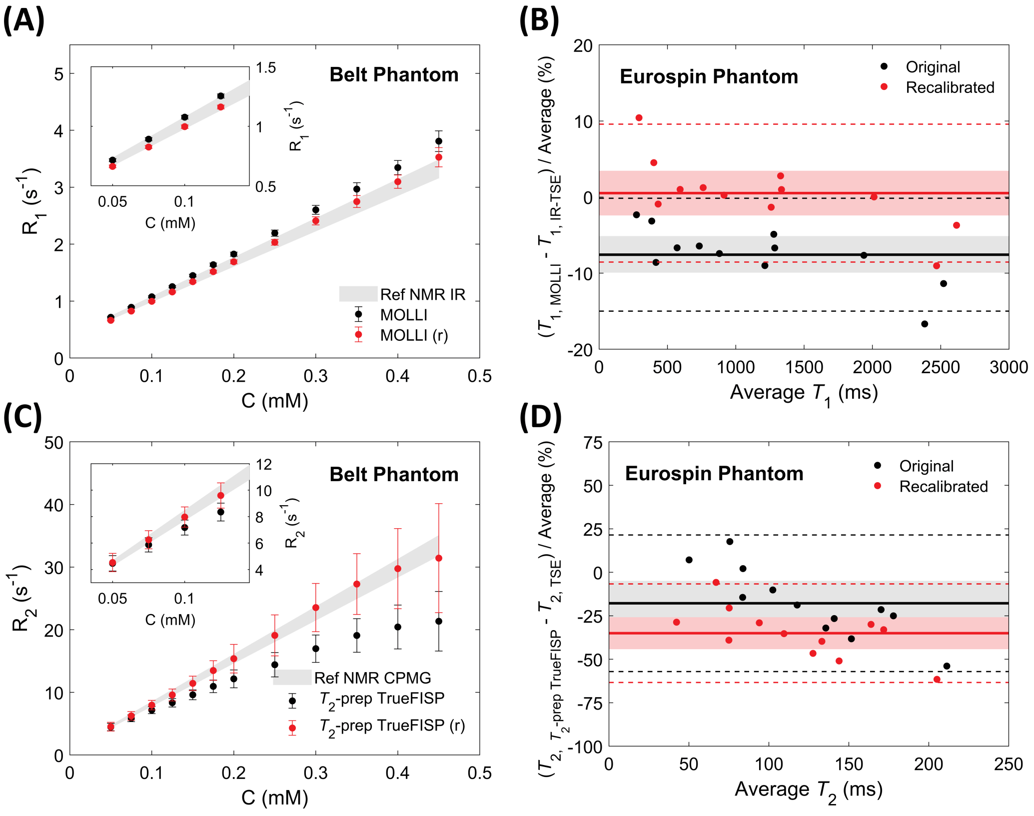

Figure 41: *Left graphs*: Effect of map recalibration on relaxation rates of the belt phantom's samples as measured on MOLLI (A) and T_2-prep TrueFISP (C) maps with a simulated heart-rate of 60 bpm. The gray areas represent the NMR reference values. Recalibrated data are indicated in red, original data in black.
Right graphs: Effect of map recalibration on relaxation times of the Eurospin phantom's samples as measured on MOLLI (C) and T_2-prep TrueFISP (D) maps with a simulated heart-rate of 60 bpm. Recalibrated data are indicated in red, original data in black. The shaded areas represent the confidence level limits, while dotted lines the limits of agreement for the mean values (bold lines). Kolmogorov-Smirnov tests for every data set: p-values > 0.1.

Finally, we tested the feasibility of the recalibration of relaxation time maps obtained from cardiac mapping sequences and acquired with a simulated heart-rate of 60 bpm (see Fig. 41). Reference values for the Eurospin phantom were assessed by means of maps generated from IR-TSE and TSE acquisitions at 22.5°C using the same set-up reported in Fig. 36 using the belt phantom to ensure a correct image acquisition and processing (the acquisitions were performed the same day of cardiac mapping ones).[1]

Due to the linearity of belt phantom MOLLI results we were able to apply the simplest method for map recalibration that is the pixel-wise multiplication for a constant factor of the map (it also reduces the error propagation with respect to more complicated methods): the factor was retrieved from the average of the ratios between MOLLI T_1s and NMR IR ground truth reference ones (Fig. 41.A). All the recalibrated MOLLI values were in agreement with NMR reference values (two-sample t-tests: p-values > 0.1). The effect of the map recalibration on Eurospin's relaxation times can be seen in the Bland-Altman plot in Fig. 41.B: the distribution of recalibrated values (in red) is more centered at 0% discrepancy with respect to the non-recalibrated distribution (in black), hence resulting in a more accurate estimation of the Eurospin's relaxation times without affecting severely the precision ($\sim \pm 10\%$).

The recalibration of the T_2 map from T_2-prep TrueFISP sequence acquisition did not provide the same good results as for the case of MOLLI T_1 map. Due to the non-linearity of belt phantom T_2-prep TrueFISP results, we fitted the ratios between T_2-prep TrueFISP T_2s and NMR CPMG ground truth reference ones with a quadratic function (bijective in the analyzed range of relaxation times) and we applied this function pixel-wise on the T_2 map, hence obtaining the expected behavior of relaxation rates as a function of $MnCl_2$ concentration for the belt phantom values (Fig. 41.C, p-values of two-sample t-tests greater than 0.1). Noticed the severe increment of the errors caused by the error propagation for having used a quadratic function for the recalibration. Eurospin's values, already underestimated (see the black distribution in Fig. 41.D), after the recalibration presented a more severe underestimation (see the red distribution in Fig. 41.D).
Further investigations on the effect of the different nature of the samples (aqueous solutions *vs* gels), probably resulting in a different sensitiveness to this particular sequence, must be performed.

---

[1] Acquisition parameters:

IR-TSE: $FOV = 300 \times 300$ mm^2; $Matrix = 512 \times 512$; $ST = 8$ mm; $FA = 180°$; $T_R = 10$ s; $T_E = 12$ ms; $T_I = 40, 100, 250, 500, 750, 1000, 1500, 3000, 5000, 9670$ ms; $ETL = 27$; $NA = 1$; $PS = 100\%$; $PB = 155$ Hz/pixel.

TSE: $FOV = 300 \times 300$ mm^2; $Matrix = 256 \times 256$; $ST = 8$ mm; $FA = 90°$; $T_R = 10$ s; $T_E = 14, 28, 42, 55, 69, 83, 97, 125, 194, 291$ ms; $ETL = 21$; $NA = 2$; $PS = 75\%$; $PB = 100$ Hz/pixel.

3.3.4 Exp. 3: *In Vivo* Applicability of the Method

We also conducted an in vivo experiment on an untrained volunteer: we acquired MOLLI T_1 and T_2-prep TrueFISP T_2 maps (using the Siemens Aera MRI scanner) of one body slice in the abdomen region, in axial geometry, scanning simultaneously both the volunteer and the $MnCl_2$ samples in a configuration similar to the one proposed in Fig. 25.B. The $MnCl_2$ were placed inside a thermal insulator envelope and positioned on the volunteer's abdomen in a cartridge-like belt configuration. B_0 and B_1 maps were also acquired in order to evaluate potential issues derived from different static and exciting magnetic field conditions. These maps were generated from gradient echo (GRE) acquisitions through, respectively, the dual echo method [75] and the double angle method [76].[2] The temperature of the $MnCl_2$ samples was monitored as in the previous case with the optical fiber sensor TempSense.

RESULTS

In Fig. 42 the maps of the in vivo experiment are reported. The hyperintense signal in the stomach in both relaxation times maps is attributed to food ingested by the volunteer. B_0 and B_1 map show quite homogeneous patterns when comparing the inside regions vs the outside ones. The off-resonance is higher for central $MnCl_2$ samples ($\sim$ 30 Hz) and decrease for lateral ones, while if evaluated in the liver region is around 40 Hz. As can be seen in Fig. 43, the data from of the $MnCl_2$ samples show the same behavior of the previous experiments: MOLLI T_1 values result underestimated but the relaxation rates are linearly dependent with the $MnCl_2$ concentration ($R^2 = 0.997$), as expected from the SBM theory; for T_2-prep TrueFISP R_2 values a plateau can be observed at high concentrations, and the linear dependence with $MnCl_2$ concentration is lost. Also, T_2s resulted underestimated or overestimated for $MnCl_2$ concentrations lower or higher than 0.2 mM, respectively.

The *in vivo* experiment pointed out how different acquisition conditions can influence the mapped relaxation times, hence supporting the necessity of an in-scan reference. In fact, even if the general behaviors of the

---

[2] Acquisition parameters:

MOLLI: $FOV = 418 \times 357$ mm^2; $Matrix = 192 \times 164$; $ST = 8$ mm; $FA = 35°$; $T_R = 262$ ms; $T_E = 1$ ms; $T_I = 100, 180, 363, 443, 625, 705, 885, 1148$ ms; $NA = 1$; $PS = 80.5\%$; $PB = 1085$ Hz pixel^{-1}.

T_2-prep TrueFISP: $FOV = 442 \times 378$ mm^2; $Matrix = 192 \times 164$; $ST = 8$ mm; $FA = 70°$; $T_R = 194$ ms; $T_E = 1$ ms; $T_{E,prep} = 0, 25, 55$ ms; $NA = 1$; $PS = 75.6\%$; $PB = 1185$ Hz pixel^{-1}.

GRE (B_0 map): $FOV = 456 \times 442$ mm^2; $Matrix = 264 \times 256$; $ST = 8$ mm; $FA = 20°$; $T_R = 221$ ms; $T_E = 2.67, 4.87$ ms; $NA = 3$; $PS = 50\%$; $PB = 815$ Hz pixel^{-1}.

GRE (B_1 map): $FOV = 500 \times 421$ mm^2; $Matrix = 256 \times 256$; $ST = 8$ mm; $FA = 45°, 90°$; $T_R = 13$ ms; $T_E = 4.8$ ms; $NA = 26$; $PS = 25\%$; $PB = 420$ Hz pixel^{-1}.

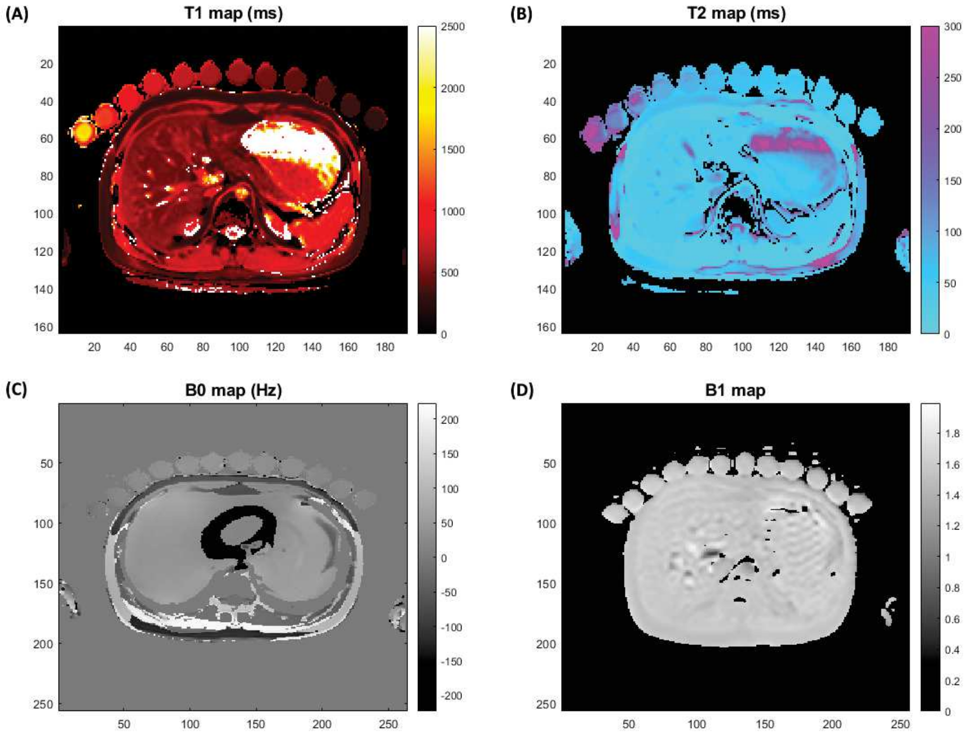

Figure 42: *In vivo* experiment maps of an abdominal axial slice: (A) MOLLI T_1 map; (B) T_2-prep TrueFISP T_2 map; (C) B_0 map; (D) B_1 map, normalized to the nominal flip angle. The darker regions in the Bo map are due to chemical shift artifacts.

relaxation rates are similar to the ones found when scanning the $MnCl_2$ samples alone, the mapped values and their errors, both evaluated with the swSD software, are different (see Figs. 38 and 43). The B_0 inhomogeneities (Fig. 38.C), which are responsible of the artifacts in Fig. 38.B on the samples on the left, do not affect severely the T_2 quantification, since, as can be seen in Fig. 43.B, the behavior of the relaxation rates as a function of the $MnCl_2$ concentration is similar to those of Fig. 38.C (which are the ones related to maps acquired with different field conditions) and, furthermore, the larger discrepancies were found in the region where B_0 was more homogeneous (no artifacts were observable on the samples on the right of Fig. 38.B). Similar considerations can be made to a lesser extent as far as concerns the B_1 inhomogeneities (in fact the B_1 map is more homogeneous, Fig. 38.D): from NMR CPMG experiment conducted on the $MnCl_2$ samples in our laboratory on the NMR spectrometer, the T_2 remains stable within an experimental error of 15% by changing the B_1 up to 50%.

Moreover, in Fig. 43.D, can be seen that the mapped T_2 values of $MnCl_2$ samples do not cover the lower values range of T_2 in the maps: this fact is related to the plateau observable for R_2 data at high $MnCl_2$ concentrations. Further investigations are needed to understand the mechanisms of

T_2-prep TrueFISP sequence that led to the non-linear dependence of relaxation rates with $MnCl_2$ concentration and affected the feasibility of map recalibration (as already pointed out in the Exp. 2). The MOLLI case is completely different (the linearity of R_1 *vs* [$MnCl_2$] is preserved and the mapped T_1 values cover properly the distribution of T_1s): a possible recalibration function was determined through a linear 1-parameter fit of NMR *vs* MOLLI values obtaining $T_{1,true} = 1.07\,T_{1,MOLLI}$. It is noticed that the factor for the MOLLI map recalibration is higher than the one applied by the Siemens software (1.035, see next paragraph).

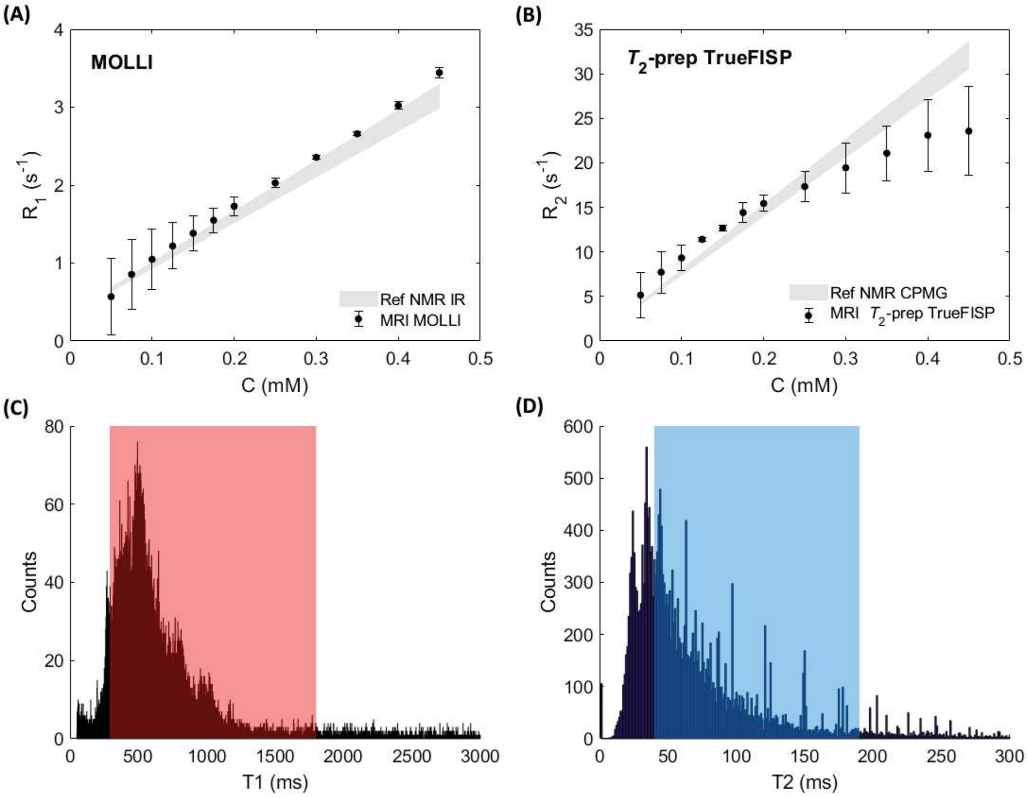

Figure 43: Relaxation rates of the $MnCl_2$ samples in the in vivo experiment: (A) MOLLI T_1 map; (B) T_2-prep TrueFISP T_2 map. The histograms in the bottom show the distribution on the maps of the relaxation times, respectively, T_1 (C) and T_2 (D). The red and blue shaded areas represent the ranges covered by the values measured on the relaxation times maps of the $MnCl_2$ samples (*i.e.* the mapped values, not the real ones). Temperature of the $MnCl_2$ samples as measured with TempSense: 25.2°C.

CLINICAL ASPECTS As a last observation on the belt phantom, it is important to remark that the explored wide ranges of both heart-rates (HR $= 30 - 150$ bpm) and relaxation times at $B_0 = 1.5$ T ($T_1 = 300 - 1500$ ms ca.; $T_2 = 30 - 250$ ms ca.) were chosen to stress the system in ideal motion-free conditions.
In clinical cardiological applications at $B_0 = 1.5$ T the usual ranges are [77]: (i) HR $= 40 - 120$ bpm, since HR values below or over these cut-offs are critical from a clinical point of view and affect severely the quality of the acquired images preventing a reliable reconstruction of the maps; (ii) $T_1 = 500 - 1200$ ms [7] ($R_1 = 0.8 - 2$ s^{-1}), with the lowest T_1 values detected in thalassemia major patients with severe iron overload and the highest T_1 values found in patients affected by myocardial edema or amyloidosis and (iii) $T_2 = 40 - 70$ ms [7] ($R_2 = 14 - 25$ s^{-1}), with the two extremes that correspond, respectively, to thalassemia major patients and to patients with myocardial edema (*e.g.* acute myocarditis or acute myocardial infarction). Usual normal reference values fall within the ranges $T_1 = 900 - 1000$ ms, and $T_2 = 45 - 50$ ms [7, 9, 10, 51]: for example, from previous studies performed by the Department of Cardiology of the Niguarda Hospital were found $T_1 = 984 \pm 30$ ms as normal reference value for MOLLI sequences, and $T_2 = 45 \pm 2$ ms for T_2-prepTrueFISP sequences. It is also noteworthy that the indicated relaxation time values (both the normal and the pathological ones) depend on the sequence, the scanner, the software and are in general different from study to study [9, 10, 78]. Moreover, this work considers the possibility of applying MOLLI and T_2-prep TrueFISP sequences to other body districts with respect to the heart that are characterized by different relaxation time ranges [5, 79–82].

3.3.5 Software Comparison

The Bland-Altman plots of the comparisons between the results obtained with the different software used in this study are illustrated in Fig. 44: in particular, the plots 44.A, 44.B, 44.C, and 44.D validate the measurements done with the swSD software, proving that they are statistically coincident with Segment's ones within 1% for T_1 and 3% for T_2 limits of agreement.

In Fig. 44 the variation that could arise in measuring the relaxation times employing different software can also be seen (plots 44.E and 44.F). The longitudinal relaxation time T_1 values extracted from MOLLI obtained using the Siemens' software are higher than those resulting from swSD by a factor of 1.035. This numerical correction applied to T_1 MOLLI maps compensates for a T_1 underestimation due to the imperfection of the excitation 180° pulse [70, 83].

From the comparison analysis between T_2-prep TrueFISP results from Siemens' software and swSD, for which an average overestimation of $\sim$ 5%, a trend is observable: the discrepancies are wider for lower T_2s and become lower with increasing T_2. This trend reflects the increment of the percentage errors measured with the swSD software on the belt phantom samples with increasing $MnCl_2$ concentration (see Fig. 39). This effect is not present in the comparison between Segment and swSD T_2-prep TrueFISP results since the computational details of the two software are much more similar than Siemens' one.

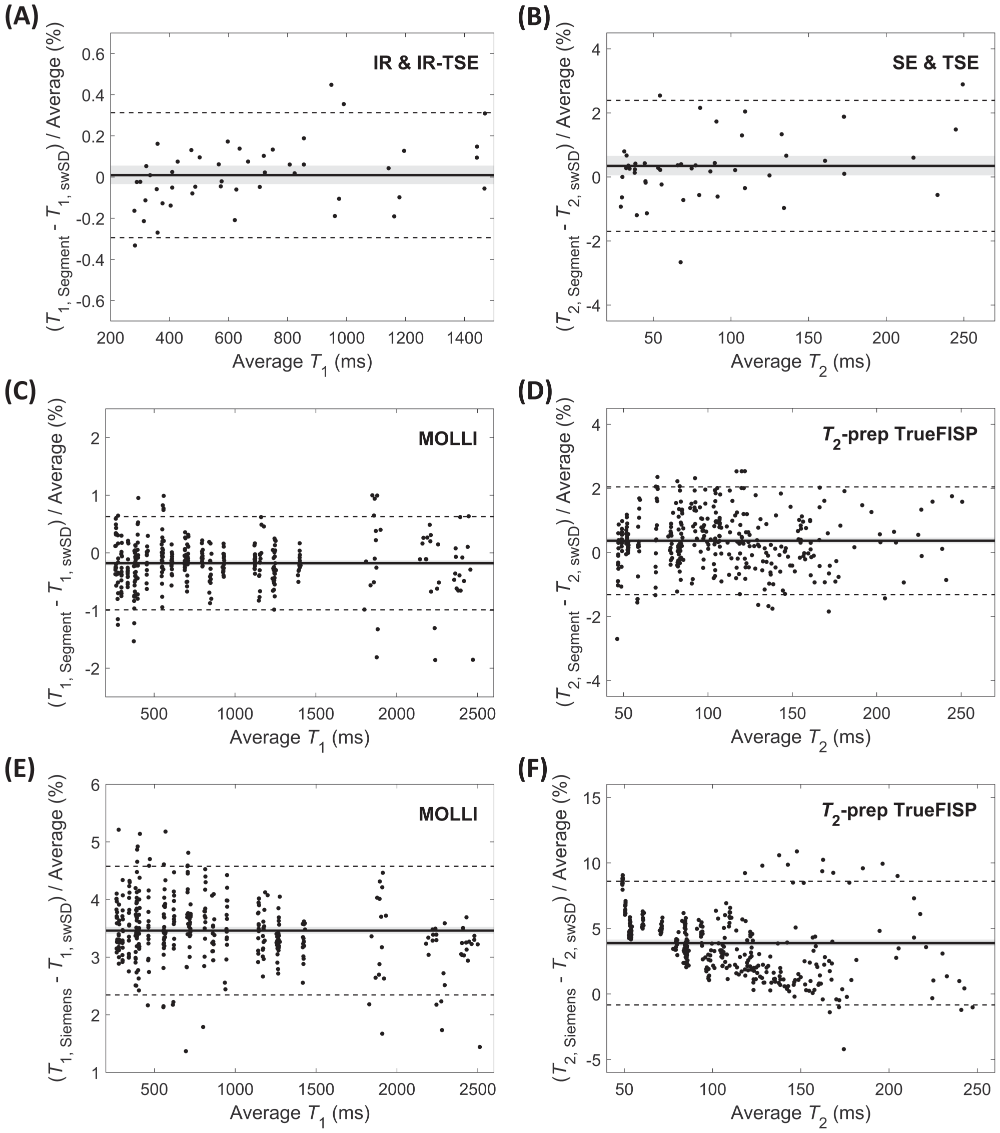

Figure 44: Bland-Altman plots of the comparisons between the results concerning the relaxation time T_1 (left column: A, C, and E) and T_2 (right column: B, D, and F) obtained with different software: Segment *vs* swSD (A, B, C, and D); Siemens VE11C MyoMaps *vs* swSD (E and F). Kolmogorov-Smirnov tests for the normality were performed for every data-set to ensure the applicability of the Bland-Altman analysis resulting in p-values > 0.1 in all cases. The dotted lines represent the limits of agreement, from $-1.96s$ to $+1.96s$ (s is the standard deviation), while the grey areas represent the confidence interval limits for the mean values (bold black lines).

3.4 CONCLUSIONS

In this work, we have presented a methodology for a scanner-independent and center-independent evaluation of the values of T_1 and T_2 using mapping sequences, as a step towards data harmonization and optimization. The method relies on a robust and well-controlled NMR laboratory T_1 and T_2 calibrating measurements, that singled out the discrepancies between maps and reference values: the temperature of the reference samples at the moment of the acquisition unveils the true values of their relaxation times. It has been shown that our method based on reference $MnCl_2$ aqueous solution samples can be easily applied for the assessment of both precision and accuracy of relaxation time maps in any experimental acquisition/analysis protocol, *i.e.* different MRI scanners, sequences, software, as well as clinical conditions (heart-rates, temperature, etc.). It is worth noting the remarkable case of T_2-prep TrueFISP, for which the T_2 values deduced from such MRI sequence are overestimated with respect to the theoretically expected behavior, by a factor that is enhanced with $1/T_2$ increase.
To test the applicability of our method to a statistically significant number of *in vivo* cases, further studies are needed. However, we guess that the use of a cartridge-like belt of $MnCl_2$ samples, joint to the combined analysis of T_1 and T_2 maps and of the related SD maps, could become a powerful instrument for the recalibration of the relaxation time maps acquired *in vivo* with fast mapping sequences.

NOTE We are currently investigating on the *in vivo* feasibility of the methodology taking particular attention to the placement of the samples in order to avoid possible surface effects and B_0/B_1/susceptibility issues on the relaxation time maps, as well as considering the increment of FOV requirements, the patient discomfort, and the temperature monitoring and stability during the scan. Preliminary attempts on untrained volunteers seem to support the applicability of the method (see Fig. 42).
The project of a year-long clinical trial was canceled due to the global pandemic of SARS-CoV-2 and will be probably started after the end of the doctorate course of the candidate.

4

INSIGHT OF CA MECHANISMS: STUDY OF LN-DOTA COMPLEXES

In this Chapter, a study on the characterization of contrast agents for high-field MRI applications will be presented. This work was developed in collaboration with the Department of Chemistry of the University of Florence (Italy) and with the Department of Physics of the University of Milan (Italy).

The study presented in this Chapter have been published on the Journal of Chemical Physics in a paper entitled *Longitudinal and transverse NMR relaxivities of Ln(III)-DOTA complexes: a comprehensive investigation* by Cicolari *et al.* [84].

NOTE Following the usual nomenclature in the MRI field, in this Section the magnetic induction ***B*** will be referred to as *magnetic field*.

4.1 RATIONALE

The Magnetic Resonance Imaging (MRI) contrast agents have been extensively studied in the last 40 years and their use in medicine is widespread, especially for the most common applications at 1.5 and 3 T [15]. The main property that allows these systems to enhance the MRI sensitivity is the ability of improving the image contrast, taking advantage of their capability to increase the nuclear relaxation rates. For their characterization, Nuclear Magnetic Resonance (NMR) is commonly employed for collecting nuclear relaxivity data, *i.e.* the relaxation rate increment (with respect to the pure solvent) normalized to 1 mM concentration of the contrast agent (CA), as a function of the Larmor resonance frequency $\nu = (\gamma/2\pi)B_0$, where γ is the gyromagnetic ratio of the nuclear species, usually ^{1}H, and B_0 is the applied static magnetic field. The acquired data generate the so-called Nuclear Magnetic Relaxation Dispersion (NMRD) profiles, that can be analyzed according to models based on the Solomon-Bloembergen-Morgan (SBM) theory [16–19, 43] for obtaining information on the chemical exchange time, the minimum approach distance of the water to the magnetic ion, the molecular dynamics (Brownian rotation), and the electron spin dynamics and the magnetic interactions of the CA molecule with the surrounding environment [85–87].

The MRI CAs are usually composed of a paramagnetic center, typically a metal ion, surrounded by a chelate, which allows biological compatibility and favors the 'safe' residence in the body and the correct elimination from the organism of the CA after its injection [15]. Their design is based on the Paramagnetic Relaxation Enhancement (PRE) mechanism [88], which, as already explained in Section 2.3 and here reported for sake of clarity, causes a local increase of both nuclear longitudinal $R_1 = 1/T_1$ and transverse $R_2 = 1/T_2$ relaxation rates of tissues, where T_1 is the spin-lattice relaxation time and T_2 is the spin-spin relaxation time. The PRE mechanism causes the desired improvement of the image contrast and, depending on their effect on T_1 or T_2, CAs can be classified as: (i) *positive* CAs that produce brighter zones reducing mainly T_1; (ii) *negative* CAs that cause darker spots reducing mainly T_2. For obtaining generally a positive contrast, as paramagnetic center the Gd(III) ion provides the best nuclear relaxation rate enhancement, if compared to the other ions of the lanthanide series, due to its long electronic relaxation time. This occurrence explains the extensive employment of Gd(III) complexes as positive CA in MRI. Other Ln(III) complexes (especially Dy(III) complexes), characterized by short electronic relaxation times, are more often used as shift agents for NMR spectroscopic applications. On the other hand, because of the recent development of very high-field scanners for the human body [89–92], materials belonging to the same family of the most used CAs, but scarcely explored, have been suggested [20, 93, 94]. Example of such materials are the non-Gd Ln(III)-based compounds [22, 95, 96], that, as their paramagnetic transverse relaxation rate contribution depends on the square of the chemical shift (proportional to the magnetic field) [21, 22], have been proposed as potential negative CAs for high-field applications [23, 97–100].

In the present work we investigated the NMRD profiles of four different Ln(III)-DOTA complexes in aqueous solutions (Ln = Gd, Dy, Tb, Er; DOTA = 1,4,7,10 - tetraazacyclododecane - N,N',N",N"' - tetraacetic acid) and of $[Mn(H_2O)_6]^{2+}$ aqua ions, for comparison, combining the analysis of both longitudinal and transverse relaxivity data acquired in a wide range of frequencies (from 10 kHz up to 700 MHz). Accordingly to the literature, this combined approach allows to determine the main physico-chemical quantities that influence the MRI contrast agent's efficiency [22]. The data were analyzed considering both the quenched (Gd(III) and Mn(II)) or unquenched (Dy(III), Tb(III) and Er(III)) orbital angular momentum, and the presence of the so-called Curie relaxation [44]. The latter contribution is efficient when the magnetic dipolar interaction between the nuclear spins and the thermal average of the electronic spin is modulated by the molecular motion. Noticeably, the Curie contribution is singled out when the electronic correlation time is short [101, 102]. Furthermore, the efficiency of Dy-DOTA, Tb-DOTA, and Er-DOTA at high fields as both positive and negative MRI CAs is shown by contrast images collected at 7 T employing a pre-clinical scanner.

In the following sections we will present: the theoretical basis of models of longitudinal and transverse NMRD profiles, the experimental details, the obtained results, and the correlated discussion.

4.2 SAMPLES

In Fig. 45.A the chemical formula of the macrocyclic ligand DOTA (1,4,7,10 - tetraazacyclododecane - N,N′,N″,N‴ - tetraacetic acid) is reported, and in Fig. 45.B and C a top and a side view of the contrast agent molecule composed by a paramagnetic lanthanide metal center and the DOTA ligand can be seen respectively. In particular, the capped square-antiprism structure can be well appreciated.

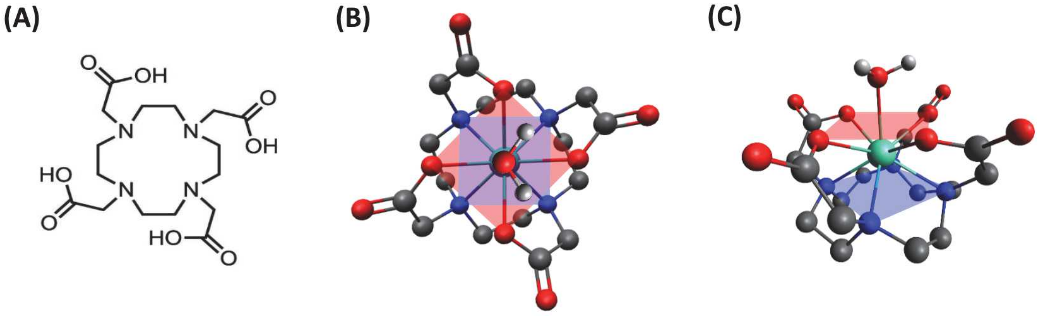

Figure 45: (A) Chemical formula of the macrocyclic DOTA ligand (1,4,7,10 - tetraazacyclododecane - N,N′,N″,N‴ - tetraacetic acid). (B) Top and (C) side view of the capped square-antiprism Ln-DOTA molecule (for sake of simplicity only the capped water hydrogens are illustrated). The atoms are colored as follows: white = H, gray = C, red = O, blue = N, teal = Ln. In Figure are also highlighted the parallel O_4-plane (red) and the N_4-plane (blue) of the antiprism.

We considered two ions with $L = 0$, *i.e.* Gd(III) and Mn(II). Indeed, Gd(III) represents a standard in MRI and it is widely used. Conversely, Mn(II) has been poorly exploited so far, but it has been recently proposed as a valid alternative to Gd(III) complexes [103–105]. In this work, as already mentioned, we used Mn(II) aqua ions as reference for the other Ln-DOTA complexes.

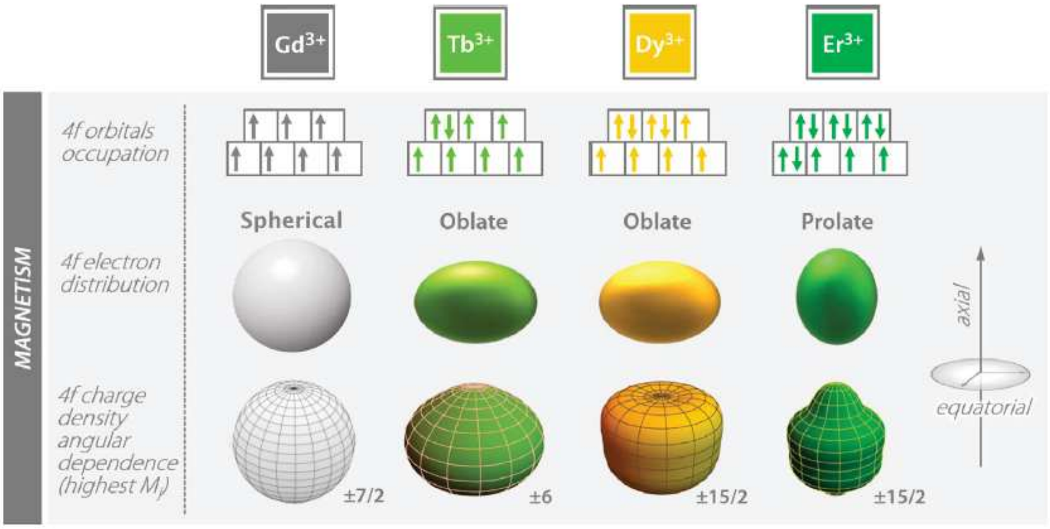

Figure 46: Ln(III) ions magnetic properties: 4f orbitals occupation, 4f electron distribution and 4f charge density angular dependence. Source [25].

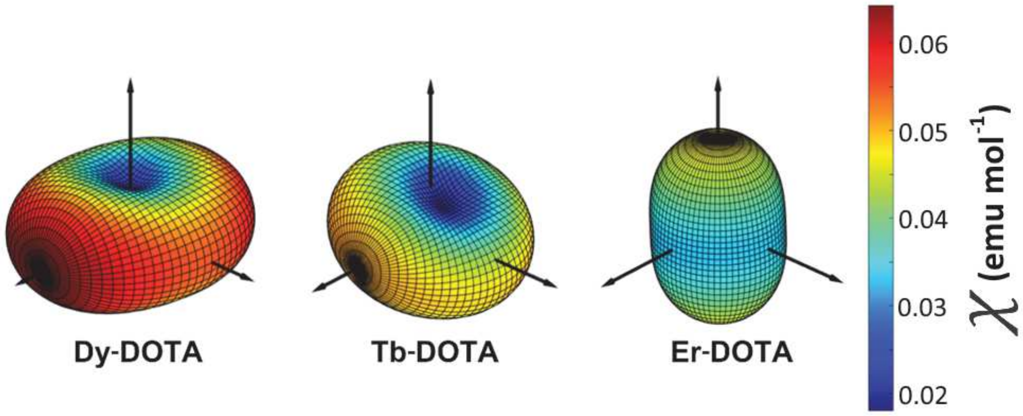

Figure 47: Magnetic susceptibility tensor of Dy-DOTA, Tb-DOTA and Er-DOTA calculated at $T = 298$ K and $B_0 = 1$ T using the Crystal Field parameters reported in the recent work of Briganti *et al.* [106]. The color scale refers to the value of the magnetic susceptibility. The vertical arrow in the three plots coincides with the direction of the lanthanide-water bond.

Among the possible anisotropic lanthanide ions ($L \neq 0$), we have chosen Dy(III), Tb(III) and Er(III) due to several reasons. In Fig. 46 the main magnetic properties of the trivalent Ln(III) ions considered in this study are summarized: their paramagnetism arises from the large number of unpaired 4f electrons, which are only marginally involved in the formation of chemical bonds since they are shielded by the 5s and 5p shells. From a chemical point of view, these ions have similar radii and comparable kinetic constants for the solvent exchange processes [107–110]. The magnetic anisotropy of all these ions is comparable and remarkably high at room temperature. A plot of susceptibility tensors of these ions in the Ln-DOTA complexes, computed at room temperature using crystal field parameters recently reported for the whole DOTA series [106], is reported in Fig. 47. The magnetic anisotropy of Dy and Tb is substantially easy plane while the magnetic anisotropy of Er is easy axis.

4.3 SBM MODELS

As already shown in Chapter 2 (Section 2.3), here reported for sake of clarity, the relaxation rate enhancement caused by a paramagnetic species diluted in a diamagnetic solvent (*e.g.* water) can be expressed as

$$R_{i,p} = r_i C = R_{i,obs} - R_{i,dia} \quad \text{with } i = 1,2 \tag{50}$$

where $R_{i,obs}$ and $R_{i,dia}$ are the relaxation rates of the solution and of the solvent respectively, while the paramagnetic contribution $R_{i,p}$ is expressed in terms of the concentration of the paramagnetic species C, usually given in mM (1 mM = 1 mmol l^{-1}), and of the relaxivity r_i (in units of $mM^{-1}\ s^{-1}$). The paramagnetic terms $R_{i,p}$ can be separated in two sub-terms, according to the intra- or inter-molecular nature of the interactions, namely the Inner- (IS) and Outer-sphere (OS) contribution respectively : $R_{i,p} = R_{i,IS} + R_{i,OS}$.

Let us now split the theoretical model of nuclear relaxation into two cases depending on the characteristics of the paramagnetic center:

- for Gd-DOTA and $[Mn(H_2O)_6]^{2+}$, $L = 0$ and negligible Curie contribution;
- for Dy(III), Tb(III), and Er(III) complexes, $L \neq 0$ and non-negligible Curie contribution.

The motivation of this choice is correlated to the different interactions considered in the SBM model: in the former case the dipolar and scalar interactions dominate the relaxation mechanism due to the longer electronic correlations times ($\gg 1$ ps); in the second case, due to short relaxation times (< 1 ps) the dipolar and scalar interactions give a much smaller contribution to the nuclear relaxation and at high fields the Curie contribution dominates.

CASE WITH $L = 0$

For ions characterized by null orbital angular momentum ($L = 0$), such as Gd(III) and Mn(II), the two major contributions to the relaxivity arise from the dipolar (DD) and the scalar (also named contact or hyperfine, SC) interactions. The contribution from the Curie can be neglected [15].
The equations expressing the inner-sphere contribution of the longitudinal and transverse relaxation rates $R_{i,IS}$ are given by:

$$R_{1,IS} = \left(\frac{1}{T_1}\right)^{IS} = fq\,\frac{1}{T_{1m} + \tau_m} \tag{51}$$

$$R_{2,IS} = \left(\frac{1}{T_2}\right)^{IS} = \frac{fq}{\tau_m}\,\frac{T_{2m}^{-2} + \tau_m^{-1}T_{2m}^{-1} + \Delta\omega_m^2}{(\tau_m^{-1} + T_{2m}^{-1})^2 + \Delta\omega_m^2} \tag{52}$$

where f is the ratio between the concentration of the paramagnetic species and the water ($f = C/55500$), q is the number of bound water molecules per paramagnetic ion (hydration number), T_{im} (with $i = 1, 2$) are the proton relaxation times of the coordinated water, τ_m is the lifetime of the first coordination sphere's water molecules of the complex exchanging with the bulk (also known as water exchange time), and $\Delta\omega_m$ is the chemical shift of the coordinated water molecule. In particular, $\Delta\omega_m$ is proportional to the magnetic field and results from the sum of a contact term $\Delta\omega_m^{cont} = g\mu_B S(S+1)(A/\hbar)[1/(3k_B T)]B_0$ where B_0 is the applied magnetic field, k_B is the Boltzmann constant and T is the temperature, and one term related to the rotational average of the dipole-dipole interaction (also known as pseudocontact) [15, 22, 111]. The equations for the two different contributions (DD and SC) to the proton relaxation rates ($1/T_{im}$) of the coordinated water molecule are:

$$\left(\frac{1}{T_{im}}\right) = \left(\frac{1}{T_i^{DD}}\right)^{IS} + \left(\frac{1}{T_i^{SC}}\right)^{IS} \quad \text{with } i = 1, 2 \tag{53}$$

where

$$\left(\frac{1}{T_1^{DD}}\right)^{IS} = \frac{2}{15}\left(\frac{\mu_0}{4\pi}\right)^2 \frac{\gamma_I^2 g^2 \mu_B^2}{r^6}\, S\,(S+1) \times \\ \times \left[7\,\frac{\tau_{c2}}{1 + \omega_S^2\tau_{c2}^2} + 3\,\frac{\tau_{c1}}{1 + \omega_I^2\tau_{c1}^2}\right] \tag{54}$$

$$\left(\frac{1}{T_1^{SC}}\right)^{IS} = \frac{2S\,(S+1)}{3}\left(\frac{A}{\hbar}\right)^2 \left(\frac{\tau_{e2}}{1 + \omega_S^2\tau_{e2}^2}\right) \tag{55}$$

and

$$\left(\frac{1}{T_2^{DD}}\right)^{IS} = \frac{1}{15}\left(\frac{\mu_0}{4\pi}\right)^2 \frac{\gamma_I^2 g^2 \mu_B^2}{r^6} S\left(S+1\right) \times$$
$$\times\left[13\,\frac{\tau_{c2}}{1+\omega_S^2\tau_{c2}^2} + 3\,\frac{\tau_{c1}}{1+\omega_I^2\tau_{c1}^2} + 4\,\tau_{c1}\right] \quad (56)$$

$$\left(\frac{1}{T_2^{SC}}\right)^{IS} = \frac{S\left(S+1\right)}{3}\left(\frac{A}{\hbar}\right)^2\left(\frac{\tau_{e2}}{1+\omega_S^2\tau_{e2}^2} + \tau_{e1}\right) \quad (57)$$

where γ_I is the gyromagnetic ratio of the observed nucleus, g is the electron g-factor, μ_B is the Bohr magneton, r is the distance between the paramagnetic ion and the observed nucleus, S is the spin quantum number, μ_0 is the vacuum magnetic permeability, $A/\hbar$ is the scalar (or hyperfine) coupling constant between the electron spin of the paramagnetic ion and the proton spin of the coordinated water, ω_I and ω_S are the nuclear and electron angular precession frequencies. The correlation times τ_{ci} and τ_{ei} ($i = 1, 2$) modulate the dipolar and the scalar interactions and are given by: $\tau_{ci}^{-1} = \tau_m^{-1} + \tau_r^{-1} + T_{ie}^{-1}$ and $\tau_{ei}^{-1} = \tau_m^{-1} + T_{ie}^{-1}$, where τ_r is the rotational correlation time of the complex, and T_{ie} are the electronic relaxation times.

In the Redfield limit (see below) and for metal complexes with $S \geq 1$, the electronic relaxation rates ($1/T_{ie}$, $i = 1, 2$) are usually written by taking into account the zero-field-splitting (ZFS) interaction as follows:

$$\left(\frac{1}{T_{1e}}\right)^{ZFS} = 2\mathfrak{C}\left(\frac{1}{1+\omega_S^2\tau_v^2} + \frac{4}{1+4\omega_S^2\tau_v^2}\right) \quad (58)$$

$$\left(\frac{1}{T_{2e}}\right)^{ZFS} = \mathfrak{C}\left(\frac{5}{1+\omega_S^2\tau_v^2} + \frac{2}{1+4\omega_S^2\tau_v^2} + 3\right) \quad (59)$$

with $\mathfrak{C} = 1/50\,\Delta^2\tau_v[4S(S+1)-3]$, where Δ^2 is the mean squared fluctuation of the ZFS, which is related to the ZFS parameters D_{ZFS} and E_{ZFS} (*i.e.* the axial and transverse component of the magnetic anisotropy) by the relation $\Delta^2 = 2/3\,D_{ZFS}^2 + 2\,E_{ZFS}^2$, and τ_v is the ZFS modulation correlation time. $\mathfrak{C}$ can be expressed in terms of the low-field electronic relaxation time τ_{S0} as $\mathfrak{C} = 0.1/\tau_{S0}$ in order to highlight its temporal meaning. In the limit $\omega_S^2\tau_v^2 \ll 1$, $T_{1e} = T_{2e} = \tau_{S0}$. The Redfield limit is given by $\Delta^2\tau_v^2 \ll 1$ [112].

The equations for the outer-sphere longitudinal and transverse proton relaxation rates of bulk water molecules $R_{i,OS} = (1/T_i^{DD})^{OS}$ (with $i = 1, 2$) are related only to the dipolar interaction and are given by:

$$\left(\frac{1}{T_1^{DD}}\right)^{OS} = \frac{32\pi}{405}\left(\frac{\mu_0}{4\pi}\right)^2 \frac{N_A C}{dD}\,\gamma_I^2 g^2 \mu_B^2\, S\,(S+1) \times \\ \times \left[7\, j_2\,(\omega_S) + 3\, j_1\,(\omega_I)\right] \quad (60)$$

$$\left(\frac{1}{T_2^{DD}}\right)^{OS} = \frac{16\pi}{405}\left(\frac{\mu_0}{4\pi}\right)^2 \frac{N_A C}{dD}\,\gamma_I^2 g^2 \mu_B^2\, S\,(S+1) \times \\ \times \left[13\, j_2\,(\omega_S) + 3\, j_1\,(\omega_I) + 4\, j_1\,(0)\right] \quad (61)$$

where N_A is the Avogadro number, d is the distance of minimum approach for bulk water molecules to the paramagnetic center, D is the relative self-diffusion constant, and $j_k(\omega)$ is the spectral density function for the dipolar interaction given by the equation:

$$j_k\,(\omega) = \mathrm{Re}\left\{\frac{1 + z/4}{1 + z + 4\, z^2/9 + z^3/9}\right\} \quad (62)$$

where $z = \sqrt{i\omega\tau_D + \tau_D/T_{ke}}$ (with $k = 1, 2$), and $\tau_D = d^2/D$ is the translational correlation time.

CASE WITH $L \neq 0$

For ions characterized by non-null orbital angular momentum ($L \neq 0$), such as Dy(III), Tb(III), and Er(III), the electronic relaxation time is shorter, the DD and SC contributions are small, and, as a consequence, the Curie contribution dominates at high fields [22, 101].

The equations for the inner-sphere contributions of the longitudinal and transverse relaxation rates $R_{i,IS}$ are, again, given by Eqs. 51 and 52, but the proton relaxation rates are now expressed as

$$\left(\frac{1}{T_{im}}\right) = \left(\frac{1}{T_i^{DD}}\right)^{IS} + \left(\frac{1}{T_i^{SC}}\right)^{IS} + \left(\frac{1}{T_i^{Curie}}\right)^{IS} \quad \text{with } i = 1, 2 \quad (63)$$

The equations for the inner-sphere terms Eqs. 54 to 57 are still valid when applying the following corrections: g must be substituted with the Landé g-factor g_j and S with the total spin quantum number J. The Curie contributions to the proton relaxation rates are expressed as:

$$\left(\frac{1}{T_1^{Curie}}\right)^{IS} = \frac{2}{5}\left(\frac{\mu_0}{4\pi}\right)^2 \frac{\gamma_I^2 B_0^2 g_j^4 \mu_B^4 J^2 \left(J+1\right)^2}{r^6} \times \\ \times \frac{1}{\left(3\, k_B T\right)^2}\left[\frac{3\,\tau_{cc}}{1+\omega_S^2\tau_{cc}^2}\right] \tag{64}$$

$$\left(\frac{1}{T_2^{Curie}}\right)^{IS} = \frac{1}{5}\left(\frac{\mu_0}{4\pi}\right)^2 \frac{\gamma_I^2 B_0^2 g_j^4 \mu_B^4 J^2 \left(J+1\right)^2}{r^6} \times \\ \times \frac{1}{\left(3\, k_B T\right)^2}\left[\frac{3\,\tau_{cc}}{1+\ \omega_I^2\tau_{cc}^2} + 4\,\tau_{cc}\right] \tag{65}$$

The equations for the outer-sphere contributions result now from the sum of two terms, the dipolar and the Curie ones, and assume the form

$$R_{i,OS} = \left(\frac{1}{T_i^{DD}}\right)^{OS} + \left(\frac{1}{T_i^{Curie}}\right)^{OS} \quad \text{with } i = 1,\, 2 \tag{66}$$

where

$$\left(\frac{1}{T_1^{DD}}\right)^{OS} = \frac{16\pi}{135}\left(\frac{\mu_0}{4\pi}\right)^2 \frac{N_A C}{dD}\gamma_I^2 g^2 \mu_B^2 \times \\ \times \left\{6\left[J\left(J+1\right) - S_c \coth\frac{\chi}{2J} - S_c^2\right] j_1\left(\omega_I\right) + 7\coth\frac{\chi}{2J} S_c j_2\left(\omega_S\right)\right\} \tag{67}$$

$$\left(\frac{1}{T_2^{DD}}\right)^{OS} = \frac{16\pi}{135}\left(\frac{\mu_0}{4\pi}\right)^2 \frac{N_A C}{dD}\gamma_I^2 g^2 \mu_B^2 \times \\ \times \left\{\left[J\left(J+1\right) - S_c \coth\frac{\chi}{2J} - S_c^2\right]\left(3\, j_1\left(\omega_I\right) + 4\, j_1\left(0\right)\right)\right\} + \\ + \frac{16\pi}{135}\left(\frac{\mu_0}{4\pi}\right)^2 \frac{N_A C}{dD}\gamma_I^2 g^2 \mu_B^2 \left[6.5\coth\frac{\chi}{2J} S_c j_2\left(\omega_S\right)\right] \tag{68}$$

and

$$\left(\frac{1}{T_1^{Curie}}\right)^{OS} = \frac{32\pi}{45}\left(\frac{\mu_0}{4\pi}\right)^2 \frac{N_A C}{dD}\gamma_I^2 g^2 \mu_B^2\, S_c^2\, j\left(\omega_I\right) \tag{69}$$

$$\left(\frac{1}{T_2^{Curie}}\right)^{OS} = \frac{16\pi}{45}\left(\frac{\mu_0}{4\pi}\right)^2 \frac{N_A C}{dD}\,\gamma_I^2 g^2 \mu_B^2\, S_c^2\, \left\{3\,j\left(\omega_I\right) + 4\,j\left(0\right)\right\} \tag{70}$$

where $\chi = JB_0\mu_B g_j/(k_B T)$ and $S_c = JB_J(\chi)$ is the time-averaged or 'Curie' spin given by the product of J with the Brillouin function $B_J(\chi)$ [44, 113] and being τ_{cc} the correlation time for the Curie contribution ($\tau_{cc}^{-1} = \tau_m^{-1} + \tau_r^{-1}$) and $j(\omega)$ the spectral density function for the dipolar interaction $j_k(\omega)$ in the limit of $T_{ie} \to \infty$.

4.4 EXPERIMENTAL DETAILS

4.4.1 Samples Preparation

Crystalline powders of Na[LnDOTA(H$_2$O)] · 4 H$_2$O, with Ln(III) = Gd(III), Dy(III), Tb(III), and Er(III) and DOTA = 1,4,7,10 - tetraazacyclododecane - N,N',N",N"' - tetraacetic acid were obtained following the procedure reported in previous works [114–116]. Manganese(II) chloride tetrahydrate powders (formula MnCl$_2$ · 4 H$_2$O, molar mass 197.91 g/mol) were supplied by Sigma-Aldrich Co., St. Louis, MO, USA.

All the solutions were prepared by diluting the compounds powders in MilliQ water and obtaining the following concentrations: [MnCl2] = 0.65 mM, [Gd-DOTA] = 1.082 mM, [Dy-DOTA] = 17.3 mM, [Tb-DOTA] = 11 mM, and [Er-DOTA] = 15.5 mM. The evaluation of the chemical shifts for the LnDOTA complexes (Ln $\neq$ Gd) was performed collecting the solutions spectra at 400 MHz and 700 MHz and by adding a small amount of trimethylsilylpropanoic acid (TSP) for the frequency lock: this step was done after the acquisition of all the NMRD profiles. Furthermore, two additional sets of Dy-DOTA, Tb-DOTA, and Er-DOTA samples with 100 mM and 5 mM concentrations were prepared for low-field T_2 measurements ($\nu \leq 3$ MHz) and MRI acquisitions, respectively.

4.4.2 Relaxometry

The NMRD profiles of the different aqueous solutions were acquired at room temperature $T = 298$ K by measuring the spin-lattice relaxation time T_1 and the spin-spin relaxation time T_2 at several Larmor resonance frequencies (*i.e.* at different external magnetic field strengths). Several devices and techniques, summarized in Table 4, were employed to span a wide range of frequencies ν, from 0.01 MHz up to 700 MHz, corresponding to a broad range of magnetic field strength $2.35 \times 10^{-4} < B_0 < 16$ T.

We employed standard NMR techniques [4] for relaxation times measurements above 7.2 MHz, while below 7.2 MHz we used the Fast-Field-Cycling

(FFC) techniques [117, 118]. All T_1 measurements were performed employing either the Saturation (SR) or the Inversion Recovery (IR) pulse-sequences. To quantify T_2, we used the Carr-Purcell-Meiboom-Gill (CPMG) sequence for frequency above 3 MHz, and the Spin-Echo (SE) sequence for frequency below 3 MHz.

Table 4: NMRD profiles acquisition instrumentation and techniques according to specific ranges of frequencies.

Frequency (MHz)	Instrumentation	Techniques
0.01 − 3	Stelar SMARTracer Relaxometer	FFC-PP (SR + SE)
3 − 7.2	Stelar SMARTracer Relaxometer	FFC-NP (SR + CPMG)
7.2 − 60	Stelar Spinmaster Spectrometer	NMR (SR + CPMG)
7.2 − 298	Tecmag Apollo Spectrometer + Bruker EM / SCM	NMR (SR + CPMG)
400	Bruker FT-NMR Avance Spectrometer	NMR (IR + CPMG)
700	Bruker Avance NEO Spectrometer	NMR (IR + CPMG)

Stelar s.r.l., Mede, Italy; Tecmag, Houston, TX, USA; Bruker, Billerica, MA, USA.

EM = Electromagnet; SCM = Superconducting Magnet; PP = Pre-Polarized; NP = Non-Polarized.

The raw data were then fitted to an exponential recovery function for T_1 (signal intensity vs different saturation/inversion times), or to an exponential decay function for T_2 (signal intensity vs different echo-times). An experimental error of 8% was assigned to all the experimental data, based on previous studies on the *a priori* error outlined for the different experimental setups due to the electronic chain.

4.4.3 *In vitro* Magnetic Resonance Imaging

MRI acquisitions were performed at 0.18 T ($\nu = 7.74$ MHz) on an Artoscan Imager (Esaote, Genova, Italy) and at 7 T ($\nu = 298$ MHz) on a PharmaScan Scanner (Bruker, Billerica, Massachusetts, USA). The images were acquired at room temperature of 2 ml vials filled with 5 mM aqueous solutions of Dy-DOTA, Tb-DOTA, and Er-DOTA. We acquired two series of Spin-Echo images for each magnetic field strength, the first one varying the repetition time (T_R) and the second one changing the echo time (T_E). The acquisition parameters can be summarized as follows:

- *Esaote Artoscan Imager* (0.18 T, $\nu = 7.74$ MHz):
    1. T_1-weighted sequence. T_R = 100, 300, 500 ms; T_E = 20 ms; Acquisition Matrix 256 × 192; Reconstruction Matrix 256 × 256; FOV = 12 × 12 cm^2; Slice Thickness = 5 mm; Averages = 10.
    2. T_2-weighted sequence. T_E = 28, 90, 120 ms; T_R = 2.8 s; Acquisition Matrix 256 × 192; Reconstruction Matrix 256 × 256; FOV = 12 × 12 cm^2; Slice Thickness = 5 mm; Averages = 1.

- *Bruker PharmaScan Scanner* (7 T, $\nu = 298.03$ MHz):
  1. T_1-weighted sequence. T_R = 100, 300, 500 ms; T_E = 20 ms; Acquisition Matrix 256 × 192; Reconstruction Matrix 256 × 256; FOV = 4 × 4 cm^2; Slice Thickness = 1 mm; Averages = 3.
  2. T_2-weighted sequence. T_E = 28, 90, 120 ms; T_R = 2.8 s; Acquisition Matrix 256 × 192; Reconstruction Matrix 256 × 256; FOV = 4 × 4 cm^2; Slice Thickness = 1 mm; Averages = 1.

4.5 DATA ANALYSIS AND DISCUSSION

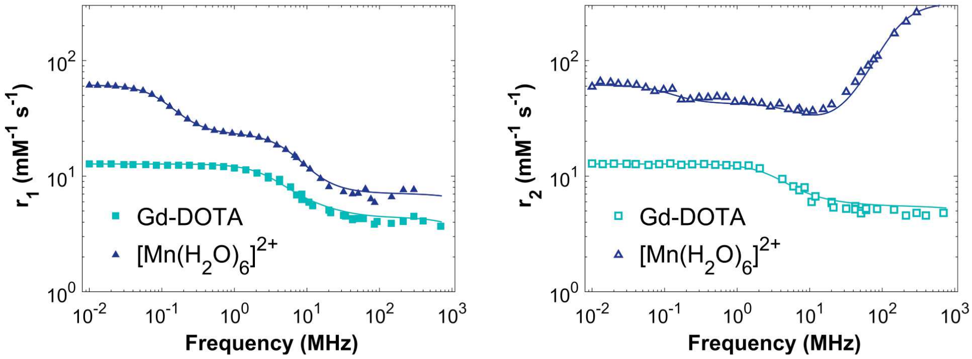

Figure 48: Longitudinal (left) and transverse (right) relaxivity ^{1}H NMRD profiles of Gd-DOTA and $[Mn(H_2O)_6]^{2+}$ solutions at 298 K. The lines represent the best-fit curves using the Solomon-Bloembergen-Morgan equations (see text).

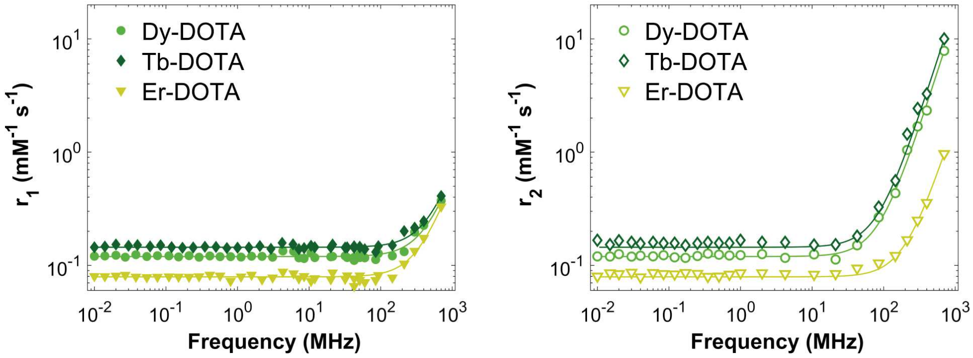

Figure 49: Longitudinal (left) and transverse (right) relaxivity ^{1}H NMRD profiles of Dy-DOTA, Tb-DOTA and Er-DOTA solutions at 298 K. The lines represent the best-fit curves using the Solomon-Bloembergen-Morgan equations (see text).

Table 5: Parameters obtained from the fitting of (A) $[Mn(H_2O)_6]^{2+}$ and (B) Gd-DOTA solutions NMRD profiles. Underscored parameters are those kept fixed in the least-square fitting procedure. The values in brackets represent the standard deviation of the fitted parameter. The fixed parameters values for the r_2 data analysis and obtained from the r_1 data fitting are labelled with the apical asterisk. The values of the parameters reported in italic were calculated through the relation $\tau_{S0}^{-1} = (1/5)\,[4S(S+1)-3]\Delta^2\tau_v$ and their standard deviations, if any, were obtained by the propagation of uncertainties.

Complex	**A. $[Mn(H_2O)_6]^{2+}$**			**B. Gd-DOTA**		
Parameters	**r_1**	**r_2**	Ref. [119] / [120, 121] / [122]	**r_1**	**r_2**	Ref. [123]
q	$\underline{6}$	$\underline{6}$	6/6/6	$\underline{1}$	$\underline{1}$	1
r / Å	2.89(0.04)	2.89*	2.83/2.78/2.71(0.03)	3.07(0.05)	3.05(0.07)	3.1
τ_r / ps	38.6(2.9)	38.6*	30.0(0.2)/32/32(2)	78.1(8.5)	81.5(12.8)	77(4)
τ_m / ns	$\underline{35.5}$	37.3(0.7)	35.5(4.0)/ – /20	$\underline{244}$	$\underline{244}$	244(11)
$A/\hbar$ / Mrad s^{-1}	5.37(0.08)	5.37*	5.43(0.03)/4.27/5.1(0.5)	–	–	–
τ_{S0} / ps	2267(42)	2267*	–/3500/3500	486.7(47.8)	445.8(58.2)	*473(52)*
τ_v / ps	0.5(0.5)	4.34(0.10)	10(10)/2 – 3/5.3	$\underline{11}$	$\underline{11}$	11(1)
Δ^2 / 10^{19} s^{-2}	–	1.59(0.05)	0.06(0.06)/*1.5 – 2.2/0.84*	*1.56(0.16)*	*1.70(0.26)*	1.6(0.1)
d / Å	$\underline{3.6}$	$\underline{3.6}$	3.6/ – /–	$\underline{3.5}$[1]	$\underline{3.5}$	3.5
D / 10^{-9} m^2 s^{-1}	$\underline{2.3}$	$\underline{2.3}$	2.3/ – /–	$\underline{2.3}$	$\underline{2.3}$	2.2

Table 6: Parameters obtained from the fitting of (A) Dy-DOTA, (B) Tb-DOTA and (C) Er-DOTA solutions NMRD profiles and from the analysis of the 400 and 700 MHz NMR ^1H spectra as explained in the text. Underscored parameters are those kept fixed in the least-square fitting procedure. The values in brackets represent the standard deviation of the fitted parameter. The values fixed for the r_2 data analysis and obtained from the r_1 data fitting procedures are labelled with the apical asterisk.

Complex	**A. Dy-DOTA**		**B. Tb-DOTA**		**C. Er-DOTA**	
Parameters	**r_1**	**r_2**	**r_1**	**r_2**	**r_1**	**r_2**
r / Å	3.37(0.05) [2]	3.37*	2.96(0.05)	2.96*	3.02(0.05)	3.02*
τ_{S0} / ps	0.19(0.01)	0.19*	0.22(0.01)	0.22*	0.13(0.01)	0.13*
α / Mrad s^{-1} T^{-1}	-	0.31(0.01)	-	0.27(0.01)	-	0.21(0.01)
τ_m / ns	$\underline{10}$	15.39(0.05)	$\underline{10}$	26.39(0.07)	$\underline{10}$	1.40(0.03)
τ_m / ns (spectra)	-	16.91(1.15)	-	29.36(2.20)	-	4.84(0.34)

The NMRD profiles were fitted with the model functions described in Section 4.3 using a custom Matlab script (MathWorks, Natick, MA, USA). The proton longitudinal and transverse relaxivity experimental data and the fitting curves of the five samples are reported in Fig. 48 (*Case 1*, Gd-

---

[1] A more reasonable choice for this parameter (whose fixed value was taken from [123]) could be $d = 4$ Å, in agreement with the molecular radius length which is about $3.7 - 3.8$ Å (equatorial metal-proton distance of the macrocyclic ring). However the fit doesn't change appreciably and the variation of the estimated parameters is below 10% ($r = 3.01 \pm 0.05$ Å, $\tau_r = 80.5 \pm 8.1$ ps, $\tau_{S0} = 488.3 \pm 53.4$ ps).

[2] By imposing $r = 3$ Å, which is closer to the value of the Ln-O_w distance estimated with many different studies (such as Density Functional Theory, diffractometric and pulsed EPR) and is also more similar to the values obtained for Tb- and Er-DOTA, the variations of the other parameters retrieved from the fits are lower than 5% ($\tau_{S0} = 0.20 \pm 0.01$ ps, $\tau_m = 15.24 \pm 0.05$ ns).

DOTA and $[Mn(H_2O)_6]^{2+}$) and in Fig. 49 (*Case* 2, Dy-DOTA, Tb-DOTA, and Er-DOTA). The parameters of each fit are reported in Table 5 (*Case* 1) and Table 6 (*Case* 2).
Here below the obtained results are separately discussed.

Case 1 - $[\mathrm{Mn(H_2O)_6}]^{2+}$

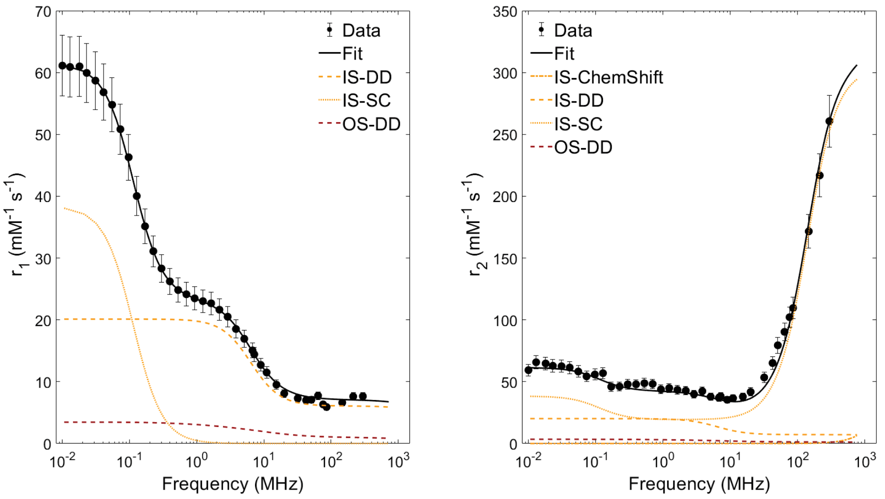

Figure 50: Longitudinal (left) and transverse (right) relaxivity ^1H NMRD profiles of $[Mn(H_2O)_6]^{2+}$ solutions at 298 K. The lines represent the best-fit curves using the Solomon-Bloembergen-Morgan equations (see text).

Experimental data for $[Mn(H_2O)_6]^{2+}$, Fig. 48, were fitted with Eq. 50 using the expressions reported in Eqs. 51 to 62 and the parameters in Table 5.A. In this table we also indicate fixed and adjustable parameters employed for the least-square fitting procedure. The fixed parameters were taken from [119]. The different contributions to the relaxivities described in Section 4.3 are shown in Fig. 50.
From the fitting of r_1 data we estimated r, τ_r, $A/\hbar$, τ_{S0}, and τ_v. The obtained values were thus fixed for the analysis of r_2, from which the values of τ_m and of the ZFS parameter τ_v were extracted. For the sake of clarity, it should be noticed that the fit of r_1 resulted insensitive to values of $\tau_m > 1$ ns, since the conditions $T_{1m} \gg \tau_m$ and $\tau_r \ll \tau_m$ hold. As τ_v and τ_{S0} were thus estimated, it was possible to calculate the mean squared fluctuations of the ZFS parameter Δ^2. It is worth remarking that the estimation of τ_v obtained from the fitting of r_1 data suffers of a great uncertainty, in analogy with the results of the work of Gomez *et al.* in 2014 [119]. Indeed, ZFS parameters can be hardly retrieved by NMR acquisitions only [123, 124], mainly if limited to the longitudinal relaxivity NMRD profile alone [15].
The increase of the transverse relaxivity at frequency $\nu > 20$ MHz is prin-

cipally due to the scalar SC contribution, which is a non-negligible mechanism differently from the situation of the other DOTA complexes here investigated. The pseudocontact contribution to $\Delta\omega_m$ was neglected.
It is important to remark that, by extending the data acquisition to the low frequency regime and combining the analysis of r_1 and r_2 NMRD profiles, we were able to directly obtain an estimation of τ_m, which is usually determined through ^{17}O NMRD profile analysis [119, 123–125], and a more accurate evaluation of τ_v and Δ^2 [105, 119, 120, 122].
As reported in Table IIA, a good agreement of all the estimated parameters with the literature ones was found ($r = 2.89 \pm 0.04$ Å, $\tau_r = 38.6 \pm 2.9$ ps, and $\tau_{S0} = 2267 \pm 42$ ps) [119–122].

Case 1 - Gd-DOTA

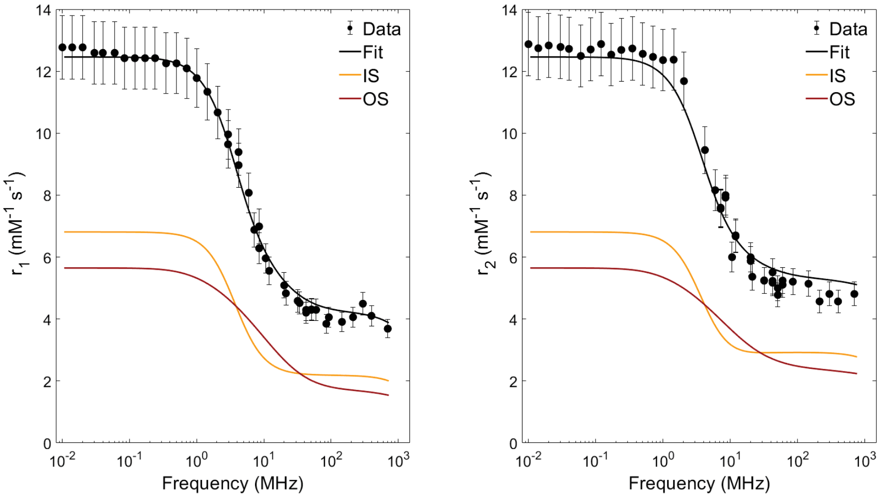

Figure 51: Longitudinal (left) and transverse (right) relaxivity ^{1}H NMRD profiles of Gd-DOTA solutions at 298 K. The lines represent the best-fit curves using the Solomon-Bloembergen-Morgan equations (see text).

The data of Gd-DOTA, Fig. 48, were fitted with Eq. 50 using the expressions reported in Eqs. 51 to 62 and the parameters in Table 5.B (even in this case, fixed and adjustable parameters are highlighted). The fixed parameters were taken from [123]. The contributions to the relaxivities described in Section 4.3 are reported in Fig. 51.
As in previous works [123, 126], the scalar contributions (Eqs. 55 and 57) to the relaxivities were neglected in the present case. Indeed, the dispersions of relaxivity data due to the scalar term and the related high-field increase of r_2 are absent (see $[Mn(H_2O)_6]^{2+}$ data for comparison, Fig. 50).
For the fitting of r_1 data we employed r, τ_r, τ_{S0}, and τ_v as adjustable parameters. Analogously to $[Mn(H_2O)_6]^{2+}$, the estimation of τ_v from the fitting of

the longitudinal NMRD profile was affected by a considerable uncertainty ($\sim 100\%$). Therefore, we decided to fix τ_v to the literature value $\tau_v = 11$ ps [123].

For r_2 fitting, as the scalar contribution can be neglected ($A/\hbar$ must be lower than 0.1 Mrad s^{-1} for a correct fitting of both r_1 and r_2 data), Eq. 52 reduces to $(1/T_2)^{IS} = fq/(T_{2m} + \tau_m)$. This relation has the same form of Eq. 51, since the chemical shift $\Delta\omega_m$ induced on water protons for Gd(III) complexes is due to a pure contact contribution [22]. No further information could therefore be extracted from r_2 data because of the insensitivity to τ_m when the conditions $T_{2m} \gg \tau_m$ and $\tau_r \ll \tau_m$ hold. In this way, we set as adjustable parameters the same ones used for r_1 fitting, *i.e.* r, τ_r, τ_{S0}, and τ_v. Again, we found a significant uncertainty in estimating the value of τ_v, that was therefore fixed to the literature value as done for the r_1 fitting.

Nevertheless, from both the analysis of longitudinal and transverse relaxivity NMRD profiles we obtained values in good agreement with the literature [123, 126].

Case 2 - Dy-DOTA, Tb-DOTA and Er-DOTA

The data obtained for Dy-, Tb-, and Er-DOTA complexes, Fig. 49, were fitted with Eq. 50 using the expressions reported in Eqs. 51 to 57, where g is substituted by g_j and S by J, and Eqs. 63 to 70 and the parameters in Table 6. The contributions to the relaxivities described in Section 4.3 are highlighted in Figs. 52 to 54.

We fixed $\tau_r = 80$ ps [127], $d = 3.5$ Å (the same value adopted for Gd-DOTA)[3]), $D = 2.3 \times 10^9$ m^2 s^{-1} [22], and we hypothesized the electronic relaxation times independent from the applied magnetic field, hence $\tau_{S0} = T_{1e} = T_{2e}$ [22, 101]. Moreover, we estimated the ratio between $\Delta\omega_m$ and the applied magnetic field ($\alpha = \Delta\omega_m/B_0$) from the spectra acquired at 400 and 700 MHz (Fig. 55). Extrapolation of $\Delta\omega_m$ was accomplished by measuring the paramagnetic chemical shift $\Delta\omega_p$, that is the shift of the water signal from the diamagnetic position, given by

$$\Delta\omega_p = fq\frac{\Delta\omega_m}{(1 + \frac{\tau_m}{T_{2m}})^2 + \tau_m^2\Delta\omega_m^2} \tag{71}$$

Eq. 71 reduces to $\Delta\omega_p = fq\Delta\omega_m$ if $\tau_m^2\Delta\omega_m^2 \ll 1$ and $\tau_m/T_{2m} \ll 1$, *i.e.* when $(T_2^{-1})^{IS}$ is proportional to the square of the magnetic field (at high fields) [21]. This behaviour can be well appreciated in Fig. 49 (right) for each sample at frequency $\nu > 20$ MHz.

---

[3] As in the case of Gd-DOTA, by setting this parameter to the more reasonable $d = 4$ Å (see the footnote relative to Table 5), we obtain no substantial changes in the fits (Dy-DOTA: $r = 3.2 \pm 0.05$ Å, $\tau_{S0} = 0.24 \pm 0.01$ ps, $\tau_m = 15.51 \pm 0.05$ ps; Tb-DOTA: $r = 2.90 \pm 0.05$ Å, $\tau_{S0} = 0.27 \pm 0.01$ ps, $\tau_m = 26.5 \pm 0.07$ ps; Er-DOTA: $r = 2.96 \pm 0.05$ Å, $\tau_{S0} = 0.16 \pm 0.01$ ps, $\tau_m = 1.57 \pm 0.03$ ps).

For the three different samples, we obtained r and τ_{S0} from r_1 data fitting, while we extracted the parameter τ_m from the analysis of r_2 data (see Table 6).

Observing Fig. 49, some considerations can follow. Er-DOTA showed systematically lower relaxivity values than Dy-DOTA and Tb-DOTA, the last one having the highest relaxivity values, over the whole measured range of frequency. The differences between the three complexes are evidenced in the high-field region of r_2 data. Indeed, since the three complexes have the same geometrical structure and similar τ_{S0}, τ_v, and α, such differences are mainly attributed to the different water-exchange time τ_m (an independent estimation of τ_m was performed using Eq. 52 combined with the expression for $\Delta\omega_p$ in the limits of $\tau_m^2 \Delta\omega_m^2 \ll 1$ and $\tau_m / T_{2m} \ll 1$, neglecting the OS terms) [21]. More in details, for Er-DOTA we found $\tau_m = 1.40 \pm 0.03$ ns, *i.e.* one order of magnitude lower than those of Dy-DOTA and Tb-DOTA, for which $\tau_m = 15.39 \pm 0.05$ ns (slightly higher than those previously published $\tau_m = 9$ ns, [21]) and $\tau_m = 26.39 \pm 0.07$ ns, respectively (see Table 6). Now, it should be reminded that the electronic distribution of the 4f electrons is different for the three lanthanide ions, being oblate for Dy(III) and Tb(III), and prolate for Er(III), see Fig. 46 [25]. Thus, a possible explanation for the lower value of τ_m of Er-DOTA could be found in the different magnetic anisotropies of these complexes, due to their different electronic distributions [128]. In fact, Dy-DOTA and Tb-DOTA complexes are characterized by an easy-plane magnetic anisotropy, *i.e.* perpendicular to the Ln-O$_\mathrm{W}$ bond (O$_\mathrm{W}$ is the oxygen of the coordinated water molecule, which resides at the top of the oxygen plane of the capped square antiprism structure of Ln-DOTA). On the other hand, Er-DOTA is characterized by an easy-axis magnetic anisotropy almost parallel to the Ln-O$_\mathrm{W}$ bond, as illustrated in Fig. 47 in Section 4.2 [114, 128–130]. It is also known in the literature that these complexes exist in solution as mixtures of isomers with different coordination geometry: monocapped square antiprismatic (SAP) and monocapped twisted square antiprismatic (TSAP). It has been shown that the TSAP isomer exhibits a coordinated water exchange rate, $k_{ex} = 1/\tau_m$, much higher than that of the SAP species [131] (*i.e.* the TSAP isomer has a lower τ_m). Furthermore, for the elements that follow Dy the TSAP isomer loses the coordination water so that, in the specific case of ErDOTA, there are two species in solution which differ in the state of hydration [132]. Of course, the species with $q = 0$ influences the relaxation of the solvent only with the OS mechanism. Hence, the "effective" τ_m that we extrapolate reflects also the relative populations of the two species as they change across the Ln series.

The values obtained for the distances between the lanthanide paramagnetic center and the coordinated water proton are lower than those recently estimated for solid-state Ln-DOTA complexes ($r = 3.4$ Å, [106]) but compa-

rable to the geometrical distance assumed for similar complexes (*e.g.* for Dy-DTPA, Vander Elst *et al.* [22] assumed $r = 3.1$ Å).
Considering Dy-DOTA, we found $\tau_{S0} = 0.19 \pm 0.01$ ps from measurements at 298 K, which is smaller than the value reported in the literature for Dy(III) aqua ion ($\tau_{S0} = 0.39$ ps at 298 K, [101]) and for Dy-DOTA water solutions at 310 K ($\tau_{S0} = 0.33$ ps, [133, 134]). Similarly, we found $\tau_{S0} = 0.13 \pm 0.01$ ps (at 298 K) for Er-DOTA that is smaller than the value reported in the literature for Er(III) aqua ion ($\tau_{S0} = 0.31$ ps at 298 K, [101]). No literature data for τ_{S0} were found for Tb-DOTA, but Harris *et al.* determined $\tau_{S0} = 0.25$ ps for the complex Tb-DTPA-BC$_{12/14}$ PhenA [99], which is very close to the value that we have reported ($\tau_{S0} = 0.22$ ps). As can be seen in detail in Figs. 52 to 54 the Curie interaction (dashed lines) is the main responsible for the high-field increase of longitudinal relaxivities observed experimentally, that cannot be described in terms of the dipolar interaction alone (dotted lines).

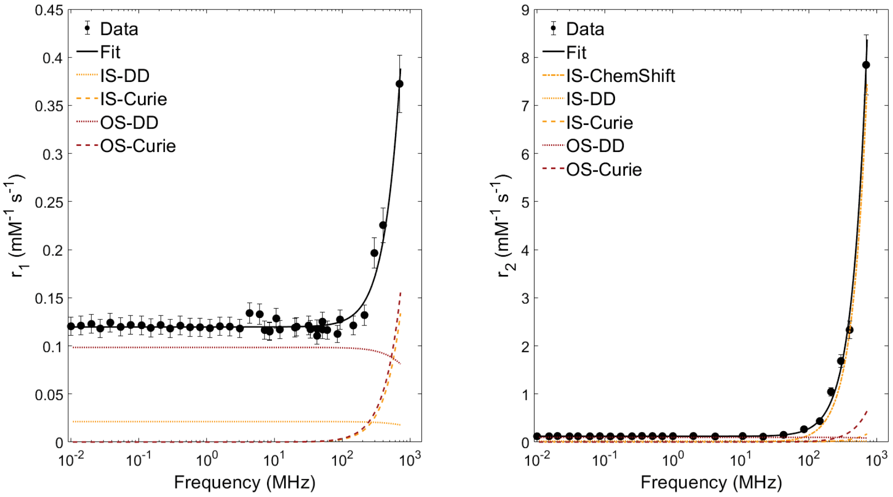

Figure 52: Longitudinal (left) and transverse (right) relaxivity ^{1}H NMRD profiles of Dy-DOTA solutions at 298 K. The lines represent the best-fit curves using the Solomon-Bloembergen-Morgan equations (see text).

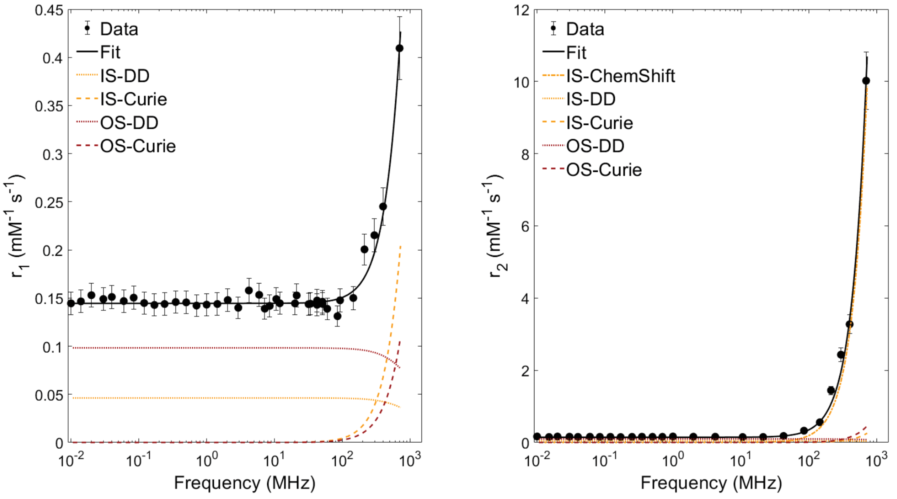

Figure 53: Longitudinal (left) and transverse (right) relaxivity ^{1}H NMRD profiles of Tb-DOTA solutions at 298 K. The lines represent the best-fit curves using the Solomon-Bloembergen-Morgan equations (see text).

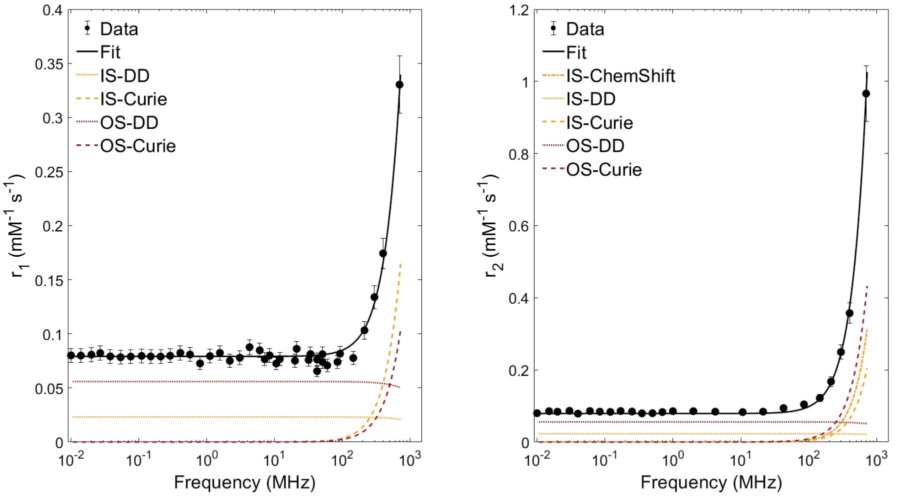

Figure 54: Longitudinal (left) and transverse (right) relaxivity ^{1}H NMRD profiles of Er-DOTA solutions at 298 K. The lines represent the best-fit curves using the Solomon-Bloembergen-Morgan equations (see text).

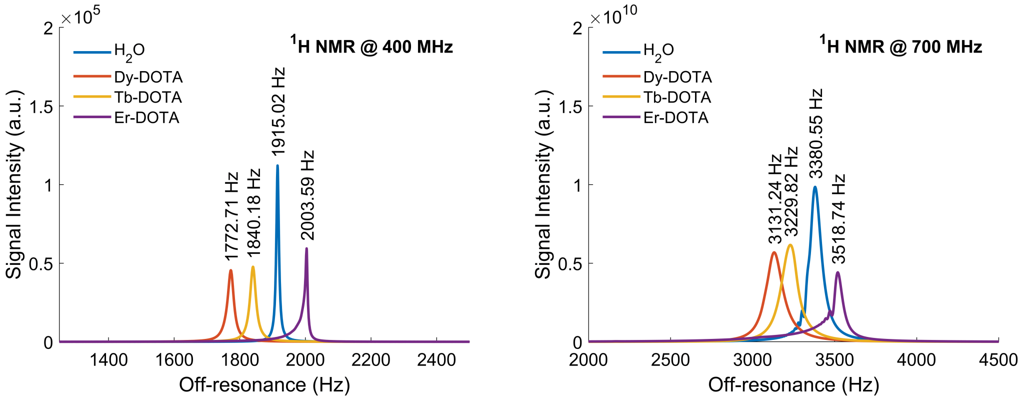

Figure 55: ^{1}H NMR spectra collected at 400 MHz (left) and at 700 MHz (right) of the aqueous solutions of Dy-DOTA, Tb-DOTA, Er-DOTA, and pure water. A small amount of TSP locking agent was added to the samples.

MRI Images

The images of the water solution sample of Dy-DOTA, Tb-DOTA and Er-DOTA with same concentration (5 mM) acquired at 0.18 T are reported in Fig. 56 (left), while Fig. 57 (left) shows the MRI acquisitions at 7 T.
Circular ROIs (Regions of Interest) were used to measure the variation of the signal intensity of the vials represented in the images along each series: the graphs on the right in Figs. 56 and 57 illustrate the evolution of the normalized signal intensity as a function of the acquisition parameters T_R or T_E. We found that Tb-DOTA shows the highest enhancement of the relaxation rate, in good agreement with the NMR relaxivity curves (see top curves on the right side of the graphs reported in Fig. 56.A and Fig. 57.A and bottom curves in Fig. 56.B and Fig. 57.B). On the counter hand, Er-DOTA displays the lowest enhancement, as shown in Fig. 56.A and Fig. 57.A (bottom curves in the right-sided graphs), and in Fig. 56.B and Fig. 57.B (top curves). It can be also appreciated the contrast enhancement, according to the NMRD profiles, for all three complexes at high field (7 T, Fig. 57) if compared to low field acquisitions (0.18 T, Fig. 56), especially for the series with variable T_E, when comparing the relative increment (varying T_R) or decrement (varying T_E) of the signal. Being equal the T_R/T_E variations at both fields, the discrepancies between the relative signal intensities are wider along the series at 7 T with respect to those at 0.18 T, indicating shorter relaxation times and, therefore, higher relaxivities.
Thanks to the high-field increment of the transverse relaxivities, Dy-DOTA, Tb-DOTA, and, to a lesser extent, Er-DOTA could be employed as negative MRI contrast agents at high field. On the other hand, their longitudinal relaxivities are too low for applications as positive contrast agents, despite

the high-field growth caused by the Curie interaction.
Further investigations are needed to assess potential pitfalls in terms of biocompatibility and side-effects of these Ln-based complexes for in-vivo applications.

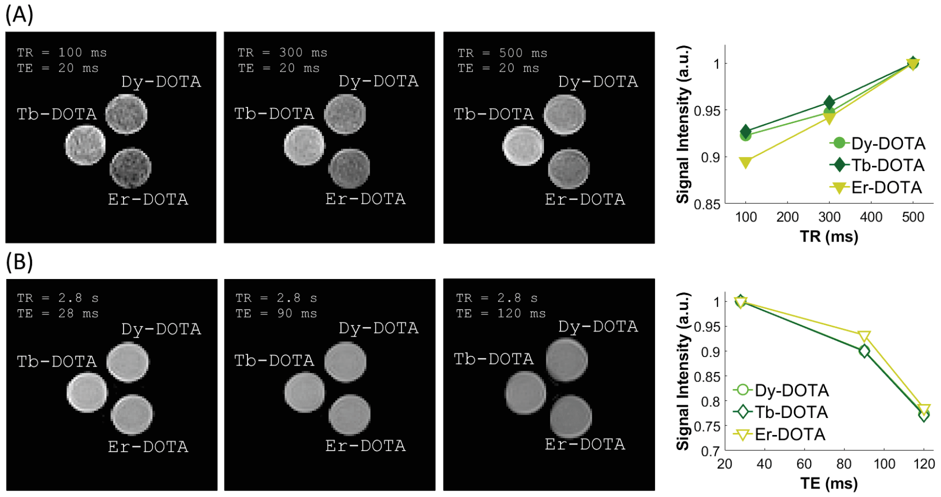

Figure 56: Spin-Echo images of vials containing 5 mM of Dy-DOTA, Tb-DOTA and Er-DOTA (A) at different repetition times and (B) at different echo times. The graphs nearby the images show the evolution of the normalized signal intensity measured in circular ROI for each sample along each series.

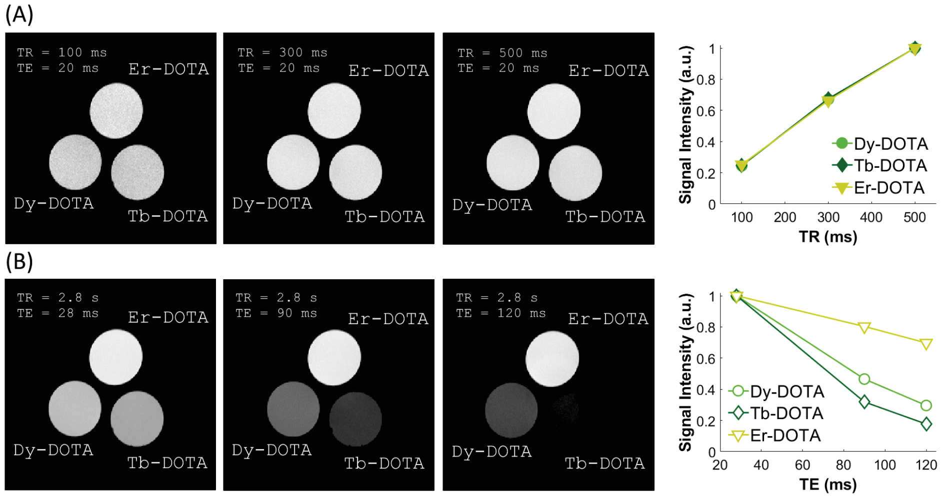

Figure 57: Spin-Echo images of vials containing 5 mM of Dy-DOTA, Tb-DOTA and Er-DOTA (A) at different repetition times and (B) at different echo times. The graphs nearby the images show the evolution of the normalized signal intensity measured in circular ROI for each sample along each series.

4.6 CONCLUSIONS

The present work provides further evidence of the deep information that could derive from a combined analysis, not usually performed, of both longitudinal and transverse relaxivities NMRD profiles collected in a wide range of frequencies for the structural, dynamic, and magnetic properties of MRI contrast agents. For the $[Mn(H_2O)_6]^{2+}$ aqua ion we were able to assess the water exchange time τ_m directly from the analysis of the NMRD profiles and to give a more accurate estimation of the ZFS parameters, namely τ_v and Δ^2. It must be mentioned that such result was obtained without employing other techniques but NMR. Conversely, the fit of r_2 profile of Gd-DOTA sample did not provide any additional information if compared to r_1 fitting, but it confirmed (i) the suitability of the SBM model in a wide range of frequencies also for the transverse relaxivity NMRD profiles, often not measured, and (ii) the negligibility of the scalar interaction for the Gd(III) complex. In addition, the analysis of Dy-DOTA, Tb-DOTA, and Er-DOTA NMRD profiles allowed the estimation of the metal-proton distance r, the electronic relaxation time τ_{S0}, and the water exchange time τ_m. We hypothesize that the latter might be correlated to the different magnetic anisotropy of the complexes, easy-plane for Dy-DOTA and Tb-DOTA, and easy-axis for Er-DOTA. Finally, the possible high-field application as negative MRI CAs for Dy-DOTA, Tb-DOTA, and Er-DOTA complexes was supported by spin-echo images acquired at 7 T. This result could be useful for future high-field clinical imagers and for currently available preclinical MRI scanners.

CONCLUSIONS AND PERSPECTIVES

In this PhD thesis, the applications of relaxation time measurements for clinical purposes and contrast agent (CA) characterization are investigated. In particular, two main research topics have been developed: the first one concerns the open issue of Magnetic Resonance Imaging (MRI) relaxation time mapping harmonization while the second one aims at understanding the relaxation enhancement mechanism of some negative CAs for high-field applications from a more fundamental point of view.

As far as concerns the issue of data harmonization for relaxation time mapping techniques, we developed a robust method based on a reference 'belt phantom' composed of vials filled with $MnCl_2$ aqueous solutions. The phantom can be used as an in-scan reference for the evaluation of both precision and accuracy of the T_1 and T_2 maps since its design allows it to be wrapped around the anatomical region of interest to be mapped (in a cartridge-like arrangement). The main advantage of this method relies on the meticulous characterization of the phantom through *super partes* Nuclear Magnetic Resonance (NMR) techniques: the phantom's relaxation times dependence from both $MnCl_2$ concentration and temperature was indeed determined thanks to our NMR laboratory instrumentation. By measuring the temperature of the phantom, which can be inserted in a thermal-insulator envelope, at the moment of the acquisition by using an optical fibers sensor, we were able to determine exactly the real relaxation times of each vial, thanks to the NMR characterization: in fact, the relaxation times were found to increase linearly with temperature (in a small range around the room temperature, $17°C < T < 29°C$), while a linear dependence with $MnCl_2$ concentration was observed for the relaxation rates ($R_i = 1/T_i$ with $i = 1, 2$). Such behaviors are in agreement with the expected ones from the Solomon-Bloembergen-Morgan theory. Three main experiments were conducted:

- **Exp. 1**: Firstly, the method was applied on three types of mapping sequences (standard IR and SE, turbo IR and SE, MOLLI and T_2-prep TrueFISP) by scanning the belt phantom alone. Two different 1.5 T MRI scanners were used: a Siemens Magnetom Aera and a General

Electric Signa (both located at the Niguarda Hospital in Milan). We found good agreement between the reference NMR relaxation times values and the ones measured on the maps from standard and turbo MRI sequences, while significant discrepancies were found for T_1 and T_2 values from MOLLI (underestimated) and T_2-prep TrueFISP (overestimated) sequences respectively. In particular for the T_2-prep TrueFISP case, differently from the MOLLI one, the theoretical expected linear dependence of the relaxation rates as a function of $MnCl_2$ concentration was lost.

- **Exp. 2**: In the second experiment we applied the method to a phantom study, wrapping the 'belt phantom' around a Eurospin phantom, which is a device commonly employed for Quality Assurance controls and is composed of vials filled with Gd-doped agarose gels. We employed MOLLI and T_2-prep TrueFISP acquisitions with the Siemens Magnetom Aera scanner. We also considered the influence of the heart-rate on the mapped relaxation times (30 bpm $< HR <$ 150 bpm) finding the major effects on the T_2 maps, particularly remarkable for the highest T_2s. Considering the 'belt phantom', the experiment confirmed the results of Exp. 1. We also tested the recalibration of the maps using the 'belt phantom' as reference: we were able to overcome the 10% of underestimation of Eurospin's T_1s, while, since Eurospin's T_2 values resulted already underestimated (and being the 'belt phantom' ones overestimated), we had to conclude that for T_2-prep TrueFISP maps a recalibration using the reference 'belt phantom' is not applicable.
- **Exp. 3**: T_1 MOLLI and T_2 T_2-prep TrueFISP maps were acquired in the third experiment conducted *in vivo* on an untrained volunteer. Results confirmed what was found in the previous experiments and pointed out further limitations of the method if applied to the T_2-prep TrueFISP maps.

A software, named 'swSD', has been developed and validated for an independent evaluation of the relaxation time maps and for the generation of the Standard Deviation (SD) maps, in which, to each pixel, is assigned the 68% confidence bound of the fitted relaxation time value represented in the corresponding pixel on the relaxation time map. This piece of information is usually not considered in the analysis of the maps but we demonstrated that especially for fast mapping sequences the uncertainties derived from the pixel-wise fitting procedure are not negligible.

The presented method allows evaluating the performances in terms of both precision and accuracy for the MRI mapping sequences commonly used in clinical practice. Moreover, the advantage of an in-scan reference together with the joint analysis of T_1 and T_2 maps with their respective

SD maps could become a powerful instrument for the recalibration, where applicable, of the relaxation time maps, paving the way for intra- and inter-center data harmonization.

Future developments on this research topic will be carried out in a clinical trial in which will be further tested the *in vivo* feasibility of the method for several clinical mapping sequences and will be also considered possible surface effects, B_0/B_1/susceptibility issues, FOV increment, patient discomfort, temperature stability, etc. In fact, the author has been currently enrolled in the Specialization School of Medical Physics of the University of Milan with an activated traineeship at the ASST Grande Ospedale Metropolitano Niguarda (Milan).

In the second research project, we investigated the physical properties of some CAs by characterizing them through the analysis of the Nuclear Magnetic Relaxation Dispersion (NMRD) profiles, *i.e.* the magnetic field dependence of the longitudinal and transverse relaxation rates normalized to 1 mM concentration of the CA. The rationale of this topic was to understand the Paramagnetic Relaxation Enhancement (PRE) of potential negative CAs, which are composed of a paramagnetic lanthanide non-Gd center complexed with a macrocyclic molecule, for high-field applications, by taking advantage of the quadratic dependence of their transverse relaxation rate with the chemical shift. This latter, that justifies the exploitation of such compounds mainly as NMR shift agents for spectroscopic applications, is indeed proportional to the applied external magnetic field.
We acquired the longitudinal and transverse NMRD profiles by collecting relaxivity data in a wide range of Larmor resonance frequency (10 kHz $< \nu <$ 700 MHz) of 3 different Ln(III)-DOTA compounds (with Ln = Dy, Tb, and Er; DOTA = 1,4,7,10 - tetraazacyclododecane - N,N′,N″,N‴ - tetraacetic acid) in aqueous solutions at 298 K. For comparison, we also collected the NMRD profiles of the well-known Gd(III)-DOTA and of Mn(II) aqua ions. We employed standard NMR techniques (IR, SR, and CPMG) for relaxation times measurements above 7.2 MHz, while below 7.2 MHz we used the Fast-Field-Cycling (FFC) techniques (SR, CPMG, and SE). The data were analyzed by means of models derived from the Solomon-Bloembergen-Morgan theory (SBM), considering both the quenched $L = 0$ (Gd(III) and Mn(II)) or unquenched $L \neq 0$ (Dy(III), Tb(III) and Er(III)) orbital angular momentum, and the presence of the so-called Curie relaxation.

Through the joint analysis of longitudinal and transverse relaxivity data we were able to obtain:

- **Mn(II) aqua ions**: a direct estimation of the water-exchange correlation time τ_m and the Zero-Field-Splitting (ZFS) parameters (*i.e.* the ZFS modulation correlation time τ_v and the ZFS mean squared fluctuation Δ^2);

- **Gd-DOTA**: a confirm of the reliability of the SBM theory in describing both the longitudinal and transverse NMRD profiles (being the second one often neglected for the characterization of CAs);
- **Dy-, Tb- and Er-DOTA**: an estimation of the metal-proton distance r, the low-field electronic relaxation time τ_{S0} and the water-exchange correlation time τ_m for each complex.

The lower relaxivity at high-fields of Er-DOTA with respect to Dy- and Tb-DOTA ones, mainly due to τ_m, was put in relation with the different magnetic anisotropies of the complexes (easy-plane for Dy- and Tb-DOTA, and easy-plane for Er-DOTA). Moreover, it was observed that Dy- and Tb-derivatives present transverse relaxivity at 7 T (~ 2 mM^{-1} s^{-1}) close to the Gd- one at clinical magnetic fields $1.5 - 3$ T (~ 6 mM^{-1} s^{-1}).
The efficiency of Dy-, Tb-, and Er-DOTA at high fields as both positive and negative magnetic resonance imaging CAs has been ascertained by contrast images collected at 7 T employing a pre-clinical MRI scanner.

As to the future perspectives on this research topic, further studies performed both *in vitro* and *in vivo* are needed in order to evaluate the biological toxicity, the contrast efficiency in biological medium and at biological temperature, as well as the effect of others influencing factors (*e.g.* pH).

A LOW FIELD MAPPING SEQUENCES DEVELOPMENT

The subjects presented in this Appendix were developed by the candidate during a 4 months mobility project in Basel (Switzerland) at the Center for Adaptable MRI Technology (AMT) affiliated with the Department of Biomedical Engineering of the University of Basel (Switzerland).

A.1 RATIONALE

Low field approaches are gaining momentum for more accessible MRI-based diagnoses: in fact, the handle of this type of technology is much easier (*e.g.* no cryogenic elements, such as liquid helium, are needed for the functioning of the scanners), not to mention the lower costs for the installation, the use and the maintenance of such devices [135]. Quantitative relaxometry is a critical step towards comparable metrics in MRI [5], despite being regrettably often set aside due to impractical acquisition times. Remarkably, low field relaxometry could be particularly compelling, benefitting from higher dispersion and potentially unveiling new contrasts [136]. With a further decreased sensitivity though, it becomes crucial to explore fast approaches for precise and accurate mapping of nuclei relaxation rates.

A.2 T_1- AND T_2-PREP SSFP

The presented work reports on the use of magnetization prepared Steady-State Free Precession (SSFP) sequences tuned for fast T_1 and T_2 mapping at low field.

The realized sequences were based on the sequence developed by Huang *et al.* [38] for the T_2 mapping in cardiac applications.

Custom T_1- and T_2-prepared SSFP sequences were developed with the software PRim (RS2D, France) and consist of three main blocks (see Fig. 58):

1. T_1-or-T_2 magnetization preparation
2. Transient-state stabilization
3. Transient state SSFP readout with customized k-space centric ordering in 2D (projection)

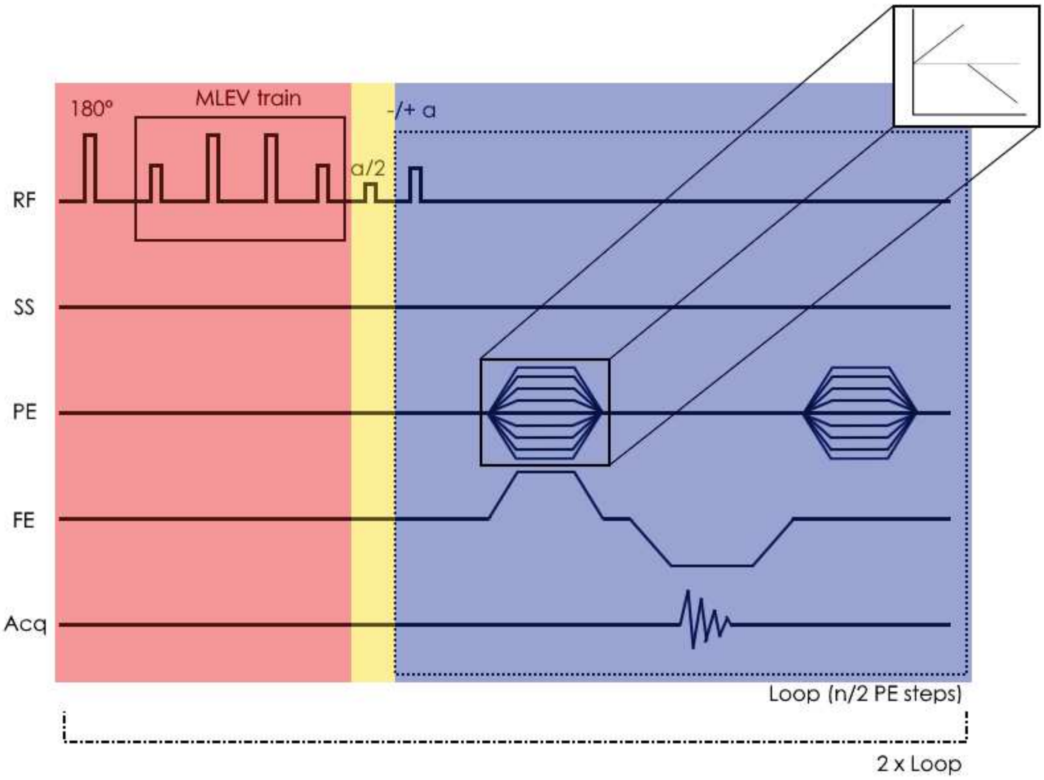

Figure 58: T_1- and T_2-prepared SSFP sequence acquisition scheme. The three blocks composing the sequences are highlighted in different colors: T_1-or-T_2 magnetization preparation pulses (red), the transient state stabilization pulse (yellow), and the SSFP readout (blue). The T_2-prep SSFP sequence is devoid of the initial inversion pulse. In the top right corner is reported the phase-encoding Fourier readout scheme.

Many variations were performed to the Huang's original sequence schemes, in order to optimize them both in terms of SNR and artifacts:

- The T_2 magnetization preparation block was based on a Malcolm-Levit (MLEV) train of two, instead of four, refocusing rf pulses (π_x and π_{-x}) between an excitation $(\pi/2)_x$ and a tip-up $(\pi/2)_{-x}$ pulses. The T_2 weighting is obtained by varying the time window of this train of pulses ($T_{E,prep}$). The T_1 magnetization preparation block was obtained by adding a π_x pulse before the minimum length T_2 preparation block. The T_1 weighting is obtained by varying the time between the inversion pulse and the shortest T_2 preparation block (T_I). All pulses were hard pulses.

- No spoiling gradients were used.

- A preparatory (-$\alpha/2$)-($T_R/2$) pulse followed by only one dummy pulse was applied to stabilize the initial oscillation of the transient state. Using more than one dummy pulse implied the necessity of more averages because of the decrement of the SNR.

- A full Fourier readout scheme with linear phase encoding was selected: data were first sampled close to the center of *k*-space and then ramped linearly to the outer *k*-space. This operation was divided in two parts (see Fig. 58). By starting the signal readout close to the center of the *k*-space, image contrast could be kept close to the initial T_1 or T_2-prepared magnetization level.

- Unfortunately, some problems arose concerning the full balancing of the readout gradients: not perfect balancing due to the hardware chain gave birth to artifacts (*e.g.* blurring) that severely affected the image reconstruction. For that reason, an unbalanced readout scheme was preferred for the acquisitions.

- No slice section gradients were used, resulting in 2D projection image acquisitions.

- The flip angle α set in the SSFP readout ($FA = 40°$) was selected in order to reduce the artifacts arising from the fact that the central *k*-space line (the ones that mostly provides amplitude information) was sampled first: the decay of the signal occurring while moving to the steady-state produced a *k*-space in which the central line had an exponential higher intensity with respect to the other lines, creating stripes in the PE direction. With a smaller flip angle, this effect was mitigated.

- The T_R of the readout was kept as short as possible ($T_R = 10.2$ ms) setting properly the spectral bandwidth (not too long for a good SNR, not too short for a reasonable FOV) and leaving sufficient time for the proper setting of the gradients by the hardware (gradient ramp time and gradient duration not too short, each > 600 µs).

The acquisitions were performed with a resistive biplanar 0.1 T MRI system (Bouhnik SAS, France, Fig. 59.A) and tested on an MRI phantom composed of nine vials filled with different [$MnCl_2$] solutions, thus spanning a wide range of T_1s and T_2s. Ground-truth relaxation times were measured at room temperature using standard spectroscopic sequences (IR and CPMG). Validation of both magnetization preparation block was assessed spectroscopically (FIDs only) for each sample.

Figure 59: (A) The resistive biplanar 0.1 T MRI system (Bouhnik S.A.S., France). (B) Disposition of the vials inside the bore of the transmitter/receiver coil.

It was possible to scan altogether nine samples in axial acquisitions with the disposition shown in Fig. 59.B. The acquisition parameters were as follows: $Acquisition\,Matrix = 64 \times 47$, $T_R/T_E = 5000/26$ ms, $FOV = 153 \times 154$ mm^2, and $NA = 5$. Ten images were acquired with different T_2-weighting ($T_{E,prep} = 2, 4, 10, 20, 35, 50, 70, 100, 150, 200$ ms) and ten images with different T_1-weighting ($T_I = 5, 25, 45, 80, 150, 250, 500, 1000, 2500, 5000$ ms). The total acquisition time was $\sim$ 10 minutes for each set of images. The acquired images were post-processed by performing a zero-filling to obtain a final matrix size of 128×128; an Hamming filter was also applied to every images.
A pixel-wise fit was performed for each series of T_1- or T_2-weighted images using a 3-parameters exponential recovery function for T_1 and a 2-parameters exponential decay function for T_2). The obtained relaxation maps are illustrated in Fig. 60 and the comparison of spectroscopic measurements with computed maps is reported in Fig. 61, with $R_1 = 1/T_1$ and $R_2 = 1/T_2$. As a reference, both the calibration curves from NMR spectroscopy (grey areas) and the values obtained from the validation of the magnetization preparation block are shown. A good correlation was found for high T_1 and T_2 values. Blurring artifacts (not shown) from intrinsic filtering of k-space and possible balancing issues critical in the approach to steady-state phase could explain the discrepancies observed at low T_1 and T_2 values. The sampling schemes of the recovery and decay curves could also affect the accuracy of the extracted maps, particularly over a broad range of relaxation rates. Introducing slice selection and adding un-

dersampling strategies are possible solutions to reduce both artifacts and acquisition times.

In conclusion, the proposed method returned very promising results both in terms of speed and accuracy for fast and reliable relaxometry of T_1 and T_2 at low field strength.

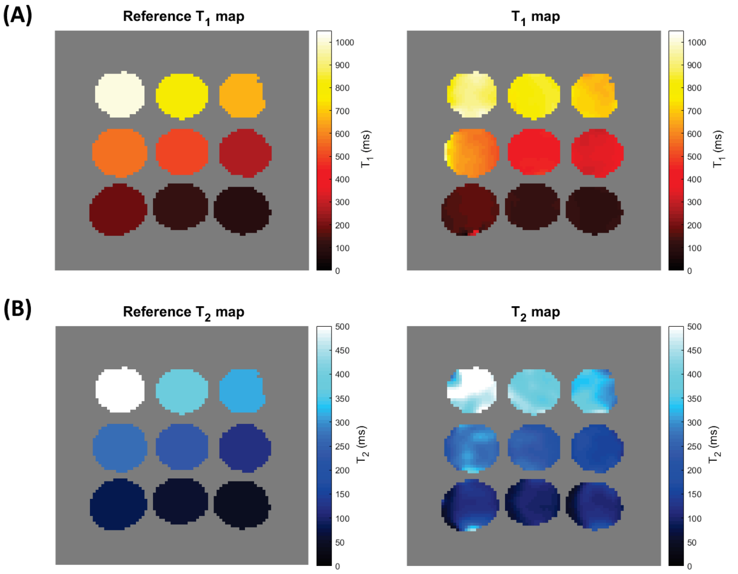

Figure 60: (A) NMR reference (left) and measured T_1 maps (right). Acquisition: 10 images with T_Is in the range $5-5000$ ms, $NA = 5$. (B)) NMR reference (left) and measured T_2 maps (right). Acquisition: 10 images with $T_{E,prep}$s in the range $2-200$ ms, $NA = 5$.

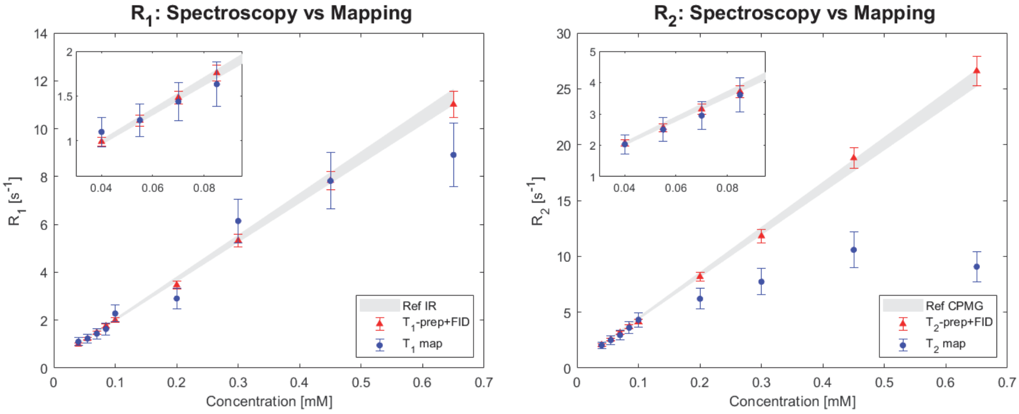

Figure 61: Relaxation rates R_1 (left) and R_2 (right) as function of [$MnCl_2$] for the different techniques used. An error of 15% is associated to all values obtained from the maps (3% for IR and CPMG results, 5% for T_1 and T_2 preparation+FID results).

A.3 SCHEDULE OPTIMIZATION FOR MRF

The interest on Magnetic Resonance Fingerprinting (MRF, [56]) has become increasingly larger in the last years since it is a method for the simultaneous generation of several parametric maps of interest (*e.g.* T_1, T_2, B_0, B_1, etc.) for clinical applications from a single and time-efficient acquisition. MRF could benefit from the higher dispersion of relaxation times at low field, that could translate in new contrasts and hence new diagnostic markers. In this study, the accuracy of parametric maps is explored at low field using an optimized approach for a model based, bSSFP (balanced Steady State Free Precession) sequence inspired from the MRF framework.

MAGNETIC RESONANCE FINGERPRINTING MRF relies on three main processes that can be summarized in:

- **Dictionary Optimization and Generation**: by means of Bloch equation simulations, the intensities of the signal during the acquisition is simulated for many combinations of a wide range of parameters of interest (T_1, T_2, B_0, B_1, etc...) taking into account the details of the acquisition sequence (FA, T_R, T_E, etc...). The collection of the signal evolution patterns is called *dictionary D*. The self-correlation matrix D^+D allows to understand the discrimination power of the dictionary: as suggested by Cohen *et al.* [137], an optimization of the acquisitions parameters can be performed in order to reach the condition of $D^+D = \mathbb{I}$ (perfect discrimination).
- **Data Acquisition**: once that the sequence parameters have been optimized and the dictionary has been created, the data can be acquired. Many different imaging sequences can be used (bSSF, EPI, etc..) but they must have been properly simulated. Usually MRF allows to acquire low SNR images speeding up the acquisition process.
- **Pattern Matching**: The last step of the MRF consists in finding the simulated data pattern (or *fingerprint*) closest as possible to the acquired one (this is a pixel-wise process). The influence of the SNR and the discrimination power of the dictionary play a fundamental role in this passage. Once the match has been found, it is possible to assign to the pixel with the matched fingerprint all the parameters used for the simulations, thus providing as many parametric maps as the number of parameters taken into account in the simulations.

Two series of twenty bSSFP projections ($Acquisition\,Matrix = 47 \times 47$, $FOV = 12 \times 12\ \text{cm}^2$, $NA = 4$, $Acquisition\,Time = 32$ min) were acquired of an MR phantom using a random and an optimized set of coupled FAs (range = $0 - 180°$) and T_Rs (range = $20 - 500$ ms), in a resistive biplanar 0.1 T MRI system (Bouhnik SAS, France). The scheme of the sequences, developed by means of the software PRim (RS2D, France) is reported in Fig. 62.

The phantom was composed of nine vials filled with different [$MnCl_2$] aqueous solutions, spanning a wide range of T_1s ($88 - 1016$ ms) and T_2s

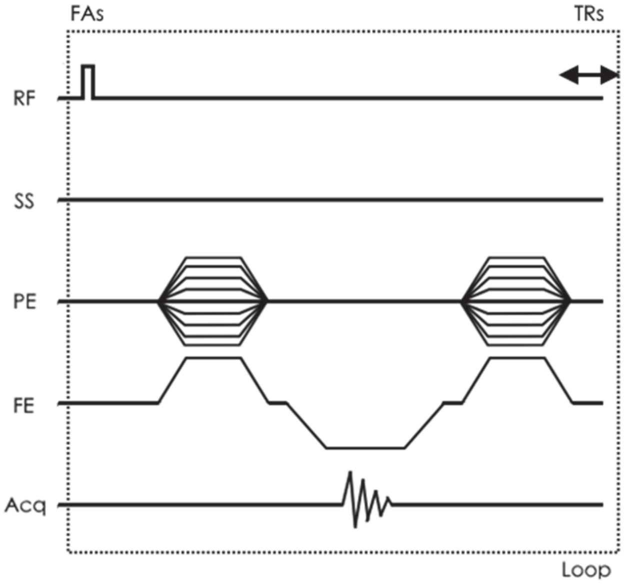

Figure 62: MRF sequence scheme: a full balanced SSFP able to acquire the same specific *k*-space line of all the images consecutively. Before moving to the next phase encoding step, a 5 s delay was set for the full recovery of the magnetization.

(38 – 486 ms). Ground-truth relaxation times were measured using standard spectroscopic sequences (IR and CPMG).

The MRF parameter optimization was performed by searching the set of FAs and T_Rs that minimize the difference between the self-correlation matrix $M = D^+D$ of the dictionary and the identity matrix $\mathbb{I}$ (*i.e.* the condition of perfect discrimination), using the Frobenius norm:

$$\min_{FAs, T_Rs} = ||\mathbb{I} - D^+D||_F^2 \tag{72}$$

In the optimization procedure, the dictionary was limited to 142 combinations of T_1 (range = $50 - 3000$ ms) and T_2 (range = $25 - 2000$ ms) supposing ideal conditions for both B_0 and B_1.
The dictionaries, both the random and the optimized one, for the matching simulated the fingerprints for $\sim 11 \times 10^6$ combinations of different values of T_1 (range = $50 - 3000$ ms), T_2 (range = $10 - 2000$ ms), B_0 (range = $-100 - 100$ Hz), and B_1 (range = $0.9 - 1.4$). In Fig. 63 are reported the random and optimized FA and T_R values, while in Fig. 64 are shown the relative acquisitions. The corresponding dictionaries and their self-correlation matrices are illustrated in Fig. 65. As can be seen from the self-correlation matrix of the dictionary generated from the set of the randomly generated FA and T_R, the yellow area near the diagonal of the matrix is quite large (black points are those equal to 1). This could represent a problem for undersampled or noisy acquisitions. After the optimization the yellow area is

reduced by a lot: notice that no particular pattern is visible in the choice of *FA* and T_R with respect to random ones.

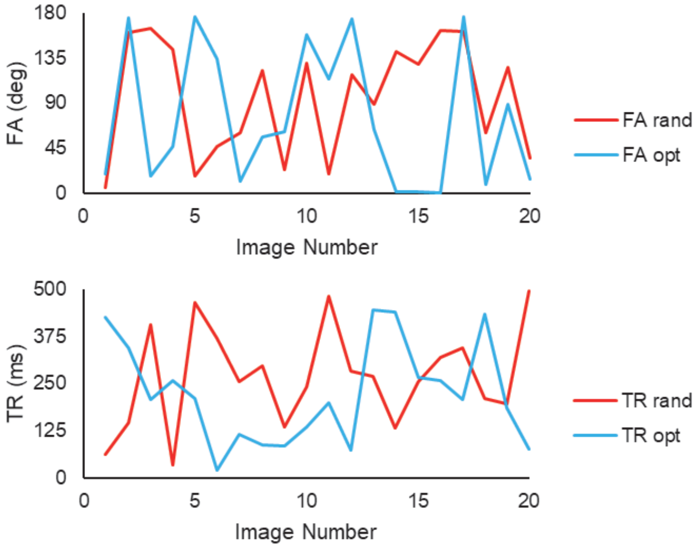

Figure 63: Comparison between *FA* and T_R values chosen randomly and obtained from the optimization procedure.

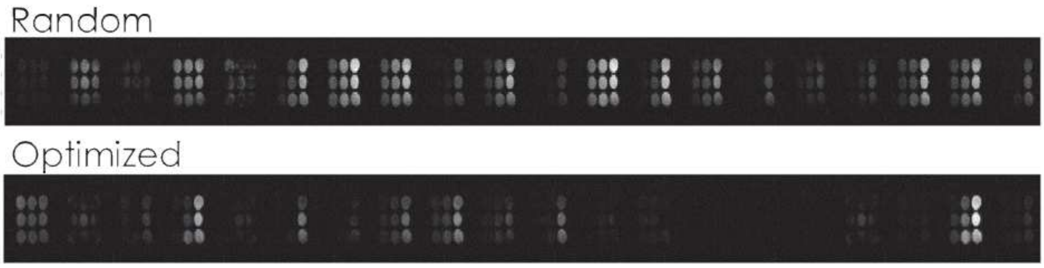

Figure 64: Random (top) and optimized (bottom) acquisitions of 20 images with the MRF-bSSFP sequence of Fig. 62 and the 20 couples of acquisition parameters of Fig. 63.

The parametric maps of M_0, T_1, T_2, B_0, B_1 were obtained through a custom Matlab algorithm (Mathworks, USA) performing a pixel-wise vector-based inner product comparison between the acquired and the simulated fingerprints composing the full dictionary.

As can be seen in Fig. 67, we obtained good matches for both acquisitions, with values of dot-products very close to 1 and with reasonable B_0 and B_1 maps (similar in both cases) but the main attention was focused on the different performances in the relaxation time estimation. From the Solomon-Bloembergen-Morgan theory, which describes the relaxation mechanism in paramagnetic aqueous dilute solutions, we expected linear dependence of the relaxation rates as a function of the $MnCl_2$ concentration in the aqueous

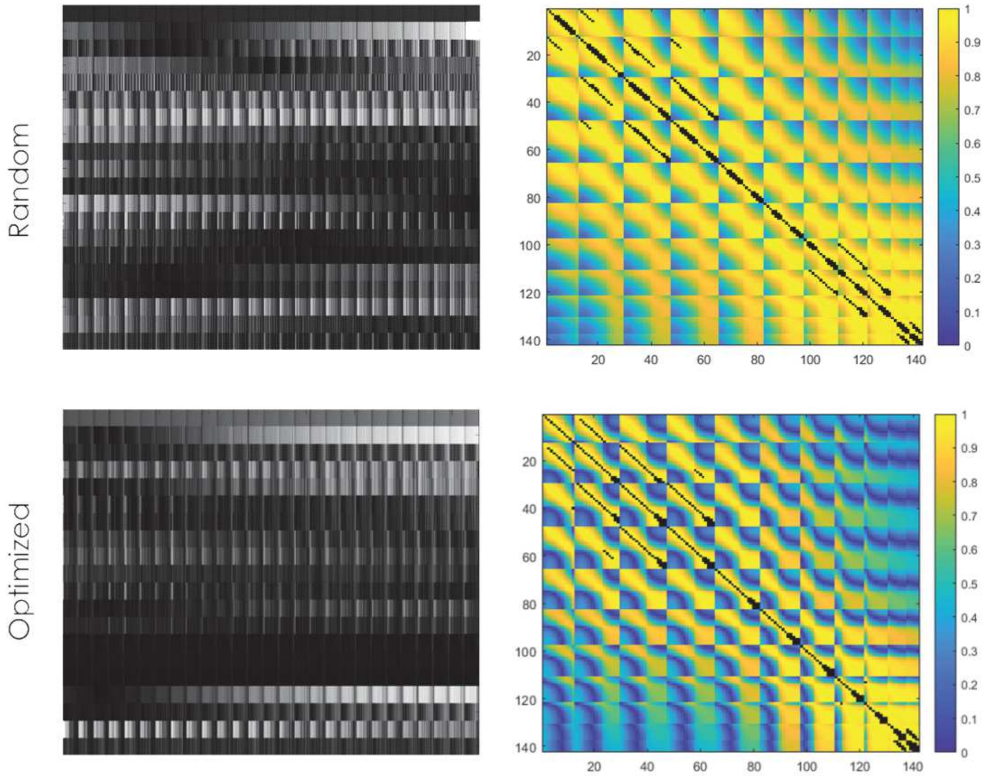

Figure 65: Pictorial representation of the random (top) and optimized (bottom) dictionaries (left) and self-correlation matrices (right). The points highlighted in black in the self-correlation matrices are those equal to 1.

solutions. A better agreement with the reference values was reached for T_1s obtained from the optimized set of acquisition parameters ($\mathrm{RMSE}_{\mathrm{rand}} = 0.21$, $\mathrm{RMSE}_{\mathrm{opt}} = 0.07$). T_2 values were found to be underestimated. Yet, we can see the effect of the optimization procedure because the theoretically expected linear dependence from the concentration of the transverse relaxation rate is restored ($R^2_{opt} = 0.998$; $R^2_{rand} = 0.94$).

Introducing slice selection gradients or 3D imaging gradients and considering also B_0 and B_1 in the optimization process could address the discrepancies found for T_2s.
Nevertheless, dictionary optimization provides a better estimation of the parametric maps. The latter could turn out to be promising for multiparametric MRI at low field, and be similarly explored at higher field regimes.

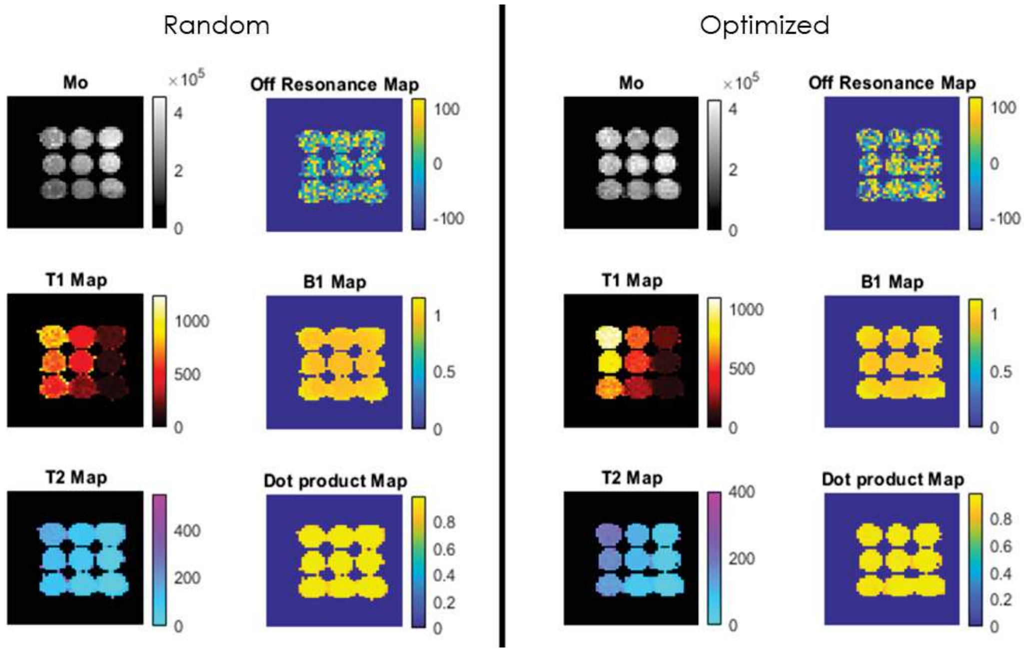

Figure 66: Matching results for the parametric maps of interest (M_0, T_1, T_2, B_0 and B_1) using the random (left) and the optimized (right) set of acquisition parameters FA and T_R. The dot product matrix between acquired data and the dictionary is also shown (threshold $= 0.8$).

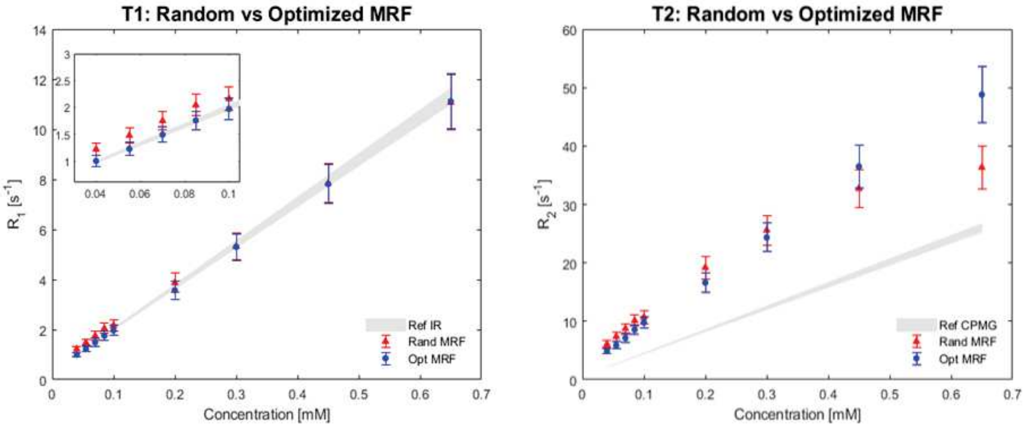

Figure 67: MRF results. The gray areas in the graph represents the reference values obtained with NMR spectroscopic IR and CPMG pulse sequences.

BIBLIOGRAPHY

[1] F. Bloch. “Nuclear induction”. In: *Physical Review* 70.7-8 (1946), p. 460 (cit. on pp. 1, 5, 36).

[2] I. I. Rabi, J. R. Zacharias, S. Millman, and P. Kusch. “A new method of measuring nuclear magnetic moment”. In: *Physical Review* 53.4 (1938), p. 318 (cit. on pp. 1, 5).

[3] P. Mansfield and P. K. Grannell. “NMR ’diffraction’ in solids?” In: *Journal of Physics C: Solid State Physics* 6.22 (1973), p. L422 (cit. on pp. 1, 15).

[4] R. W. Brown, Y.-C. N. Cheng, E. M. Haacke, M. R. Thompson, and R. Venkatesan. *Magnetic Resonance Imaging: Physical principles and sequence design*. John Wiley & Sons, 2014 (cit. on pp. 1, 5, 12–14, 18, 19, 21, 36, 72).

[5] H.-L. Margaret Cheng, N. Stikov, N. R. Ghugre, and G. A. Wright. “Practical medical applications of quantitative MR relaxometry”. In: *Journal of Magnetic Resonance Imaging* 36.4 (2012), pp. 805–824 (cit. on pp. 1, 22, 36, 60, 89).

[6] A. Carneiro, G. Vilela, D. De Araujo, and O Baffa. “MRI relaxometry: methods and applications”. In: *Brazilian Journal of Physics* 36.1A (2006), pp. 9–15 (cit. on pp. 2, 35).

[7] M. Salerno and C. M. Kramer. “Advances in parametric mapping with CMR imaging”. In: *JACC: Cardiovascular Imaging* 6.7 (2013), pp. 806–822 (cit. on pp. 2, 25, 27, 36, 60).

[8] F. S. Raman, N. Kawel-Boehm, N. Gai, M. Freed, J. Han, C.-Y. Liu, J. A. Lima, D. A. Bluemke, and S. Liu. “Modified look-locker inversion recovery T_1 mapping indices: assessment of accuracy and reproducibility between magnetic resonance scanners”. In: *Journal of Cardiovascular Magnetic Resonance* 15.1 (2013), pp. 1–10 (cit. on pp. 2, 36).

[9] S. Roujol, S. Weingärtner, M. Foppa, K. Chow, K. Kawaji, L. H. Ngo, P. Kellman, W. J. Manning, R. B. Thompson, and R. Nezafat. "Accuracy, precision, and reproducibility of four T_1 mapping sequences: a head-to-head comparison of MOLLI, ShMOLLI, SASHA, and SAPPHIRE". In: *Radiology* 272.3 (2014), pp. 683–689 (cit. on pp. 2, 25, 36, 46, 60).

[10] B. Baeßler, F. Schaarschmidt, C. Stehning, B. Schnackenburg, D. Maintz, and A. C. Bunck. "A systematic evaluation of three different cardiac T_2-mapping sequences at 1.5 and 3 T in healthy volunteers". In: *European Journal of Radiology* 84.11 (2015), pp. 2161–2170 (cit. on pp. 2, 28, 36, 46, 60).

[11] J. Shao, D. Liu, K. Sung, K.-L. Nguyen, and P. Hu. "Accuracy, precision, and reproducibility of myocardial T_1 mapping: A comparison of four T_1 estimation algorithms for modified look-locker inversion recovery (MOLLI)". In: *Magnetic Resonance in Medicine* 78.5 (2017), pp. 1746–1756 (cit. on pp. 2, 36).

[12] W. Bano, H. Feliciano, A. J. Coristine, M. Stuber, and R. B. Van Heeswijk. "On the accuracy and precision of cardiac magnetic resonance T_2 mapping: A high-resolution radial study using adiabatic T_2 preparation at 3 T". In: *Magnetic Resonance in Medicine* 77.1 (2017), pp. 159–169 (cit. on pp. 2, 36, 46).

[13] G. Captur, P. Gatehouse, P. Kellman, F. G. Heslinga, K. Keenan, R. Bruehl, M. Prothmann, M. J. Graves, A. Chiribiri, B. Ittermann, et al. "A T_1 and ECV phantom for global T_1 mapping quality assurance: The T_1 mapping and ECV standardisation in CMR (T1MES) program". In: *Journal of Cardiovascular Magnetic Resonance* 18.1 (2016), pp. 1–3 (cit. on pp. 2, 36, 46).

[14] K. E. Keenan, M. Ainslie, A. J. Barker, M. A. Boss, K. M. Cecil, C. Charles, T. L. Chenevert, L. Clarke, J. L. Evelhoch, P. Finn, et al. "Quantitative magnetic resonance imaging phantoms: a review and the need for a system phantom". In: *Magnetic Resonance in Medicine* 79.1 (2018), pp. 48–61 (cit. on pp. 2, 46).

[15] A. S. Merbach, L. Helm, and E. Toth. *The Chemistry of Contrast Agents in Medical Magnetic Resonance Imaging*. John Wiley & Sons, 2013 (cit. on pp. 2, 5, 63, 64, 68, 76).

[16] N. Bloembergen, E. M. Purcell, and R. V. Pound. "Relaxation effects in nuclear magnetic resonance absorption". In: *Physical Review* 73.7 (1948), p. 679 (cit. on pp. 2, 29, 39, 64).

[17] I. Solomon. "Relaxation processes in a system of two spins". In: *Physical Review* 99.2 (1955), p. 559 (cit. on pp. 2, 29, 39, 64).

[18] I Solomon and N Bloembergen. "Nuclear magnetic interactions in the HF molecule". In: *The Journal of Chemical Physics* 25.2 (1956), pp. 261–266 (cit. on pp. 2, 29, 64).

[19] N Bloembergen and L. Morgan. "Proton relaxation times in paramagnetic solutions. Effects of electron spin relaxation". In: *The Journal of Chemical Physics* 34.3 (1961), pp. 842–850 (cit. on pp. 2, 29, 39, 64).

[20] J. Wahsner, E. M. Gale, A. Rodríguez-Rodríguez, and P. Caravan. "Chemistry of MRI contrast agents: current challenges and new frontiers". In: *Chemical Reviews* 119.2 (2018), pp. 957–1057 (cit. on pp. 2, 64).

[21] S. Aime, M. Botta, L. Barbero, F. Uggeri, and F. Fedeli. "Water signal suppression by T_2-relaxation enhancement promoted by Dy (III) complexes". In: *Magnetic Resonance in Chemistry* 29.13 (1991), S85–S88 (cit. on pp. 2, 64, 78, 79).

[22] L. Vander Elst, A. Roch, P. Gillis, S. Laurent, F. Botteman, J. W. Bulte, and R. N. Muller. "Dy-DTPA derivatives as relaxation agents for very high field MRI: The beneficial effect of slow water exchange on the transverse relaxivities". In: *Magnetic Resonance in Medicine* 47.6 (2002), pp. 1121–1130 (cit. on pp. 2, 64, 68, 70, 78, 80).

[23] M. Harris, C. Henoumont, W. Peeters, S. Toyouchi, L. Vander Elst, and T. N. Parac-Vogt. "Amphiphilic complexes of Ho (III), Dy (III), Tb (III) and Eu (III) for optical and high field magnetic resonance imaging". In: *Dalton Transactions* 47.31 (2018), pp. 10646–10653 (cit. on pp. 3, 64).

[24] J. H. Monteiro. "Recent advances in luminescence imaging of biological systems using lanthanide (III) luminescent complexes". In: *Molecules* 25.9 (2020), p. 2089 (cit. on p. 3).

[25] R. Marin, G. Brunet, and M. Murugesu. "Shining New Light on Multifunctional Lanthanide Single-Molecule Magnets". In: *Angewandte Chemie International Edition* 60.4 (2021), pp. 1728–1746 (cit. on pp. 3, 66, 79).

[26] R. Van Eldik and I. Bertini. *Advances in Inorganic Chemistry: Relaxometry of water-metal ion interactions*. Elsevier, 2005 (cit. on p. 5).

[27] E. M. Purcell, H. C. Torrey, and R. V. Pound. "Resonance absorption by nuclear magnetic moments in a solid". In: *Physical Review* 69.1-2 (1946), p. 37 (cit. on p. 5).

[28] P. C. Lauterbur. "Image formation by induced local interactions: examples employing nuclear magnetic resonance". In: *Nature* 242.5394 (1973), pp. 190–191 (cit. on p. 15).

[29] M. A. Bernstein, K. F. King, and X. J. Zhou. *Handbook of MRI Pulse Sequences*. Elsevier, 2004 (cit. on pp. 16, 17, 19).

[30] J. Hennig, A Nauerth, and H. Friedburg. "RARE imaging: a fast imaging method for clinical MR". In: *Magnetic Resonance in Medicine* 3.6 (1986), pp. 823–833 (cit. on pp. 22, 36).

[31] Siemens. "Quantitative cardiac T_1 mapping using Sh-MOLLI". In: *Applications Guide* (2016) (cit. on p. 23).

[32] D. R. Messroghli, A. Radjenovic, S. Kozerke, D. M. Higgins, M. U. Sivananthan, and J. P. Ridgway. "Modified Look-Locker inversion recovery (MOLLI) for high-resolution T_1 mapping of the heart". In: *Magnetic Resonance in Medicine* 52.1 (2004), pp. 141–146 (cit. on pp. 23, 36).

[33] D. R. Messroghli, S. Plein, D. M. Higgins, K. Walters, T. R. Jones, J. P. Ridgway, and M. U. Sivananthan. "Human myocardium: single-breath-hold MR T_1 mapping with high spatial resolution - reproducibility study". In: *Radiology* 238.3 (2006), pp. 1004–1012 (cit. on pp. 23, 36, 44).

[34] A Oppelt, R Graumann, H Barfuss, H Fischer, W Hartl, W Schajor, et al. "FISP—a new fast MRI sequence". In: *Electromedica* 54.1 (1986), pp. 15–18 (cit. on p. 24).

[35] P. Kellman and M. S. Hansen. "T_1-mapping in the heart: accuracy and precision". In: *Journal of Cardiovascular Magnetic Resonance* 16.1 (2014), pp. 1–20 (cit. on p. 24).

[36] M. D. Robson, S. K. Piechnik, E. M. Tunnicliffe, and S. Neubauer. "T_1 measurements in the human myocardium: the effects of magnetization transfer on the SASHA and MOLLI sequences". In: *Magnetic Resonance in Medicine* 70.3 (2013), pp. 664–670 (cit. on p. 25).

[37] S. Giri, Y.-C. Chung, A. Merchant, G. Mihai, S. Rajagopalan, S. V. Raman, and O. P. Simonetti. "T_2 quantification for improved detection of myocardial edema". In: *Journal of Cardiovascular Magnetic Resonance* 11.1 (2009), pp. 1–13 (cit. on pp. 26, 27).

[38] T.-Y. Huang, Y.-J. Liu, A. Stemmer, and B. P. Poncelet. "T_2 measurement of the human myocardium using a T_2-prepared transient-state TrueFISP sequence". In: *Magnetic Resonance in Medicine* 57.5 (2007), pp. 960–966 (cit. on pp. 26, 28, 36, 89).

[39] J. H. Brittain, B. S. Hu, G. A. Wright, C. H. Meyer, A. Macovski, and D. G. Nishimura. "Coronary angiography with magnetization-prepared T_2 contrast". In: *Magnetic Resonance in Medicine* 33.5 (1995), pp. 689–696 (cit. on p. 26).

[40] M. Akçakaya, T. A. Basha, S. Weingärtner, S. Roujol, S. Berg, and R. Nezafat. “Improved quantitative myocardial T_2 mapping: Impact of the fitting model”. In: *Magnetic Resonance in Medicine* 74.1 (2015), pp. 93–105 (cit. on pp. 28, 36).

[41] I. Noebauer-Huhmann, P. Szomolanyi, C. Kronnerwetter, G. Widhalm, M. Weber, S. Nemec, V. Juras, M. Ladd, D. Prayer, and S. Trattnig. “Brain tumours at 7 T MRI compared to 3 T —contrast effect after half and full standard contrast agent dose: initial results”. In: *European Radiology* 25 (2014), pp. 106–112 (cit. on p. 29).

[42] A. Avasthi, C. Caro, E. Pozo-Torres, M. P. Leal, and M. L. García-Martín. “Magnetic nanoparticles as MRI contrast agents”. In: *Surface-modified Nanobiomaterials for Electrochemical and Biomedicine Applications* (2020), pp. 49–91 (cit. on p. 29).

[43] N Bloembergen. “Proton relaxation times in paramagnetic solutions”. In: *The Journal of Chemical Physics* 27.2 (1957), pp. 572–573 (cit. on pp. 29, 64).

[44] M. Guéron. “Nuclear relaxation in macromolecules by paramagnetic ions: a novel mechanism”. In: *Journal of Magnetic Resonance (1969)* 19.1 (1975), pp. 58–66 (cit. on pp. 30, 65, 72).

[45] D. Cicolari, D. Lizio, P. Pedrotti, M. T. Moioli, A. Lascialfari, M. Mariani, and A. Torresin. “A method for T_1 and T_2 relaxation times validation and harmonization as a support to MRI mapping”. In: *Journal of Magnetic Resonance* 334 (2022), p. 107110 (cit. on p. 35).

[46] C. E. Cann, H. K. Genant, B. Ettinger, and G. S. Gordan. “Spinal mineral loss in oophorectomized women: determination by quantitative computed tomography”. In: *JAMA* 244.18 (1980), pp. 2056–2059 (cit. on pp. 35, 46).

[47] W. A. Kalender and C. Suess. “A new calibration phantom for quantitative computed tomography”. In: *Medical Physics* 14.5 (1987), pp. 863–866 (cit. on pp. 35, 46).

[48] P. A. Bottomley, T. H. Foster, R. E. Argersinger, and L. M. Pfeifer. “A review of normal tissue hydrogen NMR relaxation times and relaxation mechanisms from $1-100$ MHz: dependence on tissue type, NMR frequency, temperature, species, excision, and age”. In: *Medical Physics* 11.4 (1984), pp. 425–448 (cit. on p. 35).

[49] P. A. Bottomley, C. Hardy, R. Argersinger, and G Allen-Moore. “A review of ^{1}H nuclear magnetic resonance relaxation in pathology: are T_1 and T_2 diagnostic?” In: *Medical Physics* 14.1 (1987), pp. 1–37 (cit. on p. 35).

[50] K. P. Whittall and A. L. MacKay. “Quantitative interpretation of NMR relaxation data”. In: *Journal of Magnetic Resonance (1969)* 84.1 (1989), pp. 134–152 (cit. on p. 36).

[51] B. Baeßler, F. Schaarschmidt, C. Stehning, B. Schnackenburg, A. Giolda, D. Maintz, and A. C. Bunck. “Reproducibility of three different cardiac T_2-mapping sequences at 1.5 T”. In: *Journal of Magnetic Resonance Imaging* 44.5 (2016), pp. 1168–1178 (cit. on pp. 36, 60).

[52] M. P. Graham-Brown, E. Rutherford, E Levelt, D. S. March, D. R. Churchward, D. J. Stensel, C. McComb, K. Mangion, S. Cockburn, C. Berry, et al. “Native T_1 mapping: inter-study, inter-observer and inter-center reproducibility in hemodialysis patients”. In: *Journal of Cardiovascular Magnetic Resonance* 19.1 (2017), pp. 1–10 (cit. on p. 36).

[53] O. Bane, S. J. Hectors, M. Wagner, L. L. Arlinghaus, M. P. Aryal, Y. Cao, T. L. Chenevert, F. Fennessy, W. Huang, N. M. Hylton, et al. “Accuracy, repeatability, and interplatform reproducibility of T_1 quantification methods used for DCE-MRI: Results from a multicenter phantom study”. In: *Magnetic Resonance in Medicine* 79.5 (2018), pp. 2564–2575 (cit. on p. 36).

[54] S. C. Deoni, T. M. Peters, and B. K. Rutt. “High-resolution T_1 and T_2 mapping of the brain in a clinically acceptable time with DESPOT1 and DESPOT2”. In: *Magnetic Resonance in Medicine* 53.1 (2005), pp. 237–241 (cit. on p. 36).

[55] P. Ehses, N. Seiberlich, D. Ma, F. A. Breuer, P. M. Jakob, M. A. Griswold, and V. Gulani. “IR TrueFISP with a golden-ratio-based radial readout: fast quantification of T_1, T_2, and proton density”. In: *Magnetic Resonance in Medicine* 69.1 (2013), pp. 71–81 (cit. on p. 36).

[56] D. Ma, V. Gulani, N. Seiberlich, K. Liu, J. L. Sunshine, J. L. Duerk, and M. A. Griswold. “Magnetic resonance fingerprinting”. In: *Nature* 495.7440 (2013), pp. 187–192 (cit. on pp. 36, 94).

[57] M. Akçakaya, S. Weingärtner, T. A. Basha, S. Roujol, S. Bellm, and R. Nezafat. “Joint myocardial T_1 and T_2 mapping using a combination of saturation recovery and T_2-preparation”. In: *Magnetic Resonance in Medicine* 76.3 (2016), pp. 888–896 (cit. on p. 36).

[58] B. Marty, B Coppa, and P. G. Carlier. “Fast, precise, and accurate myocardial T_1 mapping using a radial MOLLI sequence with FLASH readout”. In: *Magnetic Resonance in Medicine* 79.3 (2018), pp. 1387–1398 (cit. on p. 36).

[59] J. Shao, Z. Zhou, K.-L. Nguyen, J. P. Finn, and P. Hu. “Accurate, precise, simultaneous myocardial T_1 and T_2 mapping using a radial sequence with inversion recovery and T_2 preparation”. In: *NMR in Biomedicine* 32.11 (2019), e4165 (cit. on p. 36).

[60] M. Richards, W. Gregory, J. A. Webb, S. E. Jewell, and R. Reznek. "Reproducibility of spin lattice relaxation time (T_1) measurement using an 0.08 tesla MD 800 magnetic resonance imager". In: *The British Journal of Radiology* 60.711 (1987), pp. 241–244 (cit. on pp. 36, 39).

[61] G Johnson, I. Ormerod, D Barnes, P. Tofts, and D MacManus. "Accuracy and precision in the measurement of relaxation times from nuclear magnetic resonance images". In: *The British Journal of Radiology* 60.710 (1987), pp. 143–153 (cit. on p. 36).

[62] S. Keevil, G Dolke, P Armstrong, and M. Smith. "Calibration of a 0.08 Tesla magnetic resonance imager for in vivo T_1 and T_2 measurement". In: *The British Journal of Radiology* 65.773 (1992), pp. 438–442 (cit. on pp. 36, 46).

[63] A. P. Kurmis, C. Barber, J. P. Slavotinek, and N. L. Fazzalari. "A MnCl2-based MR signal intensity linear response phantom". In: *Radiologic Technology* 79.2 (2007), pp. 119–125 (cit. on p. 37).

[64] K. Thangavel and E. Ü. SARITAŞ. "Aqueous paramagnetic solutions for MRI phantoms at 3 T: A detailed study on relaxivities". In: *Turkish Journal of Electrical Engineering & Computer Sciences* 25.3 (2017), pp. 2108–2121 (cit. on p. 37).

[65] R. A. Bernheim, T. H. Brown, H. Gutowsky, and D. Woessner. "Temperature dependence of proton relaxation times in aqueous solutions of paramagnetic ions". In: *The Journal of Chemical Physics* 30.4 (1959), pp. 950–956 (cit. on p. 39).

[66] D. G. Altman and J. M. Bland. "Measurement in medicine: the analysis of method comparison studies". In: *Journal of the Royal Statistical Society: Series D (The Statistician)* 32.3 (1983), pp. 307–317 (cit. on p. 40).

[67] D. Giavarina. "Understanding bland altman analysis". In: *Biochemia Medica* 25.2 (2015), pp. 141–151 (cit. on p. 40).

[68] E. Heiberg, J. Sjögren, M. Ugander, M. Carlsson, H. Engblom, and H. Arheden. "Design and validation of Segment-freely available software for cardiovascular image analysis". In: *BMC Medical Imaging* 10.1 (2010), pp. 1–13 (cit. on p. 41).

[69] S. Bidhult, G. Kantasis, A. H. Aletras, H. Arheden, E. Heiberg, and E. Hedström. "Validation of T_1 and T_2 algorithms for quantitative MRI: performance by a vendor-independent software". In: *BMC Medical Imaging* 16.1 (2016), pp. 1–8 (cit. on p. 41).

[70] H. Xue, A. Greiser, S. Zuehlsdorff, M.-P. Jolly, J. Guehring, A. E. Arai, and P. Kellman. "Phase-sensitive inversion recovery for myocardial T_1 mapping with motion correction and parametric fitting". In: *Magnetic Resonance in Medicine* 69.5 (2013), pp. 1408–1420 (cit. on pp. 41, 60).

[71] K. Kraft, P. Fatouros, G. Clarke, and P. Kishore. "An MRI phantom material for quantitative relaxometry". In: *Magnetic Resonance in Medicine* 5.6 (1987), pp. 555–562 (cit. on p. 46).

[72] R. Lerski and J. De Certaines. "II. Performance assessment and quality control in MRI by Eurospin test objects and protocols". In: *Magnetic Resonance Imaging* 11.6 (1993), pp. 817–833 (cit. on p. 50).

[73] D. R. Messroghli, A. Greiser, M. Fröhlich, R. Dietz, and J. Schulz-Menger. "Optimization and validation of a fully-integrated pulse sequence for modified look-locker inversion-recovery (MOLLI) T_1 mapping of the heart". In: *Journal of Magnetic Resonance Imaging* 26.4 (2007), pp. 1081–1086 (cit. on p. 51).

[74] J. J. Lee, S. Liu, M. S. Nacif, M. Ugander, J. Han, N. Kawel, C. T. Sibley, P. Kellman, A. E. Arai, and D. A. Bluemke. "Myocardial T_1 and extracellular volume fraction mapping at 3 tesla". In: *Journal of Cardiovascular Magnetic Resonance* 13.1 (2011), pp. 1–10 (cit. on p. 51).

[75] P. Jezzard and R. S. Balaban. "Correction for geometric distortion in echo planar images from Bo field variations". In: *Magnetic Resonance in Medicine* 34.1 (1995), pp. 65–73 (cit. on p. 57).

[76] R. Stollberger and P. Wach. "Imaging of the active B1 field in vivo". In: *Magnetic Resonance in Medicine* 35.2 (1996), pp. 246–251 (cit. on p. 57).

[77] D. R. Messroghli, J. C. Moon, V. M. Ferreira, L. Grosse-Wortmann, T. He, P. Kellman, J. Mascherbauer, R. Nezafat, M. Salerno, E. B. Schelbert, et al. "Clinical recommendations for cardiovascular magnetic resonance mapping of T_1, T_2, T_2^* and extracellular volume: a consensus statement by the Society for Cardiovascular Magnetic Resonance (SCMR) endorsed by the European Association for Cardiovascular Imaging (EACVI)". In: *Journal of Cardiovascular Magnetic Resonance* 19.1 (2017), pp. 1–24 (cit. on p. 60).

[78] J. Z. Bojorquez, S. Bricq, C. Acquitter, F. Brunotte, P. M. Walker, and A. Lalande. "What are normal relaxation times of tissues at 3 T?" In: *Magnetic Resonance Imaging* 35 (2017), pp. 69–80 (cit. on p. 60).

[79] F. E. Mozes, E. M. Tunnicliffe, M. Pavlides, and M. D. Robson. "Influence of fat on liver T_1 measurements using modified Look–Locker inversion recovery (MOLLI) methods at 3 T". In: *Journal of Magnetic Resonance Imaging* 44.1 (2016), pp. 105–111 (cit. on p. 60).

[80] M. Meyerspeer, A. W. Magill, A. Kuehne, R. Gruetter, E. Moser, and A. I. Schmid. “Simultaneous and interleaved acquisition of NMR signals from different nuclei with a clinical MRI scanner”. In: *Magnetic Resonance in Medicine* 76.5 (2016), pp. 1636–1641 (cit. on p. 60).

[81] M. Wolf, A. de Boer, K. Sharma, P. Boor, T. Leiner, G. Sunder Plassmann, E. Moser, A. Caroli, and N. P. Jerome. “Magnetic resonance imaging T_1-and T_2-mapping to assess renal structure and function: a systematic review and statement paper”. In: *Nephrology Dialysis Transplantation* 33.suppl_2 (2018), pp. ii41–ii50 (cit. on p. 60).

[82] K. Nikiforaki, G. C. Manikis, E. Kontopodis, E. Lagoudaki, E. de Bree, K. Marias, A. H. Karantanas, and T. G. Maris. “T_2, T_2^* and spin coupling ratio as biomarkers for the study of lipomatous tumors”. In: *Physica Medica* 60 (2019), pp. 76–82 (cit. on p. 60).

[83] P. Kellman, D. A. Herzka, and M. S. Hansen. “Adiabatic inversion pulses for myocardial T_1 mapping”. In: *Magnetic Resonance in Medicine* 71.4 (2014), pp. 1428–1434 (cit. on p. 60).

[84] D. Cicolari, F. Santanni, L. Grassi, F. Brero, M. Filibian, T. Recca, P. Arosio, M. Perfetti, M. Mariani, R. Sessoli, et al. “Longitudinal and transverse NMR relaxivities of Ln (III)-DOTA complexes: a comprehensive investigation”. In: *The Journal of Chemical Physics* 155 (2021), p. 214201 (cit. on p. 63).

[85] P. H. Fries and E. Belorizky. “Electronic relaxation of paramagnetic metal ions and NMR relaxivity in solution: critical analysis of various approaches and application to a Gd (III)-based contrast agent”. In: *The Journal of Chemical Physics* 123.12 (2005), p. 124510 (cit. on p. 64).

[86] K. Ivanov, A. Yurkovskaya, and H.-M. Vieth. “High resolution NMR study of T_1 magnetic relaxation dispersion. I. Theoretical considerations of relaxation of scalar coupled spins at arbitrary magnetic field”. In: *The Journal of Chemical Physics* 129.23 (2008), p. 234513 (cit. on p. 64).

[87] D Kruk, J. Kowalewski, D. Tipikin, J. Freed, M Mościcki, A Mielczarek, and M Port. “Joint analysis of ESR lineshapes and 1H NMRD profiles of DOTA-Gd derivatives by means of the slow motion theory”. In: *The Journal of Chemical Physics* 134.2 (2011), p. 024508 (cit. on p. 64).

[88] J. Kowalewski, D. Kruk, and G. Parigi. “NMR relaxation in solution of paramagnetic complexes: recent theoretical progress for $S \geq 1$”. In: *Advances in Inorganic Chemistry* 57 (2005) (cit. on p. 64).

[89] J. H. Duyn. “The future of ultra-high field MRI and fMRI for study of the human brain”. In: *Neuroimage* 62.2 (2012), pp. 1241–1248 (cit. on p. 64).

[90] O. Kraff and H. H. Quick. “7 T: Physics, safety, and potential clinical applications”. In: *Journal of Magnetic Resonance Imaging* 46.6 (2017), pp. 1573–1589 (cit. on p. 64).

[91] G. Barisano, F. Sepehrband, S. Ma, K. Jann, R. Cabeen, D. J. Wang, A. W. Toga, and M. Law. “Clinical 7 T MRI: Are we there yet? A review about magnetic resonance imaging at ultra-high field”. In: *The British Journal of Radiology* 92.1094 (2019), p. 20180492 (cit. on p. 64).

[92] T. Nakada. “Clinical application of high and ultra high-field MRI”. In: *Brain and Development* 29.6 (2007), pp. 325–335 (cit. on p. 64).

[93] L. Frullano and T. J. Meade. “Multimodal MRI contrast agents”. In: *JBIC Journal of Biological Inorganic Chemistry* 12.7 (2007), pp. 939–949 (cit. on p. 64).

[94] P. Fries, J. N. Morelli, F. Lux, O. Tillement, G. Schneider, and A. Buecker. “The issues and tentative solutions for contrast-enhanced magnetic resonance imaging at ultra-high field strength”. In: *Wiley Interdisciplinary Reviews: Nanomedicine and Nanobiotechnology* 6.6 (2014), pp. 559–573 (cit. on p. 64).

[95] J. Garcia, J. Neelavalli, E. M. Haacke, and M. J. Allen. “Eu II - containing cryptates as contrast agents for ultra-high field strength magnetic resonance imaging”. In: *Chemical Communications* 47.48 (2011), pp. 12858–12860 (cit. on p. 64).

[96] J. Garcia, A. N. Kuda-Wedagedara, and M. J. Allen. “Physical properties of Eu2+-containing cryptates as contrast agents for ultra-high field magnetic resonance imaging”. In: *European Journal of Inorganic Chemistry* 2012.12 (2012), p. 2135 (cit. on p. 64).

[97] E. Debroye, S. Laurent, L. Vander Elst, R. N. Muller, and T. N. Parac-Vogt. “Dysprosium complexes and their micelles as potential bimodal agents for magnetic resonance and optical imaging”. In: *Chemistry – A European Journal* 19.47 (2013), pp. 16019–16028 (cit. on p. 64).

[98] M. Harris, S. Carron, L. Vander Elst, S. Laurent, R. N. Muller, and T. N. Parac-Vogt. “Magnetofluorescent micellar complexes of terbium (III) as potential bimodal contrast agents for magnetic resonance and optical imaging”. In: *Chemical Communications* 51.14 (2015), pp. 2984–2986 (cit. on p. 64).

[99] M. Harris, S. Carron, L. Vander Elst, S. Laurent, and T. N. Parac-Vogt. “Magnetofluorescent nanoaggregates incorporating terbium(III) complexes as potential bimodal agents for magnetic resonance and optical imaging”. In: *European Journal of Inorganic Chemistry* 2015.27 (2015), pp. 4572–4578 (cit. on pp. 64, 80).

[100] M. Harris, L. Vander Elst, S. Laurent, and T. N. Parac-Vogt. “Magnetofluorescent micelles incorporating Dy III–DOTA as potential bimodal agents for optical and high field magnetic resonance imaging”. In: *Dalton Transactions* 45.11 (2016), pp. 4791–4801 (cit. on p. 64).

[101] I. Bertini, F. Capozzi, C. Luchinat, G. Nicastro, and Z. Xia. “Water proton relaxation for some lanthanide aqua ions in solution”. In: *The Journal of Physical Chemistry* 97.24 (1993), pp. 6351–6354 (cit. on pp. 65, 70, 78, 80).

[102] P. H. Fries and E. Belorizky. “Quantitative interpretation of the very fast electronic relaxation of most Ln3+ ions in dissolved complexes”. In: *The Journal of Chemical Physics* 136.7 (2012), p. 074513 (cit. on p. 65).

[103] K. R. Lata, N Sahoo, and T. Das. “Nature of second hydration shell in Mn+ 2–aquoion system: Influence on proton relaxivity in nuclear magnetic resonance”. In: *The Journal of Chemical Physics* 94.5 (1991), pp. 3715–3721 (cit. on p. 65).

[104] R. Sharp. “The mechanism of paramagnetic NMR relaxation produced by Mn (II): Role of orthorhombic and fourth-order zero field splitting terms”. In: *The Journal of Chemical Physics* 129.14 (2008), p. 144307 (cit. on p. 65).

[105] M. Botta, F. Carniato, D. Esteban-Gómez, C. Platas-Iglesias, and L. Tei. “Mn (II) compounds as an alternative to Gd-based MRI probes”. In: *Future Medicinal Chemistry* 11.12 (2019), pp. 1461–1483 (cit. on pp. 65, 77).

[106] M. Briganti, E. Lucaccini, L. Chelazzi, S. Ciattini, L. Sorace, R. Sessoli, F. Totti, and M. Perfetti. “Magnetic Anisotropy Trends along a Full 4f-Series: The fn+ 7 Effect”. In: *Journal of the American Chemical Society* (2021) (cit. on pp. 66, 67, 79).

[107] V. L. Ermolaev and E. B. Sveshnikova. “The application of luminescence - kinetic methods in the study of the formation of lanthanide ion complexes in solution”. In: *Russian Chemical Reviews* 63.11 (1994), p. 905 (cit. on p. 67).

[108] K. J. Allen, E. C. Nicholls-Allison, K. R. Johnson, R. S. Nirwan, D. J. Berg, D. Wester, and B. Twamley. "Lanthanide Complexes of the Klaui Metalloligand, $CpCo(P{=}O(OR)_2)_3$: An Examination of Ligand Exchange Kinetics between Isotopomers by Electrospray Mass Spectrometry". In: *Inorganic Chemistry* 51.22 (2012), pp. 12436–12443 (cit. on p. 67).

[109] L. Tei, Z. Baranyai, L. Gaino, A. Forgács, A. Vágner, and M. Botta. "Thermodynamic stability, kinetic inertness and relaxometric properties of monoamide derivatives of lanthanide (III) DOTA complexes". In: *Dalton Transactions* 44.12 (2015), pp. 5467–5478 (cit. on p. 67).

[110] H. Terraschke, M. Rothe, and P. Lindenberg. "In situ monitoring metal-ligand exchange processes by optical spectroscopy and X-ray diffraction analysis: a review". In: *Reviews in Analytical Chemistry* 37.1 (2018) (cit. on p. 67).

[111] J. Peters, J Huskens, and D. Raber. "Lanthanide induced shifts and relaxation rate enhancements". In: *Progress in Nuclear Magnetic Resonance Spectroscopy* 28.3-4 (1996), pp. 283–350 (cit. on p. 68).

[112] J. Kowalewski, C. Luchinat, T. Nilsson, and G. Parigi. "Nuclear spin relaxation in paramagnetic systems: electron spin relaxation effects under near-Redfield limit conditions and beyond". In: *The Journal of Physical Chemistry A* 106.32 (2002), pp. 7376–7382 (cit. on p. 69).

[113] P. Gillis, A. Roch, and R. A. Brooks. "Corrected equations for susceptibility - induced T_2 - shortening". In: *Journal of Magnetic Resonance* 137.2 (1999), pp. 402–407 (cit. on p. 72).

[114] M.-E. Boulon, G. Cucinotta, J. Luzon, C. Degl'Innocenti, M. Perfetti, K. Bernot, G. Calvez, A. Caneschi, and R. Sessoli. "Magnetic anisotropy and spin-parity effect along the series of lanthanide complexes with DOTA". In: *Angewandte Chemie International Edition* 52.1 (2013), pp. 350–354 (cit. on pp. 72, 79).

[115] F Benetollo, G Bombieri, S Aime, and M Botta. "A holmium complex of a macrocyclic ligand (DOTA) and its isostructural europium analogue". In: *Acta Crystallographica Section C: Crystal Structure Communications* 55.3 (1999), pp. 353–356 (cit. on p. 72).

[116] J. F. Desreux. "Nuclear magnetic resonance spectroscopy of lanthanide complexes with a tetraacetic tetraaza macrocycle. Unusual conformation properties". In: *Inorganic Chemistry* 19.5 (1980), pp. 1319–1324 (cit. on p. 72).

[117] E Anoardo, G Galli, and G Ferrante. "Fast-field-cycling NMR: Applications and instrumentation". In: *Applied Magnetic Resonance* 20.3 (2001), pp. 365–404 (cit. on p. 73).

[118] C. V. G. Ferrante, D. Canina, E. Bonardi, M. Polello, and P. Golzi. "Measurement of spin-spin relaxation time T_2 at very low magnetic field by means of the Fast Field Cycling NMR method." In: *48th ENC Conference* (2007) (cit. on p. 73).

[119] D. Esteban-Gómez, C. Cassino, M. Botta, and C. Platas-Iglesias. "^{17}O and ^{1}H relaxometric and DFT study of hyperfine coupling constants in $[Mn(H_2O)_6]^{2+}$". In: *RSC Advances* 4.14 (2014), pp. 7094–7103 (cit. on pp. 75–77).

[120] I. Bertini, C. Luchinat, and G. Parigi. "^{1}H NMRD profiles of paramagnetic complexes and metalloproteins". In: *Advances in Inorganic Chemistry* 57.15 (2005), pp. 105–172 (cit. on pp. 75, 77).

[121] I Bertini, F Briganti, Z. Xia, and C Luchinat. "Nuclear magnetic relaxation dispersion studies of hexaaquo Mn(II) ions in water-glycerol mixtures". In: *Journal of Magnetic Resonance, Series A* 101.2 (1993), pp. 198–201 (cit. on pp. 75, 77).

[122] R Hausser and F Noack. "Kernmagnetische relaxation und korrelation in zwei-spin-systemen". In: *Zeitschrift für Physik* 182.1 (1964), pp. 93–110 (cit. on pp. 75, 77).

[123] D. H. Powell, O. M. N. Dhubhghaill, D. Pubanz, L. Helm, Y. S. Lebedev, W. Schlaepfer, and A. E. Merbach. "Structural and dynamic parameters obtained from ^{17}O NMR, EPR, and NMRD studies of monomeric and dimeric Gd^{3+} Complexes of interest in Magnetic Resonance Imaging: an integrated and theoretically self-consistent approach1". In: *Journal of the American Chemical Society* 118.39 (1996), pp. 9333–9346 (cit. on pp. 75–78).

[124] K. Micskei, L. Helm, E. Brucher, and A. E. Merbach. "Oxygen-17 NMR study of water exchange on gadolinium polyaminopolyacetates $[Gd(DTPA)(H_2O)]^{2-}$ and $[Gd(DOTA)(H_2O)]^{-}$related to NMR imaging". In: *Inorganic Chemistry* 32.18 (1993), pp. 3844–3850 (cit. on pp. 76, 77).

[125] G. Gonzalez, D. H. Powell, V. Tissieres, and A. E. Merbach. "Water-exchange, electronic relaxation, and rotational dynamics of the MRI contrast agent $[Gd(DTPA\text{-}BMA)(H_2O)]$ in aqueous solution: a variable pressure, temperature, and magnetic field oxygen-17 NMR study". In: *The Journal of Physical Chemistry* 98.1 (1994), pp. 53–59 (cit. on p. 77).

[126] S. Aime, M. Botta, G. Ermondi, F. Fedeli, and F. Uggeri. "Synthesis and NMRD studies of gadolinium (3+) complexes of macrocyclic polyamino polycarboxylic ligands bearing. beta.-benzyloxy-. alpha.-propionic residues". In: *Inorganic Chemistry* 31.6 (1992), pp. 1100–1103 (cit. on pp. 77, 78).

[127] S. Aime, L. Barbero, M. Botta, and G. Ermondi. “Determination of metal–proton distances and electronic relaxation times in lanthanide complexes by nuclear magnetic resonance spectroscopy”. In: *Journal of the Chemical Society, Dalton Transactions* 2 (1992), pp. 225–228 (cit. on p. 78).

[128] G. Cucinotta, M. Perfetti, J. Luzon, M. Etienne, P.-E. Car, A. Caneschi, G. Calvez, K. Bernot, and R. Sessoli. “Magnetic anisotropy in a dysprosium/DOTA single-molecule magnet: beyond simple magneto-structural correlations”. In: *Angewandte Chemie International Edition* 51.7 (2012), pp. 1606–1610 (cit. on p. 79).

[129] E. A. Suturina, K. Mason, C. F. Geraldes, N. F. Chilton, D. Parker, and I. Kuprov. “Lanthanide-induced relaxation anisotropy”. In: *Physical Chemistry Chemical Physics* 20.26 (2018), pp. 17676–17686 (cit. on p. 79).

[130] L. Smentek, B Andes Hess Jr, J. P. Cross, H Charles Manning, and D. J. Bornhop. “Density-functional theory structures of 1,4,7,10 - tetraazacyclododecane - 1,4,7,10 - tetraacetic acid complexes for ions across the lanthanide series”. In: *The Journal of Chemical Physics* 123.24 (2005), p. 244302 (cit. on p. 79).

[131] S. Aime, A. Barge, M. Botta, A. S. De Sousa, and D. Parker. “Direct NMR spectroscopic observation of a lanthanide-coordinated water molecule whose exchange rate is dependent on the conformation of the complexes”. In: *Angewandte Chemie International Edition* 37.19 (1998), pp. 2673–2675 (cit. on p. 79).

[132] S. Aime, M. Botta, M. Fasano, M. P. M. Marques, C. F. Geraldes, D. Pubanz, and A. E. Merbach. “Conformational and coordination equilibria on DOTA complexes of lanthanide metal ions in aqueous solution studied by 1H-NMR spectroscopy”. In: *Inorganic chemistry* 36.10 (1997), pp. 2059–2068 (cit. on p. 79).

[133] J. W. Bulte, C. Wu, M. W. Brechbiel, R. A. Brooks, J. Vymazal, M. Holla, and J. A. Frank. “Dysprosium-DOTA-PAMAM dendrimers as macromolecular T_2 contrast agents: preparation and relaxometry”. In: *Investigative Radiology* 33.11 (1998), pp. 841–845 (cit. on p. 80).

[134] K. E. Kellar, S. L. Fossheim, and S. H. Koenig. “Magnetic field dependence of solvent proton relaxation by solute dysprosium (III) complexes”. In: *Investigative Radiology* 33.11 (1998), pp. 835–840 (cit. on p. 80).

[135] M. Sarracanie and N. Salameh. “Low-field MRI: how low can we go? A fresh view on an old debate”. In: *Frontiers in Physics* 8 (2020), p. 172 (cit. on p. 89).

[136] L. M. Broche, P. J. Ross, G. R. Davies, M.-J. MacLeod, and D. J. Lurie. “A whole-body Fast Field-Cycling scanner for clinical molecular imaging studies”. In: *Scientific Reports* 9.1 (2019), pp. 1–11 (cit. on p. 89).

[137] O. Cohen and M. S. Rosen. “Algorithm comparison for schedule optimization in MR fingerprinting”. In: *Magnetic Resonance Imaging* 41 (2017), pp. 15–21 (cit. on p. 94).

LIST OF PUBLICATIONS

SCIENTIFIC PAPERS

Published

1. **D. Cicolari**, D. Lizio, P. Pedrotti, M. T. Moioli, A. Lascialfari, M. Mariani, A. Torresin. *A method for* T_1 *and* T_2 *relaxation times validation and harmonization as a support to MRI mapping*. Journal of Magnetic Resonance 2022, 344:107110. https://doi.org/10.1016/j.jmr.2021.107110
2. **D. Cicolari**, F. Santanni, L. Grassi, F. Brero, M. Filibian, T. Recca, P. Arosio, M. Perfetti, M. Mariani, R. Sessoli, A. Lascialfari. *Longitudinal and transverse NMR relaxivities of Ln(III)-DOTA complexes: a comprehensive investigation*. Journal of Chemical Physics 2021, 155:214201. https://doi.org/10.1063/5.0072185
3. P. Arosio, **D. Cicolari**, A. Manfredi, F. Orsini, A. Lascialfari, E. Ranucci, P. Ferrutti, D. Maggioni. *Nanosized* T_1 *MRI contrast agent based on a biocompatible and biodegradable polyamidoamine as multidentate Gd ligand*. Molecules 2022, 27:174. https://doi.org/10.3390/molecules27010174

Submitted

1. M. Fiorito, M. Yushchenko, **D. Cicolari**, N. Salameh, M. Sarracanie *Fast, interleaved, Look-Locker-based* T_1 *mapping sequence with a variable averaging approach: towards temperature mapping at low magnetic field* Submitted to NMR in Biomedicine.

In Progress

1. F. Brero, **D. Cicolari**, M. Albino, M. Porru, C. Sangregorio, F. Orsini, M. Mariani, P. Arosio, A. Lascialfari. *Magnetite core-shell nanoparticles and 1H-NMR relaxation properties: evaluation of the coating effect*

ABSTRACTS

PUBLISHED

1. **D. Cicolari**, D. Lizio, P. Pedrotti, M. T. Moioli, A. Lascialfari, M. Mariani, A. Torresin. *Characterization of an MRI phantom for relaxation times maps harmonization and optimization*. Physica Medica 92S1: S253-S254 (2021) - ECPM 2021. https://doi.org/10.1016/S1120-1797(22)00549-X
2. **D. Cicolari**, M. Yushchenko, M. Fiorito, R. Ayde, M. Mariani, N. Salameh, M. Sarracanie. *Effect of dictionary optimization on relaxation time maps in low field MR Fingerprinting applications*. Physica Medica 92S1: S13-S14 (2021) - ECMP 2021. https://doi.org/10.1016/S1120-1797(22)00034-5
3. **D. Cicolari**, F. Santanni, L. Grassi, F. Brero, M. Filibian, T. Recca, P. Arosio, M. Perfetti, M. Mariani, R. Sessoli, A. Lascialfari. *NMR characterization of lanthanide-based MRI contrast agents*. Atti 107° Congresso Nazionale SIF (2021). ISBN: 978-88-7438-127-2
4. P. Arosio, F. Brero, M. Albino, F. Orsini, M. Mariani, **D. Cicolari**, C. Innocenti, A. Lascialfari, C. Sangregorio. *The role of coating in magnetite core-shell nanoparticles studied with ^1H NMR relaxometry*. Atti 107° Congresso Nazionale SIF (2021). ISBN: 978-88-7438-127-2
5. M. Mariani, A. Lascialfari, F. Brero, **D. Cicolari**, M. Filibian, L. Rinaldi, L. Sorace, M. Fittipaldi, G. Latino, A. Rettori, F. Cinti, R.A. Rusnati, P. Arosio, F. Orsini, E. Giroletti, D. Redigolo, P. Santini, A. Moreira Nogueira, G. Poneti. *Magnetic properties and spin dynamics in lanthanide-semiquinone complexes: a NMR investigation*. Atti 107° Congresso Nazionale SIF (2021). ISBN: 978-88-7438-127-2
6. **D. Cicolari**, D. Lizio, P. Pedrotti, M. T. Moioli, A. Lascialfari, M. Mariani, A. Torresin. *3364. A phantom-based method for MRI relaxation time mapping data validation and harmonization*. Proc. Intl. Soc. Mag. Reson. Med. 29 (2021) - ISMRM 2021. ISSN#1545-4428
7. M. Fiorito, M. Yushchenko, **D. Cicolari**, M. Sarracanie, N. Salameh. *3315. In vivo T_1 quantification at 0.1 T using a fast, interleaved Look-Locker based T_1 mapping sequence*. Proc. Intl. Soc. Mag. Reson. Med. 29 (2021) - ISMRM 2021. ISSN#1545-4428
8. **D. Cicolari**, D. Lizio, P. Pedrotti, M. T. Moioli, A. Lascialfari, M. Mariani, A. Torresin. *MRI phantom calibration for relaxation times maps harmonization and optimization*. Atti 106° Congresso Nazionale SIF (2020). ISBN: 978-88-7438-123-4

9. **D. Cicolari**, M. Yushchenko, M. Fiorito, R. Ayde, M. Mariani, N. Salameh, M. Sarracanie. *L01.94. T_1- and T_2-prepared SSFP sequences for fast relaxometry at low field*. ESMRMB Congress 33 (Suppl 1): S69-S233 (2020). https://doi.org/10.1007/s10334-020-00876-y
10. M. Fiorito, M. Yushchenko, **D. Cicolari**, M. Sarracanie, N. Salameh. *L01.96. Fast, interleaved Look-Locker based T_1^* mapping for low field MR thermometry*. ESMRMB Congress 33 (Suppl 1): S69-S233 (2020). https://doi.org/10.1007/s10334-020-00876-y
11. **D. Cicolari**, D. Lizio, P. Pedrotti, M. T. Moioli, A. Lascialfari, M. Mariani, A. Torresin. *3774. Phantom study on magnetic resonance imaging (MRI) T_1 and T_2 relaxation times measurements standardization*. Proc. Intl. Soc. Mag. Reson. Med. 28 (2020) - ISMRM 2020. ISSN#1545-4428

Submitted

1. **D. Cicolari**, D. Lizio, P. Pedrotti, M. T. Moioli, A. Lascialfari, M. Mariani, A. Torresin. *Feasibility of map recalibration using an in-scan reference system for two MRI mapping cardiac sequences*. Submitted for the Joint Annual Meeting ISMRM-ESMRMB to be held in May 2022.
2. R. F. Cabini, L. Barzaghi, **D. Cicolari**, A. Pichiecchio, S. Figini, P. Arosio, M. Filibian, A. Lascialfari, S. Carrazza. *Application of Deep Learning techniques to Magnetic Resonance Fingerprinting*. Submitted for the Joint Annual Meeting ISMRM-ESMRMB to be held in May 2022.
3. M. Fiorito, M. Yushchenko, **D. Cicolari**, M. Sarracanie, N. Salameh. *Fast T_1-based MR Thermometry at Low Magnetic Field*. Submitted for the Joint Annual Meeting ISMRM-ESMRMB to be held in May 2022.

Journal of Magnetic Resonance 334 (2022) 107110

Contents lists available at ScienceDirect

Journal of Magnetic Resonance

journal homepage: www.elsevier.com/locate/jmr

A method for T_1 and T_2 relaxation times validation and harmonization as a support to MRI mapping

Davide Cicolari [a,*], Domenico Lizio [b], Patrizia Pedrotti [c], Monica Teresa Moioli [b], Alessandro Lascialfari [a], Manuel Mariani [a], Alberto Torresin [b,d]

[a] University of Pavia, Department of Physics, and INFN-Pavia Unit, Via Bassi 6, 27100 Pavia, Italy
[b] ASST Grande Ospedale Metropolitano Niguarda, Department of Medical Physics, P.zza Ospedale Maggiore 3, 20162 Milan, Italy
[c] ASST Grande Ospedale Metropolitano Niguarda, Department of Cardiology, P.zza Ospedale Maggiore 3, 20162 Milan, Italy
[d] University of Milan, Department of Physics, Via Celoria 16, 20133 Milan, Italy

ARTICLE INFO

Article history:
Received 19 July 2021
Revised 9 November 2021
Accepted 17 November 2021
Available online 20 November 2021

Keywords:
Relaxation time maps
Data harmonization
Calibration
Accuracy
Precision

ABSTRACT

We present a proof-of-concept study focusing on a method for the intra- and inter-center validation and harmonization of data obtained from MRI T_1 and T_2 maps. The method is based on a set of $MnCl_2$ samples that provide in-scan ground-truth reference values regardless of the details of the MRI protocol. The relaxation times of $MnCl_2$ aqueous solutions were first measured by means of an NMR laboratory relaxometer, as a function of concentration and temperature. The obtained T_1 and T_2 values, once renormalized at the scanner temperature, were used as reference values for the MRI mapping measurements of the $MnCl_2$ relaxation times. By using different clinical MRI scanners and sequences, we found a good agreement for standard and turbo sequences (limits of agreement: 5% for IR, SE, IR-TSE; 10% for TSE), while an under-estimation and an over-estimation were found respectively for MOLLI and T_2-prep TrueFISP, as already reported in the literature. The linearity of the relaxation rates with the concentration predicted by the Solomon-Bloembergen-Morgan theory was observed for every dataset at all temperatures, except for T_2-prep TrueFISP maps results. Some preliminary results of an *in vivo* experiment are also presented.

1. Introduction

The re-scaling of a parametric map using in-scan reference calibrated samples, hence resulting in a recalibration of the map, has been a commonly used technique for Computed Tomography (CT) applications since the 60s [1,2]. In fact, the intensity values from CT images, which reflect the absorption coefficients of different materials/tissues, are reported in Hounsfield Units (HU), and are often re-scaled using reference standard values from calibrated samples scanned simultaneously with the patient. On the other hand, MRI often suffers from limited use of in-scan reference standards for improved accuracy of quantitative imaging data acquisitions which can provide physiologically relevant parametric maps. In recent years, thanks to the technological developments of MRI scanners, such sequences have become routine in todays clinical settings [3]. To further establish quantitative MRI for diagnostic purposes there is a strong need for advanced acquisition and analysis approaches that can guarantee accuracy and precision of diagnosis, but also enable robust reliability and reproducibility of across different scanners (both intra and interinstitutional) [4,5].

MRI parametric maps of the spin–lattice relaxation times (T_1) and of the spin–spin relaxation times (T_2) are extracted from MR images acquired using dedicated T_1- or T_2- "weighted" sequences with variable acquisition parameters in a sequential or interleaved manner, obtaining sets of the same slice images with different parameter values (*e.g.* different inversion times for the Inversion Recovery imaging sequence [6], or different echo-times for the Spin-Echo imaging sequence [6]). The resulting set of images with variable parameter-dependent intensities are then used to extract relaxation time parametric maps through a voxel-by-voxel least-square-fitting analysis using the phenomenological Bloch equations [6,7], which describe the relaxation behavior of the nuclear system, usually composed of hydrogen nuclei, decoupling the different relaxation time contrast mechanisms that contribute to the overall MR signal: for example, the signal for an image

---

[*] Corresponding author.

E-mail addresses: davide.cicolari01@universitadipavia.it (D. Cicolari), domenico.lizio@ospedaleniguarda.it (D. Lizio), patrizia.pedrotti@ospedaleniguarda.it (P. Pedrotti), monicateresa.moioli@ospedaleniguarda.it (M.T. Moioli), alessandro.lascialfari@unipv.it (A. Lascialfari), manuel.mariani@unipv.it (M. Mariani), alberto.torresin@unimi.it (A. Torresin).

https://doi.org/10.1016/j.jmr.2021.107110
1090-7807/

The Journal of Chemical Physics | ARTICLE | scitation.org/journal/jcp

Longitudinal and transverse NMR relaxivities of Ln(III)-DOTA complexes: A comprehensive investigation

Cite as: J. Chem. Phys. 155, 214201 (2021); doi: 10.1063/5.0072185
Submitted: 20 September 2021 • Accepted: 11 November 2021 •
Published Online: 1 December 2021

View Online Export Citation CrossMark

Davide Cicolari,[1,2,a)] Fabio Santanni,[3] Leonardo Grassi,[3] Francesca Brero,[1,2] Marta Filibian,[2,4] Teresa Recca,[4] Paolo Arosio,[5,6] Mauro Perfetti,[3] Manuel Mariani,[1,2] Roberta Sessoli,[3] and Alessandro Lascialfari[1,2]

AFFILIATIONS

[1] Department of Physics, University of Pavia, Via Bassi 6, Pavia (PV) 27100, Italy
[2] INFN, Istituto Nazionale di Fisica Nucleare–Pavia Unit, Via Bassi 6, Pavia (PV) 27100, Italy
[3] Department of Chemistry, University of Florence, Sesto Fiorentino (FI) 50019, Italy
[4] Centro Grandi Strumenti, University of Pavia, Via Bassi 21, Pavia (PV) 27100, Italy
[5] Department of Physics, University of Milan, Via Celoria 16, Milan (MI) 20133, Italy
[6] INFN, Istituto Nazionale di Fisica Nucleare–Milan Unit, Via Celoria 16, Milan (MI) 20133, Italy

[a)] Author to whom correspondence should be addressed: davide.cicolari01@universitadipavia.it. Telephone: +39 0382 987483

ABSTRACT

Longitudinal and transverse ^{1}H nuclear magnetic resonance relaxivities of Ln(III)-DOTA complexes (with Ln = Gd, Tb, Dy, Er; DOTA = 1,4,7,10-tetraazacyclododecane-N,N′,N″,N‴-tetraacetic acid) and Mn(II) aqueous solutions were measured in a wide range of frequencies, 10 kHz to 700 MHz. The experimental data were interpreted by means of models derived from the Solomon–Bloembergen–Morgan theory. The data analysis was performed assuming the orbital angular momentum $L = 0$ for Gd-DOTA and the aqua ion $[Mn(H_2O)_6]^{2+}$ and $L \neq 0$ for Dy-, Tb-, and Er-DOTA. A refined estimation of the zero-field-splitting barrier Δ and of the modulation correlation time τ_v was obtained for $[Mn(H_2O)_6]^{2+}$ by extending the fitting of nuclear magnetic relaxation dispersion profiles to the low-field regime. The Gd-DOTA fitting parameters resulted in good agreement with the literature, and the fit of transverse relaxivity data confirmed the negligibility of the scalar interaction in the nuclear relaxation mechanism. Larger transverse relaxivities of Dy-DOTA and Tb-DOTA (~10 mM^{-1} s^{-1}) with respect to Er-DOTA (~1 mM^{-1} s^{-1}) were observed at 16 T. Such higher values are suggested to be due to a shorter residence time τ_m that is possibly linked to the fluctuations of the hyperfine interaction and the different shape of the magnetic anisotropy. The possible employment of Dy-DOTA, Tb-DOTA, and Er-DOTA as negative magnetic resonance imaging contrast agents for high-field applications was envisaged by collecting spin-echo images at 7 T. Particularly in Dy- and Tb-derivatives, the transverse relaxivity at 16 T is of the order of the Gd-one at 1.5 T.

INTRODUCTION

The Magnetic Resonance Imaging (MRI) contrast agents have been extensively studied in the last 40 years, and their use in medicine is widespread, especially for the most common applications at 1.5 and 3 T,[1] The main property that allows these systems to enhance the MRI sensitivity is the ability of improving the image contrast, taking advantage of their capability to increase the nuclear relaxation rates. For their characterization, Nuclear Magnetic Resonance (NMR) is commonly employed for collecting nuclear relaxivity data, i.e., the relaxation rate increment (with respect to the pure solvent) normalized to 1 mM concentration of the contrast agent (CA), as a function of Larmor resonance frequency $\nu = (\gamma/2\pi)B_0$, where γ is the gyromagnetic ratio of the nuclear species, usually ^{1}H, and B_0 is the applied static magnetic field. The acquired data generate the so-called Nuclear Magnetic Relaxation Dispersion (NMRD) profiles, which can be analyzed according to models based on Solomon–Bloembergen–Morgan (SBM) theory[2–5] for

molecules

MDPI

Article

Nanosized T_1 MRI Contrast Agent Based on a Polyamidoamine as Multidentate Gd Ligand

Paolo Arosio [1,2,*], Davide Cicolari [3], Amedea Manfredi [4], Francesco Orsini [1,2], Alessandro Lascialfari [3], Elisabetta Ranucci [4], Paolo Ferruti [4] and Daniela Maggioni [2,4,*]

[1] Dipartimento di Fisica, INFN, Istituto Nazionale di Fisica Nucleare-Milano Unit, Università degli Studi di Milano, Via Celoria 16, 20133 Milano, Italy; francesco.orsini@unimi.it
[2] Consorzio Interuniversitario Nazionale per la Scienza e Tecnologia dei Materiali, Via Golgi 19, 20133 Milano, Italy
[3] Dipartimento di Fisica, INFN, Istituto Nazionale di Fisica Nucleare-Milano Unit, Università degli Studi di Pavia, Via Bassi 6, 27100 Pavia, Italy; davide.cicolari01@universitadipavia.it (D.C.); alessandro.lascialfari@unipv.it (A.L.)
[4] Dipartimento di Chimica, Università degli Studi di Milano, Via Golgi 19, 20133 Milano, Italy; amedea.manfredi@unimi.it (A.M.); elisabetta.ranucci@unimi.it (E.R.); paolo.ferruti@unimi.it (P.F.)
[*] Correspondence: paolo.arosio@unimi.it (P.A.); daniela.maggioni@unimi.it (D.M.)

Abstract: A linear polyamidoamine (PAA) named BAC-EDDS, containing metal chelating repeat units composed of two *tert*-amines and four carboxylic groups, has been prepared by the aza-Michael polyaddition of ethylendiaminodisuccinic (EDDS) with 2,2-bis(acrylamido)acetic acid (BAC). It was characterized by size exclusion chromatography (SEC), FTIR, UV–Vis and NMR spectroscopies. The pK_a values of the ionizable groups of the repeat unit were estimated by potentiometric titration, using a purposely synthesized molecular ligand (Agly-EDDS) mimicking the structure of the BAC-EDDS repeat unit. Dynamic light scattering (DLS) and ζ-potential analyses revealed the propensity of BAC-EDDS to form stable nanoaggregates with a diameter of approximately 150 nm at pH 5 and a net negative charge at physiological pH, in line with an isoelectric point <2. BAC-EDDS stably chelated Gd (III) ions with a molar ratio of 0.5:1 Gd (III)/repeat unit. The stability constant of the molecular model Gd-Agly-EDDS (log K = 17.43) was determined as well, by simulating the potentiometric titration through the use of Hyperquad software. In order to comprehend the efficiency of Gd-BAC-EDDS in contrasting magnetic resonance images, the nuclear longitudinal (r_1) and transverse (r_2) relaxivities as a function of the externally applied static magnetic field were investigated and compared to the ones of commercial contrast agents. Furthermore, a model derived from the Solomon–Bloembergen–Morgan theory for the field dependence of the NMR relaxivity curves was applied and allowed us to evaluate the rotational correlation time of the complex (τ = 0.66 ns). This relatively high value is due to the dimensions of Gd-BAC-EDDS, and the associated rotational motion causes a peak in the longitudinal relaxivity at ca. 75 MHz, which is close to the frequencies used in clinics. The good performances of Gd-BAC-EDDS as a contrast agent were also confirmed through in vitro magnetic resonance imaging experiments with a 0.2 T magnetic field.

Keywords: polyamidoamine; MRI; relaxivities; Gd-based contrast agent; nanosized contrast agent

check for updates

Citation: Arosio, P.; Cicolari, D.; Manfredi, A.; Orsini, F.; Lascialfari, A.; Ranucci, E.; Ferruti, P.; Maggioni, D. Nanosized T_1 MRI Contrast Agent Based on a Polyamidoamine as Multidentate Gd Ligand. *Molecules* **2022**, *27*, 174. https://doi.org/10.3390/molecules27010174

Academic Editor: Giovanni Palmisano

Received: 18 October 2021
Accepted: 23 December 2021
Published: 28 December 2021

1. Introduction

Magnetic resonance imaging (MRI) is an in-clinic diagnostic modality that has received tremendous development for many decades. It allows for obtaining images of an organism in a non-invasive way, without damaging ionizing radiation and with an excellent penetration depth, having the advantage of providing better spatial resolution than other clinical imaging modalities [1–9]. Unfortunately, in many cases, the natural tissue contrast is not enough to obtain images of good quality. For that reason, many different contrast agents have been developed since the 1970s. To date, the contrast agents used clinically are small molecules, mostly gadolinium chelates, which, however, have the drawback of a

ACKNOWLEDGMENTS

First of all, I want to express my gratitude to the University of Pavia for granting my PhD and the research activity, even included the scolarship I received for a four-months mobility period at the AMT Center in Basel (Switzerland).

I also want to thank Prof. Lucio Andreani and Prof. Daniela Rebuzzi for all the very hard work they have done for the PhD program in Physics here in Pavia.

Special thanks to Prof. Mauro Botta (Università del Piemonte Orientale) and Prof. Sophie Laurent (University of Mons) for promptly accepting to be referees of my thesis, giving me precious advices.

My sincere and full gratitude goes to my supervisor, Prof. Alessandro Lascialfari, for the opportunity he gave me, as well for his constant help and precious suggestions. He really provided me a model to aim both from a scientific and human point of view.

Likewise, to my advisor Dr. Manuel Mariani is addressed my thankfulness for his continuous contribution to my work and for his constant presence on which I could count on throughout all the PhD and even before, during the master thesis.

A special thank to the Niguarda group, in particular to Prof. Alberto Torresin, Dr. Domenico Lizio, and Dr. Patrizia Pedrotti, who supported my research since my master thesis and now have warmly welcome me to be part of their team.

I also owe my gratitude to the chemists of the University of Florence, Prof. Roberta Sessoli, Dr. Mauro Perfetti, and Dr. Fabio Santanni, for sharing with me their precious knowledge concerning the chemistry of the contrast agents.

I wish to express my gratitude to Prof. Mathieu Sarracanie and Prof. Najat Salameh, heads of the AMT Center, for their availability in hosting me in their institution. I have a wonderful memories of the period spent in Basel even if complicated by the Covid pandemic (since the very first day...). Many thanks also to Dr. Marco Fiorito, Dr. Maksym Yushchencko and Dr. Reina Ayde. As I always say, I left a part of my heart in Basel.

Many thanks to Dr. Paolo Arosio, Dr. Marta Filibian, and Dr. Linda Bianchini for their experimental and human support.

A special mention to Dr. Matteo Avolio and Dr. Francesca Brero for sharing with me their experience and for their precious help since the very beginning. I will always remember affectionately the days in our office and in the laboratory, as well as every other moment spent together.

I would like to thank also Dr. Lisa Rinaldi and my other PhD colleagues for sharing with me this marvelous adventure.

These three year of PhD in Pavia, even if affected by hard challenges (I begun my PhD experience with a severe injury at the Achille’s tendon, one of the worsts for a basketball player like me, not to mention the global pandemic started in 2020...), have been enriched by fantastic people and if you are reading these lines you are probably part of them. Thank you.

I will be always grateful to my family, their support goes beyond any words.

And to Beatrice, thank you for having chosen me and for simply everything.